Master Thesis

Conducted at the

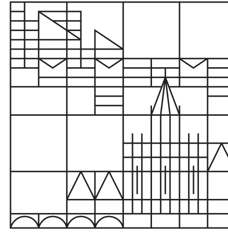

in the Photovoltaic Division of

Prof. Dr. Giso Hahn

between December 2015 and March 2017

Characterization of Structured Doping Areas Diffused from Doped CVD Layers on Crystalline Si Substrates

Author:
Yannick Dupuis

First Supervisor: Prof. Dr. Giso Hahn
Second Supervisor: Prof. Dr. Thomas Dekorsy

Mentors:
Josh Engelhardt & Daniel Sommer

Konstanz, June 6, 2017

Konstanzer Online-Publikations-System (KOPS)
URL: http://nbn-resolving.de/urn:nbn:de:bsz:352-0-410666

Contents

List of Abbreviations iii

1 Motivation 1

2 Physics of Solar Cells 3
2.1 Working Principle . . . 3
2.1.1 Semiconductor Material . . . 3
2.1.2 Photon Absorption . . . 3
2.1.3 Charge Carriers . . . 5
2.1.4 Doping, Profiles and Sources . . . 6
2.1.5 pn-Junction . . . 10
2.2 Recombination Loss and Passivation . . . 11
2.2.1 Loss Mechanisms . . . 11
2.2.2 Surface Passivation . . . 12
2.2.3 Recombination at the pn-Junction . . . 13
2.3 Metallization . . . 14
2.4 Solar Cell Structure . . . 15
2.4.1 Standard Solar Cell . . . 15
2.4.2 Back Contact Back Junction Solar Cells - Advantages and Challenges . . . 15
2.5 Characteristic Quantities . . . 17
2.5.1 J-V Curve . . . 17
2.5.2 Free Energy Loss Analysis . . . 19

3 Simulation 21
3.1 Quokka . . . 21
3.2 Comparison Quokka and Sentaurus . . . 22
3.3 Simulation of the pn-Junction . . . 30

4 Analysis and Results 35
4.1 Chemical Vapor Deposition (CVD) . . . 36
4.2 Local Removal of Dielectric Material . . . 36
4.2.1 Photolithography . . . 37
4.2.2 Laser-Ablation . . . 40
4.2.3 Creating pn-Junctions . . . 44
4.2.4 Contact Opening . . . 49
4.3 Metallization . . . 50
4.3.1 Contact Formation . . . 50
4.3.2 Metallization Mask . . . 52
4.3.3 Shunting . . . 52
4.4 Effective Lifetime and Surface Passivation . . . 57
4.4.1 Effective Lifetime Measurement . . . 57
4.4.2 Photoluminescence . . . 58
4.4.3 Sample Preparation . . . 59
4.4.4 Rear Side Passivation . . . 59

4.4.5 Bulk Lifetime 63
4.4.6 Front Side Passivation 64
4.5 Characterization Method 66
4.5.1 Illumination Mask 67
4.5.2 Alignment Method 67
4.5.3 J-V Curve Measurement 69
4.6 J-V Curve Measurement Results 69
4.6.1 Patterning of the pn-Junction 69
4.6.2 Surface Passivation 70
4.6.3 Contact Opening 72
4.6.4 Conclusion 72

5 Summary and Outlook **73**

6 Zusammenfassung und Ausblick [german] **75**

List of Abbreviations

Abbreviation	Meaning
A	Area
Ag	Silver
ALD	Atomic Layer Deposition
Al	Aluminum
APCVD	Atmospheric Pressure CVD
ARC	Anti-Reflective Coating
a-Si	Hydrogenated intrinsic amorphous silicon (i)a-Si:H
α	Absorption coefficient
B	Boron
BC-BJ	Back Contact Back Junction
BHF	Buffered HF solution
BRL	Boron Rich Layer
BSF	Back Surface Field
COSIMA	Local COntacts to a-SI-passivated solar cells by Means of Annealing
CO_2	Carbon dioxide
CVD	Chemical Vapor Deposition
C_a	Ambipolar Auger coefficient
c-Si	Crystalline silicon
$D_{\mathrm{n,p}}$	Diffusion constant
Δn	Excess carrier density
EDX	Energy-Dispersive X-ray spectroscopy
E	Energy
E_c	Energy at the bottom of the conduction band
E_F	Fermi energy
$E_{F,n/p}$	Quasi-Fermi energies
E_g	Band gap energy
$E_{g,Si}$	Band gap energy of silicon
E_t	Trap state energy level
E_v	Energy at the top of the valence band
E_γ	Photon energy
ε	Electric field at the pn-junction
FELA	Free Energy Loss Analysis
FF	Fill factor
FSF	Front Surface Field
$\phi_\gamma(x)$	Photon flux
ϕ_{g}	Photogeneration rate of free energy density

Abbreviation	Meaning
$\phi_{\mathrm{t,e/h}}$	Free energy density dissipation rate by transporting charge carriers
$\phi_{\mathrm{r,b/s}}$	Charge carrier recombination loss rate in the bulk/at the surface
G	Generation rate
$\mathrm{G}_\gamma(\lambda, x)$	Generation profile
HF	Hydrogen Fluoride
$\hbar$	Reduced Planck constant
η	Power conversion efficiency
IBC	Interdigitated Back Contact
J_{gen}	Generated current density
J_{mpp}	Current density at the MPP
$\vec{J}_{\mathrm{Q,e/h}}$	Charge current density of electrons/holes
J_{sc}	Short circuit current density
J_{shunt}	Shunt current density
J-V curve	Current density-voltage curve
J_0	Recombination parameter
KPFM	Kelvin Probe Force Microscopy
k	Wave vector
k_B	Boltzmann's constant
κ	Extinction coefficient
$L_{\mathrm{n,p}}$	Diffusion length
λ	Photon wavelength
MPP	Maximum Power Point
n	Ideality factor
NH_4F	Ammonium fluoride
$\mathrm{N_A}$	Acceptor doping concentration
$\mathrm{N_D}$	Donor doping concentration
N_{t}	Trap density
n^+	Highly n-doped
ν_{th}	Thermal velocity
p	Momentum
P	Phosphorus
PCD	Transient Photoconductance Decay
Pd	Palladium
PECVD	Plasma-Enhanced CVD
$POCl_3$	Phosphorus oxychloride
PSG	Phosphorus Silicate Glass
p^+-doped	Highly p-doped
ρ_c	Specific contact resistivity
R	Recombination rate

Abbreviation	Meaning
R_{c}	Contact resistance
R_{series}	Series resistance
R_{sheet}	Sheet resistance
R_{shunt}	Shunt resistance
SCR	Space Charge Region
SEM	Scanning Electron Microscope
Si	Silicon
SiH_4	Silane
SiN_x	Silicon nitride
SiO_x	Silicon oxide
SiO_x:B	Borosilicate glass
SRH	Shockley-Read-Hall
σ	Capture cross section for charge carriers
$\sigma_{\mathrm{e/h}}$	Electron/hole conductivity
Ti	Titanium
TLM	Transfer Length Method
τ	Resulting minority charge carrier lifetime
τ_{Auger}	Charge carrier lifetime for Auger recombination
τ_{eff}	Effective minority charge carrier lifetime
τ_{rad}	Charge carrier lifetime for radiative recombination
τ_{SRH}	Charge carrier lifetime for SRH recombination
V_{mpp}	Voltage at the MPP
V_{oc}	Open circuit voltage
V_{th}	Thermal voltage
$\tilde{V}$	Volume
q	Elementary charge
QSSPC	Quasi-Steady-State Photoconductance

1 Motivation

Our sun constantly emits electromagnetic radiation to Earth due to nuclear fusion reaction of hydrogen and helium in its core. Solar irradiance integration over the earth's illuminated surface, amounts in energy that is 10000 times larger than the world's primary energy consumption[1]. This illustrates that the solar energy reaching Earth is in theory abundant to cover the world's current energy consumption.
Humans harness the sun's energy in various ways. Sunlight can be used directly to grow plants or as a heat source, or as a mean of electricity production with solar panels, wind turbines, biomass and hydro-power plants. Fossil fuel on the contrary was formed millions of years ago and is essentially stored solar energy that can be used in limited amounts nowadays. In contrast to renewable energy originating from e.g. solar cells, burning fossil fuel intensifies global warming due to the greenhouse effect[2],[3]. As a consequence the use of fossil fuels is to be avoided and renewable energies are to be used to provide the Earth's population with energy.
A key renewable energy is photovoltaics, where solar radiation is directly converted into electricity using a solar cell. The conversion of light into electrical power was first discovered by Becquerel in 1839 while experimenting with a solid electrode in an electrolyte[4]. Only in the beginning of the 20th century, with the introduction of quantum theory, the effect could be explained by scientists. This discovery lead to the development of solar cells, with the first silicon solar cell being presented in 1954 by Chapin et al. with a power conversion efficiency of approximately 6%[5]. To this day Si is the dominant material in solar cell production (∼90%) because of high power conversion efficiencies, low production costs and its remarkable reliability[6].
Currently front and rear contacted crystalline silicon solar cells with a phosphorus-diffused emitter on the front side and an aluminum-diffused back surface field on the rear side constitute the most common solar cell architecture. The advantage of these standard solar cells is the simplicity and cost-efficiency in the production process, however, the conversion efficiency of such cells is practically limited to ∼19%[7]. Therefore, cutting-edge silicon solar cells that achieve a higher conversion efficiency with cost efficient production methods can considerably lower the production costs per generated electrical power output and are expected to increase their market share in the years to come.
The cutting-edge solar cell concept holding the world record efficiency of 26.3%[8] is a Back Contact-Back Junction (BC-BJ) solar cell, where all parts of the front contact grid are moved to the rear of the device. Rear contact solar cells have the advantage of no shading loss as well as of more freedom in metallization and front side design. Due to the exceptional results achieved with the BC-BJ solar cell concept by different research teams around the world[9]–[13], research in this cutting-edge field appears particularly promising.
This Master Thesis aims at a particular characterization method to describe physical processes in the complex BC-BJ solar cell concept. The results of this work are part of a larger project at the Universität Konstanz in the field of BC-BJ solar cells. While the benefits of moving the front contacts to the back are evident, the realization of such a cell's rear side remains challenging. To this day, essential characterization methods to investigate physical effects on the rear side, such as tunneling recombination between the two highly doped regions, are scarce. In this work, single co-diffused pn-junctions are studied with the aim to learn more about these effects on the rear side.

A brief overview of this work's structure is given in the following.

Chapter 2 presents the knowledge base that is required to understand this work. The working principle of a solar cell, the recombination mechanisms in a cell and the contact metallization are explained in this context. Furthermore, the solar cell structure of a BC-BJ solar cell is compared to that of a standard solar cell and the J-V curve as well as the Free Energy Loss Analysis are described in this chapter.

Chapter 3 concerns itself with simulations that support the analysis chapter of this work. A comparison of simulation results obtained with Quokka and Sentaurus Synopsis is carried out, in which the J-V curve characteristic quantities and the Free Energy Loss Analysis results are used. In addition, simulations of the pn-junction, that is to be experimentally realized, are performed.

Chapter 4 is the main chapter of this work. Physical effects, difficulties and solutions to these challenges are presented along the samples' processing procedure. A key part of this chapter is the local removal of dielectric material with photolithography or laser ablation to pattern the pn-junction or the contact openings. A special focus lies on the creation of the pn-junction with and without an intrinsic gap region with laser ablation. Furthermore, the contact metallization, the effective lifetime and surface passivation are investigated in this chapter. Finally, the method to characterize the pn-junction and J-V curve characteristic quantities obtained with this method are presented.

Chapter 5 summarizes the results obtained in this work and gives an outlook for further studies related to this work.

2 Physics of Solar Cells

This chapter summarizes the physical background that is required for the analysis of this work. Most content of this chapter is well established physics that can be found in text books such as [14]–[18], therefore not all passages will be provided with a citation. This chapter is narrowed down to silicon (Si) photovoltaics with single junctions, due to the particular topic of this work.

2.1 Working Principle

2.1.1 Semiconductor Material

Solid-state material can be categorized into insulators, semiconductors or conductors. Conductors are defined by a low electrical resistivity (10^{-6}-10^{-4} Ωcm[18]), while insulators are characterized by a high electrical resistivity (10^{8}-10^{18} Ωcm[18]). This difference in resistivity results from the allowed energy bands for the different material classes. In the ground state, the energy bands of insulators are either completely full or completely empty, which leads to a band gap. The band gap is a forbidden energy sector, with no available energy states for electrons. At finite temperatures, thermal agitation results in a continuous transition of electrons between the valence and the conduction band. Solid-state material, that is an insulator for $T = 0$, while featuring a band gap that is small enough to allow measurable intrinsic conductivity at a temperature below the melting point, are called semiconductors. The semiconductors' band gaps are typically in the order of $\sim$1 eV[18] and the Fermi energy ($\mathrm{E_F}$) is found within this energy gap. The resistivity of a semiconductor depends on several factors, such as the material's temperature, the illumination intensity (see Chapter 2.1.3) and the concentration of impurity atoms (see Chapter 2.1.4).

2.1.2 Photon Absorption

In a solar cell, photon absorption in the semiconductor material is the main process for charge carrier generation. While photons with energies below the band gap energy are not absorbed by electrons in a semiconductor, photons with energies exceeding the band gap energy can be used for an electron transition. The band gap energy is defined as

$$\mathrm{E_g} = \mathrm{E_c} - \mathrm{E_v}$$

where $\mathrm{E_c}$ is the energy level at the bottom of the conduction band and $\mathrm{E_v}$ at the top of the valence band. The band gap energy corresponds to the minimum required energy to excite an electron from the valence band to the conduction band and is $\mathrm{E_{g,Si}} = 1.12$ eV wide in Si[18]. According to the Bloch theorem, the band structure of a crystalline solid can be reduced to the Brillouin zone, which is the Wigner-Seitz cell in the reciprocal lattice[17]. This band structure of Si is visualized in the so called energy band diagram in Figure 2.1.

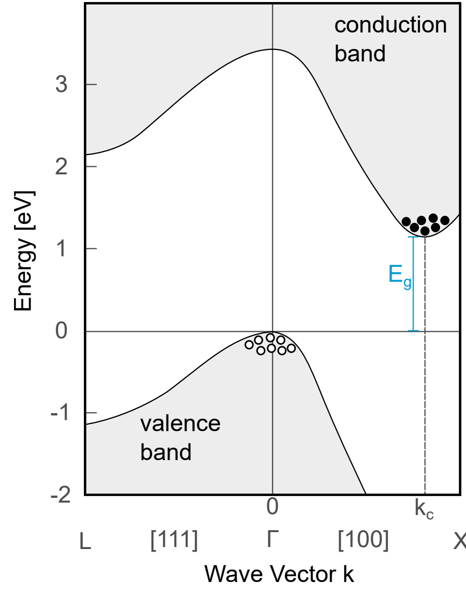

Figure 2.1: Silicon energy band diagram (based on[18]).

The energy band diagram displays the energy-momentum (E-k) relationship for carriers in the crystal lattice, where the momentum p is linked to the wave vector k such that $p = \hbar k$[17]. In the energy band diagram of Si, the maximum of the valence band is at $\mathrm{k} = 0$ and the minimum of the conduction band is at $\mathrm{k} = \mathrm{k_c} \neq 0$. As a consequence of energy and momentum conservation, an electron excitation from the maximum of the valence band to the minimum of the conduction band requires a change in momentum in addition to the change in energy. A semiconductor with this property is called an indirect semiconductor, while a semiconductor is called direct if no change in momentum is required.
The type of semiconductor has a direct consequence on photon absorption. On the one hand, a necessity for electronic photon absorption in in-/direct semiconductor types is that the photon energy exceeds the band gap energy because of the missing energy levels in this forbidden energy gap. On the other hand, in-/direct semiconductor types differ in their absorption mechanism because the indirect semiconductor requires the additional phonon interaction for the conservation of momentum. This makes photon absorption less likely for indirect semiconductors than for direct semiconductors. Electrons that are excited with energies exceeding the band gap energy, emit excess energy by exciting phonons (thermalization). Although this is generally a several step process, because phonons in solids have low energies up to 0.05 eV, it proceeds on a ps timescale[16].

The photon flux $\phi_\gamma(x)$ entering the Si layer decreases exponentially as function of the penetration depth x. Each photon that is absorbed in Si, as a result of a photon-phonon-electron interaction, generates one electron-hole pair (explained in Chapter 2.1.3; no multiple carrier generation). The resulting generation profile $G_\gamma(\lambda, x) = G_e(\lambda, x) = G_h(\lambda, x)$ is dependent on the absorption coefficient α and the photon wavelength λ according to the Beer–Lambert law[16]

$$G_\gamma(\lambda, x) = \alpha(\lambda)\phi_\gamma(\lambda, x = 0)\exp(-\alpha(\lambda)x) \tag{2.1}$$

where α can be calculated from the extinction coefficient κ such as[17]

$$\alpha = \frac{4\pi\kappa}{\lambda} \tag{2.2}$$

A generation profile, used for simulations in Chapter 3, is displayed in Figure 2.2. The exponential decay described by formula 2.1 is apparent for the development starting from a depth

of about 50 nm. This generation profile was obtained by ray tracing, while taking into account the geometry of the front surface as being texturized in pyramid-like shape. Due to this texture, the Si area along the wafer's thickness increases from the pyramids' tips up to the point of full area coverage when reaching the bulk material. This effect is accounted for in the ray tracing simulation[19],[20], leading to a decreased generation rate in the textured depth. A pyramid size of less than 50 nm was chosen to minimize the effect on the generation profile. The common pyramid sizes are in the order of several μm. The reason for the relatively large pyramid size is to obtain a homogeneous Anti-Reflective Coating (ARC) thickness with an ARC that is usually thinner than 100 nm.

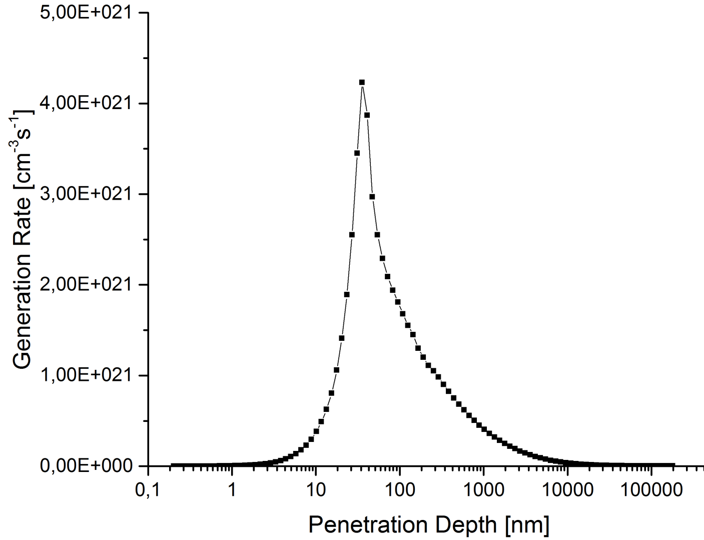

Figure 2.2: Generation profile obtained by ray tracing for a 180 μm thick silicon wafer.

Knowing the generation profile, one can calculate the total photogenerated current density J_{gen} by integrating over the cell thickness d as well as over all wavelengths contained in the photon flux ϕ_γ[16]

$$J_{\text{gen}} = q \int_0^d \int_{\lambda_1}^{\lambda_2} G_\gamma(\lambda, x) \mathrm{d}\lambda \mathrm{d}x \tag{2.3}$$

The generation profile and the calculation of the total photogenerated current density are relevant in the simulation in Chapter 3.

2.1.3 Charge Carriers

As explained in Chapter 2.1.2, photon absorption by an electron in a semiconductor can excite the electron from the valence band to the conduction band. This leads to an unoccupied electron-state in the valence band, an electron deficiency. This deficiency can shift in location when it is filled by a neighboring electron and, hence, contributes to the electrical current in the semiconductor. Therefore, the hole can be introduced as a fictitious particle with a positive charge $q_{\text{h}} = +e$. Holes are used as an equivalent description in regions and situations of high electron energy state occupation (e.g. in the valence band), since the description is less complicated as the holes form an ideal gas[16].
The electron-hole pair generated by photon absorption is only weakly bonded in semiconductors

such as Si and the two charge carriers are therefore considered to be free charge carriers. The existence of free charge carriers due to illumination of a semiconductor explains that illumination lowers its resistivity.
Charge carriers in a semiconductor perform thermal motion at room temperature. This random thermal motion is influenced by scattering from collisions with scattering centers such as impurity atoms and lattice atoms. The impurity atoms exert Coulomb force interaction on the charge carrier, while the lattice atoms vibrate with higher temperature, which disturbs their periodic potential and allows the energy transfer between the free charge carriers and the crystal lattice. Other than the thermal motion, carrier drift and diffusion play an essential role in doped (see Chapter 2.1.4) semiconductors. If a small electric field is added in the semiconductor, the charge carriers are accelerated along the field and therefore a drift velocity is added to the thermal motion. A diffusion current is created by a charge carrier concentration gradient with the result of charge carriers moving towards an energetically favorable region with less charge carriers of the same polarity.

2.1.4 Doping, Profiles and Sources

Doping

The addition of impurities into the crystal lattice of a semiconductor material is called doping, the semiconductor is then called extrinsic. Doping is used to vary the resistivity of the material or to create an internal electric field.

Table 2.1: The part of the periodic table concerning semiconductors (based on[18]).

Period	Column II	III	IV	V	VI
2		B	C	N	O
3	Mg	Al	Si	P	S
4	Zn	Ga	Ge	As	Se
5	Cd	In	Sn	Sb	Te
6	Hg		Pb		

The Si atom has two full inner shells with tightly bound electrons and four valence electrons, it is therefore found in period 3 and column IV of the periodic table (see Table 2.1). When Si forms a crystal (diamond lattice), the four valence electrons are shared with the atom's four neighboring atoms for covalent bonding. Covalent bonds are formed by electron pairs between atoms (see Figure 2.3a). A semiconductor is called intrinsic, undoped or i-type, if it is pure with no (significant) dopant atoms in the crystal lattice.
Donor or acceptor atoms are introduced into the crystal lattice to dope a semiconductor. Donor atoms have at least one additional valence electron, while acceptor atoms have less valence electrons than the atoms of the intrinsic semiconductor. In this work, only discrepancy of one valence electron is considered because the typical donor element phosphorus (P) and acceptor element boron (B) are used for Si doping (see Table 2.1).
Due to the substitution of a Si atom for a donor atom, an additional electron is introduced to the lattice (see Figure 2.3b). A P atom yields this electron (ionization) because it is weakly bonded to the nucleus. When a multitude of donor atoms replace Si atoms in a Si crystal, the semiconductor becomes n-type because of the added free negative charge carriers. A substitute acceptor atom that takes the position of a Si atom brings an additional hole to the lattice, for it is missing one electron to form the fourth valence band with its neighboring atoms (see Figure

2.3c). Holes introduced by B atoms are only weakly bonded and are therefore easily parted with (ionization), this makes the semiconductor p-type because it has free positive charge carriers. The free charge carriers generated by ionization of the doping atoms reduce the resistivity of the material. If both, donor and acceptor atoms, are locally present in the crystal lattice, the electrons yielded by donors are integrated by acceptors (analogous for holes), therefore only the difference between donor and acceptor concentration is of relevance for the overall amount of free charge carriers[21] (if all charge carriers are electrically active; defined in Chapter 2.1.4). In solar cells, one distinguishes between minority and majority charge carriers. Minority charge carriers are outnumbered by majority charge carriers in a semiconductor, such as positive charge in a n-type semiconductor.

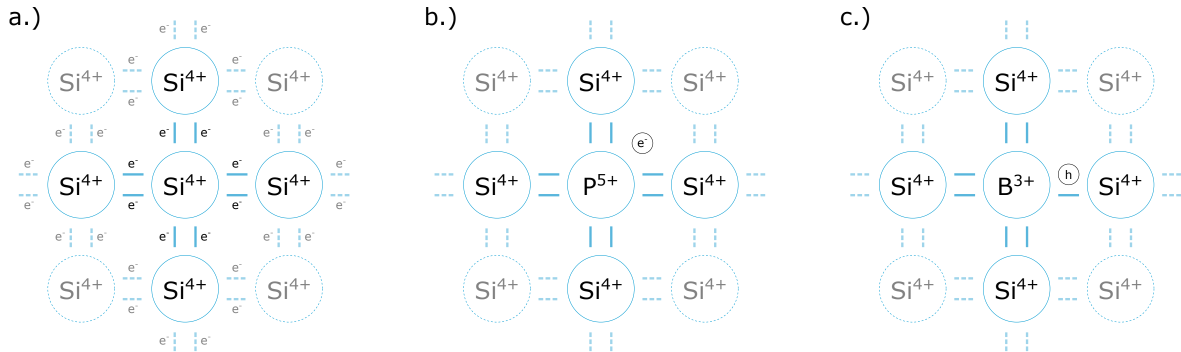

Figure 2.3: Schematic illustration of a.) intrinsic silicon crystal, b.) n-type Si with phosphorus doping, c.) p-type Si with boron doping (based on[17]).

P and B are shallow impurities, because they demonstrate a low ionization energy of about 45 meV[17] that is comparable to the thermal energy $k_B T$ at room temperature. The complete ionization of P and B at room temperature is a reason for their extensive use as doping elements for Si semiconductors. The dopant is usually introduced in doping concentrations of $10^{15} - 10^{21}$ cm^{-3} into Si, which has a density of atoms in the order of 10^{23} cm^{-3}[16]. Doping in this work is achieved by diffusion at temperatures from 750 °C to 1000 °C from gaseous or solid doping sources.

Relevant Dopant Sources

In this work, dopants are diffused into the Si crystal from gaseous and solid dopant sources. Phosphorus Oxychloride ($POCl_3$) is used as the gaseous dopant source[22] for P, while borosilicate glass (SiO_x:B) is the solid B dopant source.
During the diffusion process, $POCl_3$ gas can be introduced into the furnace, which decomposes in the gas phase into Phosphorus Pentoxide (P_2O_5), then oxidizes at the silicon surface and consequently results in a P diffusion into the Si bulk[23]. Ghoshtagore proposed a model in 1975[24] starting with a thick SiO_2 layer on the Si substrate, where the oxidation reaction forms a Phosphorus Silicate Glass (PSG). In this model, the top layer of the PSG consists of a SiO_2/P_2O_5 mixture that is liquid at diffusion temperature due to a high P_2O_5 content. Micard et al. were able to apply this model to PSG formation on Si because of a thin silicon oxide (SiO_x) layer that forms within the PSG on the Si substrate and acts as a diffusion barrier, similar to the one in the model of Ghoshtagore. With this model, Micard et al. successfully interpret experimentally obtained diffusion profiles[23].
In contrast to the gaseous diffusion source, SiO_x:B is applied as solid dopant source. Therefore Chemical Vapor Deposition (CVD) is used to deposit the thin film of solid material. During this chemical process, the Si wafer is exposed to several volatile precursors that react or decompose

on the wafer. Two CVD techniques are used in this work, the Atmospheric Pressure CVD (APCVD) and the Plasma-Enhanced CVD (PECVD). The two techniques differ primarily in two points: while the APCVD operates at atmospheric pressure with thermally activated chemical reaction of the precursors, the PECVD operates at pressures around 10^{-6} bar and applies a plasma to activate the reaction molecules. The plasma employment and the vacuum are the key advantages of PECVD which allow a wider deposition temperature range than APCVD. Studies investigating the composition of the SiO_x:B layers have been previously carried out in this research group[25]–[29], these findings are used in this work. Heating the coated wafer in a diffusion furnace leads to a diffusion of B from the SiO_x:B layer into the Si substrate. The SiO_x:B layer can also be coated with an additional capping layer to prevent B degassing and P in-diffusion during a $POCl_3$ co-diffusion[25]. It is to be noted, that such capping layers can influence the composition of the SiO_x:B layer during deposition and during the diffusion process (e.g. B can diffuse into the capping layer). Possible capping layers can be SiO_x[30],[31] and silicon nitride (SiN_x)[32]. In this work SiO_x:B is typically capped by SiN_x.

Diffusion and Co-Diffusion

A brief look will be taken at the diffusion process applied to diffuse dopants into the Si substrate. The two major parameters that influence the diffusion process in the furnace are temperature and duration of the diffusion process. These parameters are usually adapted to suit the required sheet resistivity R_{sheet} or more precisely the doping profile. The sheet resistivity gives information about the resistance of the thin doped layer that is ideally electrically separated from the bulk by a pn-junction (see Chapter 2.1.5) for further measurement of R_{sheet}. The higher the doping in that layer, the lower the sheet resistivity. Measurements of the doping profile resolve the doping intensity as a function of the film depth and therefore give a more accurate insight into the origin of R_{sheet}. Earlier work of the research group at the Universität Konstanz has revealed that B diffusion from SiO_x:B above 900 °C for about 1 h[25],[26] and P diffusion from $POCl_3$ at around 830 °C for about 40 min (20 min $POCl_3$ with gas)[25],[33] achieve the desired results with the matching SiO_x:B layer composition and gas flows.

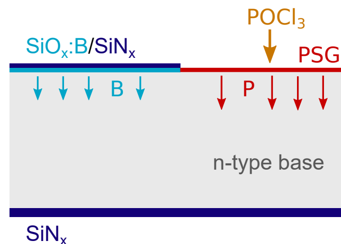

Figure 2.4: Cross section schematic showing the diffusion process from SiO_x:B (solid doping source) and $POCl_3$ (gaseous doping source) of two adjacent regions that are to be oppositely doped (not to scale).

In this work, co-diffusion is aimed for, which allows for the simultaneous formation of all the required doped layers in the same diffusion step[22],[28],[34],[35]. This has the potential to shorten the process flow and in consequence to decrease the process costs. Due to the different temperatures needed for diffusion of B and P, a sequential diffusion is chosen in this work. First B is diffused at temperatures above 900 °C, followed by introduction of the $POCl_3$ gas flow at lower temperature. That way the parameters for both diffusion processes can be adapted independently, while keeping the advantage of diffusing both dopants in one high temperature step (see illustration in Figure 2.4).
It is to be mentioned, that an elaborate simulation of P diffusion from $POCl_3$, of B diffusion

from SiO_x:B and of P diffused through SiO_x:B into Si bulk material is numerically performed by Gloger in his dissertation[25].

Doping Profiles

Diffusion is the redistribution (here at high temperature) of initially localized atoms, where the movement is driven by the impurity concentration gradient. As set out earlier in this chapter, B and P occupy substitutional positions in Si and form covalent bonds with neighboring Si atoms[36]–[38]. Interaction between the dopant atoms and intrinsic point defects, such as vacancies and interstitial atoms, is the prime mover of the diffusion process[36],[38] while direct interchange of an impurity in a substitutional position with a neighboring Si atom is unlikely because of the strong covalent bonds with the neighboring atoms[39]. Therefore the diffusion coefficient is highly dependent on intrinsic point defects.
A complex diffusion process needs to be considered for P diffusion from an infinite source at the surface, such as from $POCl_3$ gas[23]. Fair and Tsai proposed a model for P diffusion in 1977[40] that relies on the ideas of Schwettmann and Kendall[41],[42] as well as on the model of Yoshida[43],[44]. The model proposes, that in the region of high electron concentration close to the surface, the ionized vacancies $V^{=}$ (double negatively charged) form pairs $(PV)^{-}$ with the ionized P atoms P^{+}. These charged pairs lead to an increased diffusion. The pairs discharge to neutral pairs $(PV)^{-} \rightarrow (PV)^{x} + \mathrm{e}^{-}$ and dissociate $(PV)^{x} \rightarrow P^{+} + V^{-}$ at the kink concentration because the Fermi-level coincides with the second acceptor level of $V^{=}$ at this concentration. After the kink begins the tail region, where the freed P atoms dominantly diffuse via numerously available interstitial atoms. This results in a kink-and-tail doping profile. The kink of the doping profile is favorable for the contact formation on the one hand, on the on the other hand it is disadvantageous for the charge carrier lifetime because of the increased recombination activity[45] (see Chapter 2.2).
It is to be mentioned, that the dopant B is generally entirely electrically active in Si[46],[47], while highly concentrated P in Si is usually partly electrically inactive due to P in a precipitated phase[33],[46],[48],[49].

The dopant diffusion under steady state conditions in Si is described by Fick's first law

$$\vec{J} = -D \cdot \mathrm{grad}\,(c(r,t)) \tag{2.4}$$

The diffusion flux $\vec{J}$ is proportionally linked to the dopant concentration gradient $c(r,t)$ by the diffusion coefficient D.
According to dopant conservation, a time dependent concentration change corresponds to a local change of the diffusion flux:

$$\frac{\partial c(r,t)}{\partial t} = -\mathrm{div}\left(\vec{J}\right) \tag{2.5}$$

In the following, diffusion is considered in one dimension only, therefore one-dimensional equations will be applied. In the case of an infinite dopant source $c(0,t) = c_s$ at the surface and an undoped bulk material $c(\infty,t) = 0$, a complementary error function is obtained. This approach applies quite well for B diffusion from a SiO_x:B layer, where the SiO_x:B layer functions as infinite dopant source[25],[50].
A Boron Rich Layer (BRL) can arise during B diffusion from SiO_x:B layers. In that case, a very high concentration of boron forms at the Si surface (boron pile up) and transforms the surface into a BRL, for example according to[51],[52]

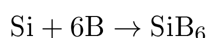
$$\mathrm{Si} + 6\mathrm{B} \rightarrow \mathrm{SiB_6}$$

B misfit dislocations create tension and can even glide from the surface to the Si bulk[53]–[55] inflicting on the wafer's lifetime. Additionally, the high B concentration on the surface leads to a high charge carrier recombination. BRL formation is therefore avoided in this work by choosing an amount of B in the SiO_x:B layer that is low enough to prevent BRL formation.
A hydrophilic Si surface after immersion in highly concentrated solution of Hydrogen Fluoride (HF) in water (in the following called HF solution) can be a sign for a BRL[52],[56] because a lowly doped Si surface is likely to be hydrophobic after a dip in HF solution[54],[55].

2.1.5 pn-Junction

Consider adjacent n- and p-type semiconductors in contact with one another. The majority charge carriers from both semiconductor types diffuse in the border region (diffusion current, see Chapter 2.1.3) and recombine (see Chapter 2.2). This creates a depletion region at the junction with less free charge carriers than in the bulk. The recombined charge carriers leave behind charged immobile ions at the impurity sites, leading to a space charge region (SCR) between positively charged ions in the n-type semiconductor and negatively charged ions in the p-type semiconductor. This SCR builds up, until the drift current (see Chapter 2.1.3) resulting from the electric field ϵ compensates the diffusion current. This electric field leads to band bending with the result that the Fermi energy, as defined by the Fermi-Dirac function, is at a constant level in both regions (without illumination).

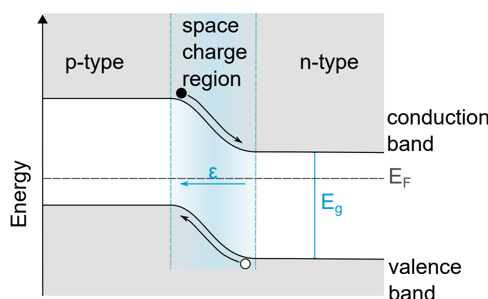

Figure 2.5: Schematic of a pn-junction, which displays the energetically favorable flow direction for electrons and holes across the pn-junction (based on[16]).

Solar cells are designed to generate an electrical current when illuminated. Charge carriers generated in Si by photon absorption (see Chapter 2.1.2) randomly diffuse in the semiconductor, resulting in a net zero current flow. The pn-junction in a solar cell attracts minority charge carriers to pass the junction, while repelling majority charge carriers. It therefore creates a drift current with a preferred flow direction for the electrons and holes (see Figure 2.5), which results in a net current of the minority charge carriers.

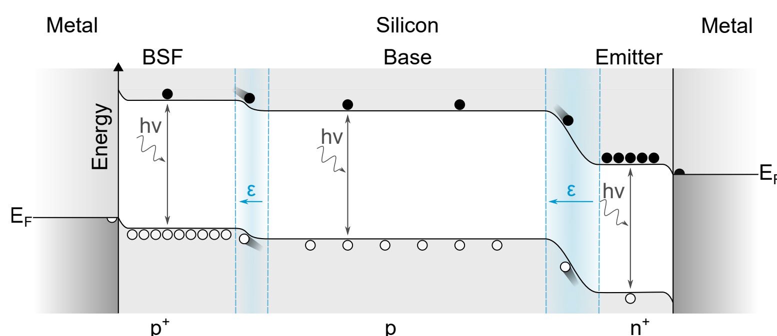

Figure 2.6: Schematic band diagram of a conventional solar cell (based on[57]).

In general, four doped regions can be differentiated in solar cells: the base, the Back Surface Field (BSF), the Front Surface Field (FSF) and the emitter. The base is the bulk material, that is either n- or p-type and commonly features a low dopant concentration. The BSF and/or FSF, depending on the layout of the solar cell, is of the same doping type than the base and is highly doped. In contrast, the emitter is highly doped with opposite doping. This creates a pn-junction between the emitter and the surrounding regions and commonly a flatter junction between the highly doped BSF/FSF and the base.
The working principle of an assembled conventional solar cell (see Chapter 2.4.1) is depicted by the band diagram in Figure 2.6. Due to illumination, the solar cell is not in its thermodynamic equilibrium and the electron and hole concentration is raised (see Chapter 2.1.3). This leads to two separate quasi-Fermi levels at different energies for the two charge carrier types. Free charge carriers are created by photon absorption (detailed in Chapter 2.1.2) in one of the four regions of the solar cell. If the charge carriers do not recombine, they are separated by the p^+p-junction and the pn-junction so that electrons are accelerated into the emitter and holes into the BSF. The separated charge carriers are then extracted by metal contacts that have Fermi energies roughly at the same energy level than the Fermi energy of the corresponding majority charge carriers in the contacted region (ohmic contact, see Chapter 2.3).

2.2 Recombination Loss and Passivation

In this chapter the loss mechanisms of a solar cell are briefly discussed, followed by a description of surface passivation with the focus on passivation layers used in this work. The specific recombination processes taking place between adjacent highly doped p- and n-doped regions are specified.

2.2.1 Loss Mechanisms

Thermalization, optical and electrical loss are among the three major loss mechanisms of solar cells.
Thermalization loss is an intrinsic loss mechanism, where excess photon energy ($E_\gamma > E_g$) is dissipated as heat (thermalization) within a ps timescale due to inelastic scattering between the charge carriers and phonons[16]. Currently there is no technology in solar cell physics that can make use of the thereby dissipated energy. While thermalization loss is an intrinsic loss, that cannot be reduced in a single junction solar cell, there are concepts to moderate optical loss. A textured front surface with an ARC is one example of how photon capture is enhanced. Optical losses occur when photons impinging on the solar cell do not generate excess charge carriers. This can be due to reflection on the front surface, due to photons that are not absorbed within the Si bulk or due to free carrier absorption, where a photon is absorbed by a charge carrier that is in an excited state already.
An ongoing research topic is charge carrier recombination loss (electrical loss, ohmic losses left aside). This recombination process takes place to restore the equilibrium of the system after excess carriers have been generated due to optical excitation. Radiative recombination, Auger recombination and Shockley-Read-Hall (SRH) recombination are distinguished. They combine to the resulting minority charge carrier lifetime of[17]

$$\tau^{-1} = \tau_{\mathrm{rad}}^{-1} + \tau_{\mathrm{Auger}}^{-1} + \tau_{\mathrm{SRH}}^{-1} \tag{2.6}$$

The sole recombination process emitting a photon, is called radiative recombination. It is the reverse of the absorption process discussed in Chapter 2.1.2, radiative recombination therefore takes place in the ms timescale[16] in Si. Auger recombination describes the recombination

process where a free electron relaxes into the valence band while transferring its energy to another free charge carrier which is excited to a higher energy level in the same band and thermalizes as a consequence[58]. This recombination mechanism is especially relevant in highly doped Si. The charge carrier lifetime for Auger recombination depends on the excess charge carrier density Δn and the ambipolar Auger-coefficient $C_a = 1.66 \cdot 10^{-30}$ cm^6/s (at room temperature) as follows[59]

$$\tau_{\text{Auger}}^{-1} = (\Delta n)^2 \cdot C_a \tag{2.7}$$

Deep level impurities[60] (as opposed to shallow impurities, see Chapter 2.1.4) cause recombination loss, as they function as stepping-stone for free charge carriers between the two bands. The charge carrier lifetime for SRH recombination τ_{SRH} depends on the thermal velocity ν_{th}, the trap density N_{t} and the capture cross section for charge carriers σ[17]

$$\tau_{\text{SRH}} = \frac{1}{\nu_{th} \cdot N_{\text{t}} \cdot \sigma\left(\text{E}_{\text{t}}\right)} \tag{2.8}$$

where σ is determined by the energetic level of the trap states E_{t}.
Due to an increased number of traps at the wafers surface, this so-called SRH recombination mainly occurs on the surface of high purity wafers. Consequently, surface passivation (Chapter 2.2.2) is key to increase the charge carrier lifetime of Si wafers.

2.2.2 Surface Passivation

The surface of a Si wafer corresponds to an abrupt interruption of the crystal lattice. Therefore, atoms lack neighboring atoms and have unpaired valence electrons that introduce various energy levels in the band gap, so called surface states. Surface passivation reduces the surface recombination, hence, an improved passivation is associated with a decrease of the recombination parameter J_0[61] and an increase in the effective minority charge carrier lifetime τ_{eff}.
It is to be mentioned that dielectric surface passivation was first reported by Atalla et al. in 1959 with a SiO_2 passivation layer[62]. Surface passivation can be realized by reducing the number of surface states (chemical passivation) or by reducing the concentration of one charge carrier type at the surface (field-effect passivation).
Chemical passivation accounts for the binding of surface valence electrons by a thin layer of material with a wide band gap. The layer is often assisted by hydrogen atoms that are either incorporated in the deposited layer or introduced by hydrogen anneal. Passivation layers containing stable charge that repels one charge carrier type (ideally the minority charge carriers) exert field-effect passivation. This prevents charge carrier recombination at the surface, since both charge carrier types are required for recombination.
One of the passivation layers used in this work is hydrogenated intrinsic amorphous silicon (i)a-Si:H (in the following called a-Si), which is a semiconductor material[63]. Its absorption characteristic resembles that of a crystal semiconductor with a direct bandgap of 1.6 eV[17]. It is deposited by PECVD with a sole silane gas flow resulting in a non-columnar layer on the substrate which is stable at a high passivation level during long thermal treatment[64]. The passivation mechanism is purely chemical without field-effect passivation[65]. Though, excellent chemical passivation with a-Si on c-Si surfaces has been achieved with a single layer or in a stack with dielectrics[66]–[69]. a-Si layers with SiN_x capping that show no degradation under UV irradiation have been shown[70]. The a-Si coated Si substrate is thermally annealed in a post-deposition treatment to increase the chemical passivation by incorporated hydrogen[25],[71]–[73].
Another passivation layer used is amorphous Al_2O_3 (in the following referred to as Al_2O_3), which is deposited by Atomic Layer Deposition (ALD) in an FlexAL ALD from Oxford Instruments. Al_2O_3 is an insulator material with an optical band gap of 6.4 eV[63]. It yields a high chemical

surface passivation quality[74],[75] and a high density of fixed negative charge which creates a strong field effect passivation that is ideal to passivate p-type surfaces[63],[76],[77]. It is not necessarily suited for passivation of highly n-doped (n^+-doped) surfaces, unless activated with a short high-temperature firing process (800 °C)[75]. In general, the passivation layer requires an activation by a thermal post-deposition treatment of several minutes at a temperature of around 400 °C[75].

In this work n- and p-type areas on one and the same sample are passivated with one single passivation layer. n- and p-doped surfaces are not equally well passivated by both passivation layers, however, as will be detailed in Chapter 4.4.4. Using independent passivation layers for adjecent highly p- and n-doped surfaces has been taken into consideration by Chen et al. to further decrease the recombination current and, hence, to increase the overall performance of the solar cell[78]. According to the published study in[78], this passivation theme could not be realized experimentally due to fabrication difficulties. The conclusion for this work is, that no easily applicable method is available yet for independent passivation layers on adjacent highly doped areas.

The SiN_x deposited as capping layer and ARC is grown by ammonia (NH_3) and silane (SiH_4) by PECVD and therefore results in SiN_x:H, a silicon nitride that incorporates a considerable amount of hydrogen. The incorporation of hydrogen is an advantage for passivation, because in a double layer structure the SiN_x:H capping layer indirectly influences the surface passivation due to its hydrogen reserve. Since hydrogen saturates the unpaired valence electrons at the surface[78],[79], double layer passivation generally outperforms single-layer passivation[78].

2.2.3 Recombination at the pn-Junction

In this work, loss mechanisms described in Chapter 2.2.1 are minimized with the objective to analyze the recombination occurring at the pn-junction on the rear side of the cell. This recombination process is highly related to the BC-BJ solar cell structure due to the adjacent highly p- and n-doped regions, hence it is the most relevant recombination mechanism in the context of this Master Thesis.

Local recombination paths (see Chapter 2.2.1), such as band-to-band recombination (Figure 2.7a) and SRH recombination (Figure 2.7b), are of high relevance at the pn-junction on the rear side of the solar cell, because of the highly doped regions and an increased number of trap states at the surface and in the highly doped regions[45]. Besides these local recombination paths, also tunneling recombination paths have to be considered at the junction of highly doped regions because of the sharp change in doping.

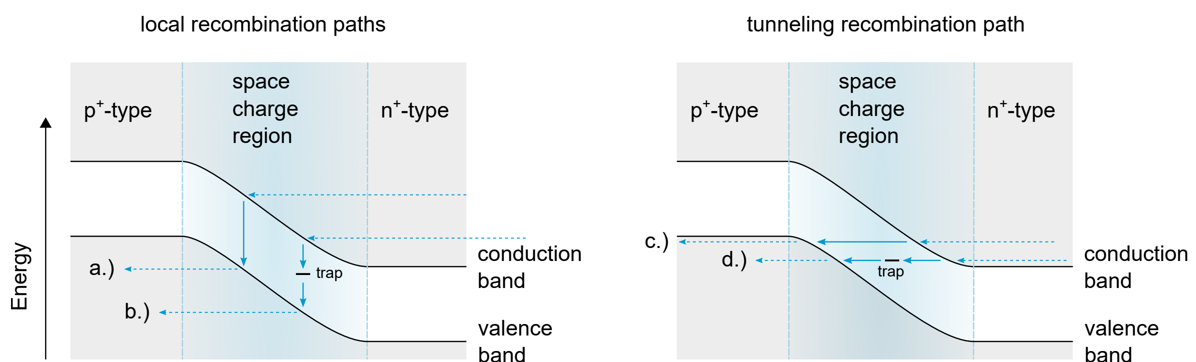

Figure 2.7: Charge carrier recombination paths at a highly doped pn-junction; a.) Band-to-band recombination, b.) SRH recombination, c.) direct tunneling recombination, d.) trap assisted tunneling recombination; (based on[80]).

Leaving no intrinsic gap between the two highly doped regions on the rear side of a BC-BJ solar cell involves the opportunity for charge carriers to recombine by tunneling through the SCR of the pn-junction[81]–[84]. In that case, the wave function of the charge carriers penetrates into and through a potential barrier, therefore the tunneling probability of the charge carriers is unequal zero.
It is possible to check solar cells for tunneling recombination by applying a reverse bias voltage. The break down voltage is a function of the SCR width and for a breakdown voltage below $4E_g/q = 4.4$ V for Si, tunneling recombination is the mechanism responsible for the breakdown[17]. Direct tunneling recombination (Figure 2.7c) is possible by a sharp change from high p-doping to high n-doping that creates a thin SCR and therefore results in a breakdown at low reverse bias voltage[85],[86].
Already in 1979 Pankove and Tarng observed that charge carriers could recombine by tunneling through trap states at the Si surface of adjacent p- and n-type regions covered by an insufficiently passivating layer[87]. This effect became apparent because the effect was much lower for an a-Si passivation layer than for a SiO_2 passivation layer. For this trap assisted tunneling (Figure 2.7d) traps are stepping-stones for free charge carriers to cross the pn-junction[88]. Traps in the SCR are likely to lower the breakdown voltage at applied reverse bias voltage[89]–[91]. Recombination at the pn-junction is related to surface passivation since unpassivated traps at the surface are a major source for SRH recombination and trap assisted tunneling recombination. Different passivation layers therefore possibly have a major impact on the recombination process at the pn-junction.
As mentioned earlier, tunneling recombination is more likely across a sharp pn-junction. By introducing an intrinsic (base doping, see Chapter 2.4) gap between the two highly doped regions, these regions are separated, leading to a flat band bending. This highly decreases the probability of tunneling recombination and possibly alters the local recombination paths.

2.3 Metallization

Contacting a semiconductor with a metal, builds up stable space charge at the interface that forms a potential barrier. If the barriers height is much larger than $k_B T$, the barrier is called a Schottky barrier. It is to be mentioned that current transport across the junction is mainly due to majority charge carriers, which contrasts to charge carrier transport across a pn-junction (see Chapter 2.1.5). The specific contact resistance is to be low for a solar cell device. An ohmic contact, that is defined by negligible resistance relative to the total resistance of the device, is therefore favorable. For a low contact resistance, a low barrier height and a high doping concentration at the surface are beneficial[17]. Metals such as Aluminum (Al) and Titanium (Ti) form ohmic contacts on n- and p-type Si[17].
The metallization is performed on contact openings to directly contact the Si substrate. For this purpose, the dielectric layers covering the Si substrate are removed in the area of the contact openings (see Chapter 4.2.4). In a consecutive processing step, these opened areas are metallized. An electron gun is used to metallize substrates with thin metal layers, such as Ti, Pd, Ag and Al, via evaporation deposition. The entire process takes place in a vacuum with a pressure below $5 \cdot 10^{-6}$ mbar as to increase the mean free path of evaporated particles. An electron beam is directed at the source metal that evaporates as a consequence. Due to the vacuum in the chamber, the vaporized metal particles travel directly towards the substrate, where they condense on the surface. This way metal layers of varying thickness can be deposited on the substrate. With this technique, Al (500 nm)/Ag (200 nm) is deposited on a-Si passivated surfaces and Ti (50 nm)/Pd (50 nm)/Ag (500 nm) on Al_2O_3 passivated areas. Using Ti/Pd/Ag contacts avoids possible p-doping of the Si substrate on the n-type contact by Al[92].
The a-Si passivation layer is likely to be only partly removed after the contact opening process.

The contacts to substrates passivated with a-Si, are therefore performed with use of the 'local Contacts to a-Si passivated solar cells by Means of Annealing' (COSIMA) technique according to the dissertation of Plagwitz[93]. COSIMA contacts are generally formed with Al on an a-Si passivated surface. The a-Si dissolves and recrystallizes within the Al during the annealing process or during the deposition process. As a result, the original a-Si layer is entirely replaced by Al. In the context of this work, COSIMA contact formation is useful to dissolve remaining a-Si in the Al contact. The contact is furthermore covered by silver (Ag) to avoid oxidation of the Al.

2.4 Solar Cell Structure

2.4.1 Standard Solar Cell

The conventional state-of-the-art c-Si solar cell is presented in the following (see Figure 2.8). The wafer is commonly approximately 180 μm thick. The base is lightly B doped and, hence, is a p-type material with a resistivity around 1 Ωcm, which corresponds to an acceptor doping concentration of $N_A \sim 1.5 \cdot 10^{16}$ cm^{-3}[57]. The BSF is located at the rear side and is achieved using an Al paste covering the entire surface. The paste forms an alloy with Si during the firing step and leads to an Al doped p^+-region (see Table 2.1) with a depth of up to 10 μm ($N_A \sim 10^{19}$ cm^{-3}[57]). In contrast, the emitter is highly n-doped with P on a textured front side with a depth of the doping profile below 1 μm and a surface donor doping concentration of $N_D > 10^{20}$ cm^{-3}[57]. A SiN_x layer of about 75 nm covers the front surface to act as an ARC and to passivate the surface with its high concentration of hydrogen (detailed in Chapter 2.2.2). The metallization of the front surface is performed with Ag paste that perforates the SiN_x layer and forms crystals in the Si during the firing step.

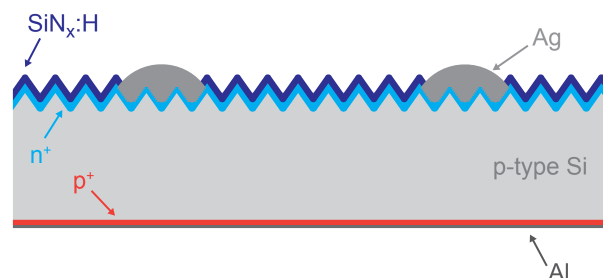

Figure 2.8: Schematic cross section of a conventional solar cell (not to scale, based on[57]).

2.4.2 Back Contact Back Junction Solar Cells - Advantages and Challenges

In contrary to standard solar cells, the contacts of both polarities are located on the rear side of back-contacted solar cells. Relevant for this work is the Back Contact-Back Junction (BC-BJ) solar cell, which features the contacted diffused regions (BSF and emitter) and the complete metallization on the backside. The most efficient single junction solar cells are achieved with this solar cell concept. The most recent world record of the Kaneka Corporation with an conversion efficiency of 26.3%[8], that surpasses the previous leading solar cell from Panasonic with a 25.6%[9] conversion efficiency by 0.7%, is to be mentioned. Both of these BC-BJ solar cells are hetero junction solar cells, which per definition contain a-Si layers. The most common alignment method for the metal grid on a BC-BJ solar cell is the interdigitated metal grid. Solar cells featuring this grid structure are called Interdigitated Back Contact (IBC) solar cells. The

concept of IBC solar cells was already introduced by Schwartz and Lammert in 1975[94],[95] for solar concentrator application and has been strongly improved since then. The characterization method presented in this work applies to BC-BJ as well as to IBC solar cells, which is why the more general term of BC-BJ solar cells is usually used in the following.

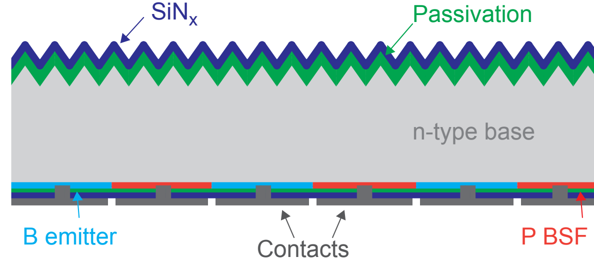

Figure 2.9: Schematic cross section of an IBC solar cell (not to scale).

A schematic cross section of an IBC solar cell is displayed in Figure 2.9. The display is tailored to suit the samples prepared in the course of this work. The base consists of a lowly doped n-type bulk. The front surface is textured and coated with a passivation layer and an ARC. Passivation layer and ARC can also be one and the same layer, and moreover the ARC can consist of multiple layers (here single-layer). The front can optionally be diffused with a n^+ doped FSF or a p^+ doped front floating emitter (FE). While an undoped front side may yield the best passivation quality[96], a FSF offers a less resistive path for electrons[97] and a FE for holes[98]. The rear side has alternating B and P diffused regions to form the emitter and the BSF. Ideal parameters for an efficient IBC solar cell imply a large emitter to BSF fraction for cells with industrially relevant widths[99]. Although the diffused regions in this schematic are adjacent to one another, without an intrinsic gap separating them, it is important to note, that IBC solar cells with an intrinsic gap region are produced in research[11],[12] and likewise samples with a gap are made in this work. The rear side is coated with a double layer of a-Si or Al_2O_3 and SiN_x, while the diffused regions are contacted separately.
The BC-BJ solar cell concept entails several advantages with regard to that of a standard solar cell. To begin with, placing the entire metal grid on the rear side, cancels out the optical shading that is typically caused by the front grid. This implies that a high passivation quality can more easily be realized because of fewer restricting conditions. One can take the freedom to chose a wider metallization for the grid, that is now located on the backside. Another advantage is brought about by moving the emitter from the front to the rear of the cell. In a standard solar cell, a large amount of charge carriers are commonly generated in the highly recombinative emitter region (see generation profile in Chapter 2.1.2). This results in a low blue response of the solar cell. With a high passivation quality of the IBC cell's front surface, the recombination in this crucial region can be minimized.

On the other hand, the IBC solar cell concept brings about several challenges. The necessity to use high silicon material quality and to precisely align diffused areas and the contact metallization are detailed hereafter.

Bulk Material

A high Si material quality is key for an efficient BC-BJ solar cell. This is due to the fact, that the emitter is located at the rear, while the charge carrier generation occurs predominantly near the front surface (see Chapter 2.1.2 for more information). Therefore minority charge

carriers not only have to diffuse through the entire wafer but they typically have to travel even further distance in lateral direction to reach the emitter on the backside of the wafer. As a consequence, a high minority charge carrier diffusion length is required. This does not solely imply the use of high quality mono-crystalline wafers, but also the use of n-type material instead of the more commonly used p-type material. Important is, that the effective minority charge carrier lifetime is maintained at a high level through the entire production process. It is to be mentioned, that the effective minority charge carrier lifetime and the diffusion length $L_{\mathrm{n,p}}$ are material recombination parameters that are linked by the diffusion constant $D_{\mathrm{n,p}}$ as follows $L_{\mathrm{n,p}} = \sqrt{D_{\mathrm{n,p}}\tau_{\mathrm{eff}}}$[17].
N-type material has several advantages over p-type material, which results in a higher τ_{eff}. One advantage of n-type material is, that no light-induced degradation associated with the boron-oxygen complex occurs[100],[101]. It is also less sensitive to laser-induced damage[101],[102], which is essential for the application of laser ablation as a technique to remove dielectric layers. Additionally, n-type Si material is less susceptible to metal impurities[102],[103]. Iron defects are likely to be present in Si material and inflict on the τ_{eff} of p-type Si more severely than for n-type material[103] due to a larger capture cross section for electrons than for holes[104],[105].
In conclusion, n-type Si material generally features lower recombination loss and a higher charge carrier lifetime over the course of the production process than p-type Si material.

Alignment

Careful alignment of the constituent is mandatory to prevent shunting. Shunting introduces an unwanted alternative current path for the light-generated charge carriers which causes power loss. Due to closely spaced grid lines of different polarity, this is a common difficulty in BC-BJ solar cells. Besides the shunt between the metal grids, shunting can likewise occur as an unwanted contact between a metal contact and a diffused region. This can happen for instance through pinholes if the BSF metallization is not slim enough to fit on the BSF region only but overlaps on the emitter region[85]. Reducing the finger width of the BSF contact, on the other hand, can cause an increased series resistance loss along these fingers.
This explains the necessity of precise alignment. One single alignment step is optimal to keep the process steps to a minimum. The alignment procedure in this work is elaborated in Chapter 4.5.2. While photolithography and laser ablation yield high alignment precision, suitable for a small pitch size, only laser ablation can cost-efficiently be adapted for large-scale production.

2.5 Characteristic Quantities

2.5.1 J-V Curve

The current density-voltage (J-V) curve gives insight into several characteristic quantities of a solar cell. An exemplary illuminated and a dark J-V curve are plotted in Figure 2.10 with the resulting output power of the solar cell. The maximum of the output power is defined as the Maximum Power Point (MPP). Furthermore, the short-circuit current density J_{sc} (which is commonly defined as a positive value) and the open circuit voltage V_{oc} are characteristic quantities of a solar cell. A solar cell generates power for $0 < V < V_{\mathrm{oc}}$, while it is ideally operated at the MPP. The Fill Factor (FF) of a cell is defined as

$$FF = \frac{J_{\mathrm{mpp}}V_{\mathrm{mpp}}}{J_{\mathrm{sc}}V_{\mathrm{oc}}} \tag{2.9}$$

and can geometrically be identified with the fraction of the two striped rectangles in Figure 2.10.

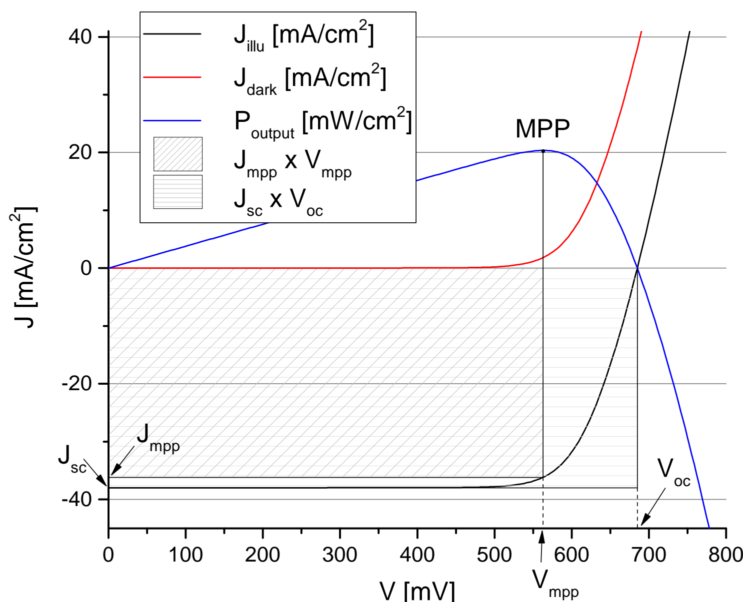

Figure 2.10: Exemplary illuminated and a dark J-V curves and the power output; Display of characteristic quantities (based on[85]).

An ideal solar cell yields a constant current $-J_{\text{sc}}$ when a reverse bias voltage is applied (without considering the reverse bias breakdown voltage). In a shunted solar cell on the other hand, an additional unwanted current path is present in the cell. The applied voltage, induces a parallel current across the shunt, which can be modeled by a shunt resistance R_{shunt}. The resulting current J_{total} can be calculated according to Kirchoff's current law and Ohm's law as

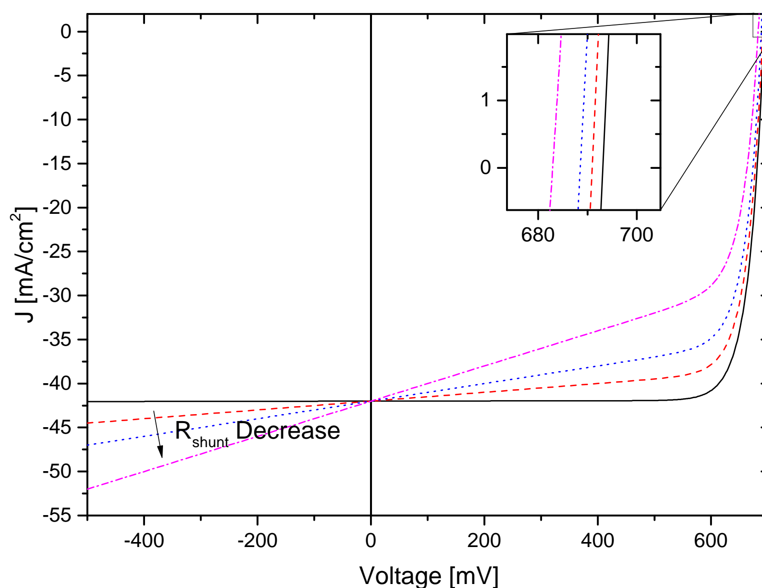

Figure 2.11: Impact of the shunt resistance on the J-V curve (based on[85]).

$$J_{\text{total}} = J - J_{\text{shunt}} = J - \frac{V + JR_{\text{series}}}{R_{\text{shunt}}} \tag{2.10}$$

where R_{series} is the series resistance of the cell. This parallel connected shunt resistance applies on forward bias likewise, thus reducing the FF as well as the V_{oc}, as apparent in Figure 2.11. Accordingly, R_{shunt} is the value defining the impact of a shunt on the cell performance. The lower the shunt resistance, the higher the current across the shunt, which decreases the cell's performance.

2.5.2 Free Energy Loss Analysis

A key quantity for a solar cell is the conversion efficiency η, which can be calculated by the Free Energy Loss Analysis (FELA)[106]. This approach is detailed in the following and applied in Chapter 3 to compare results achieved with two different simulation programs. The theory of analyzing free energy loss in solar cells was first published by Brendel et al.[106] in 2008.
Since electrical power is entropy-free, the produced electrical power by a solar cell can be considered as a rate of free energy[106]. The loss mechanisms detailed in Chapter 2.2 are accounted for in the FELA. Optical and thermalization loss are taken into consideration by a photogeneration rate of free energy density that solely considers photons that generate free charge carriers and only attributes them the energy between the quasi-Fermi energies ($\mathrm{E}_{\mathrm{F,n}}$ and $\mathrm{E}_{\mathrm{F,p}}$)[106]

$$\phi_g = \frac{1}{A} \int_{\tilde{V}} G \left(\mathrm{E}_{\mathrm{F,n}} - \mathrm{E}_{\mathrm{F,p}}\right) \mathrm{d}\tilde{V} \tag{2.11}$$

where A is the area of the solar cell, $\tilde{V}$ is the volume and G the generation rate.
The electrical loss is described by two loss channels, the resistive loss due to charge carrier transport and the charge carrier recombination. The free energy density dissipation rate by transporting charge carriers[106]

$$\phi_{\mathrm{t,e/h}} = \frac{1}{A} \int_{\tilde{V}} \left|\vec{J}_{\mathrm{Q,e/h}}\right|^2 / \sigma_{\mathrm{e/h}} \mathrm{d}\tilde{V} \tag{2.12}$$

accounts for loss resulting from charge carrier drift and diffusion. While a drift current induces resistive heating, diffusion of charge carriers dissipates free energy due to the increase of the charge carrier's entropy by diffusing from a region of high to a region of lower charge carrier concentration (see Chapter 2.1.3), thus reducing the entropy-free part of their total energy[106]. Recombination loss is weighted with the local quasi-Fermi splitting. This transforms global current loss into local loss rates of free energy, which conveniently results in the same units as the resistive loss and the power output of the cell. All charge carrier recombination loss detailed in Chapter 2.2.1, is included for the bulk in[106]

$$\phi_{r,b} = \frac{1}{A} \int_{\tilde{V}} R \left(\mathrm{E}_{\mathrm{F,n}} - \mathrm{E}_{\mathrm{F,p}}\right) \mathrm{d}\tilde{V} \tag{2.13}$$

and for the surface in[106]

$$\phi_{r,s} = \frac{1}{A} \int_{\tilde{V}} R_{\mathrm{surf}} \left(\mathrm{E}_{\mathrm{F,n}} - \mathrm{E}_{\mathrm{F,p}}\right) \mathrm{d}\tilde{V} \tag{2.14}$$

The produced electrical power is calculated by subtracting all free energy dissipation from the photo-generation rate, such as

$$J_Q V_Q = \phi_g - \phi_{\mathrm{t,e}} - \phi_{\mathrm{t,h}} - \phi_{r,b} - \phi_{r,s} \tag{2.15}$$

where J_Q and V_Q are the terminal charge current density and voltage, respectively.
The conversion efficiency η is defined as the maximal output power of the solar cell weighted with the total incident illumination power density of an AM1.5 spectrum of the sun $\phi_{\text{AM1.5}}$

$$\eta = \frac{J_{\text{mpp}} V_{\text{mpp}}}{\phi_{\text{AM1.5}}} = \frac{FF \cdot J_{\text{sc}} V_{\text{oc}}}{\phi_{\text{AM1.5}}} = \frac{\phi_g - \phi_{\text{t,e}} - \phi_{\text{t,h}} - \phi_{r,b} - \phi_{r,s}}{\phi_{\text{AM1.5}}} \tag{2.16}$$

The spectrum of solar irradiation reaching the earth's atmosphere (AM0) corresponds to that of a 5760 K black body. Hence the radiation hitting the earth's surface when the sun is at a 42° angle of elevation is further attenuated and filtered around the absorption spectra of atoms and molecules contained in the atmosphere (AM1.5), as can be seen in Figure 2.12.

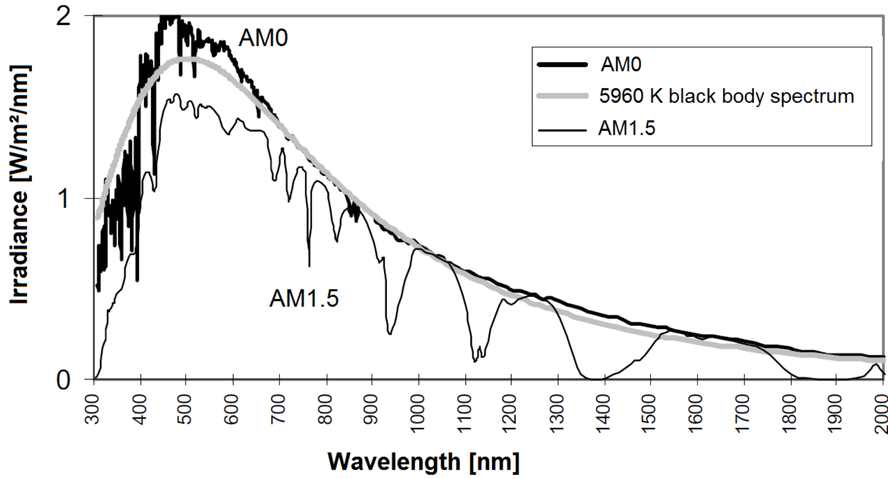

Figure 2.12: Solar spectrum outside (AM0) and inside (AM1.5) the Earth's atmosphere and the 5760 K black body spectrum (based on[14]).

A semi empirical limiting curve of the efficiency as function of the energy gap was introduced by Shockley and Queisser in 1961[107]. The so called detailed balance limit, or Shockley-Queisser limit, that takes only radiative recombination into account, reveals a 30% efficiency limit for single junction c-Si solar cells under AM1.5 irradiation. A more recent publication from A. Richter et al. applies a new internationally accepted solar spectrum and band gap narrowing, as well as the Auger recombination as dominant intrinsic loss mechanism, and hence reduces the theoretical limit to 29.43%[108]. In conclusion, the homo junction BC-BJ solar cell designed by Franklin et al. at the Australian National University[11], attaining a power conversion efficiency of 24.4%, has reached approximately 83% of the theoretical conversion efficiency limit.

3 Simulation

Simulations of solar cells are generally used to model the transport and recombination of charge carriers. This insight can help to improve and understand solar cells. In this work, simulations are used to investigate the recombination mechanisms at the junction of highly p- and n-doped regions (see Chapter 3.3). Furthermore, various simulations are performed in Chapter 4 to gain information about the impact that certain parameter changes have on the resulting cell performance.
Elaborate simulations usually require a large amount of computer memory because numerically demanding modeling is performed. Next to complexity in simulation setup, another drawback is the availability of simulation programs such as Sentaurus Synopsys[109] (in the following called Sentaurus). The author has therefore aimed at the use of the fast and freely available 3-D simulation tool Quokka[110],[111].
Several publications such as[111]–[113] have shown the compatibility of Quokka's simulation results with other simulation programs such as Sentaurus, and have compared experimental results to simulated results from Quokka. To the knowledge of the author, no profound comparison of the FELA analysis of the simulation program Quokka with another simulation program has been published yet. A comparison of FELA results obtained with Quokka and Sentaurus is performed in the following of this work exemplarily on an IBC solar cell. The comparison's validation is employed to carry out further simulations with Quokka in in the experimental part of this work.
Due to the multitude of theoretical components contributing to the calculations of the simulation, the theoretical background given in this work is restricted to the parts which are relevant for the discussion in this chapter and for the analysis of the experimental part.

3.1 Quokka

The solar cell simulation program of choice in this work is Quokka. Quokka is implemented in MATLAB and employs two simplifications in comparison with Sentaurus, namely the quasi-neutrality condition and conductive boundaries, to reduce the computational effort of simulations.
The quasi-neutrality condition describes the equality of excess carrier densities and is applied in Quokka outside of the SCR. This assumption was first investigated by Kleinman in 1956[114]. In the model for charge carrier transport presented in[115] three coupled differential equations have to be simultaneously solved in the cell's bulk, the two quasi-Fermi potentials $\varphi_{\mathrm{F,n}}$ and $\varphi_{\mathrm{F,p}}$, and the electrostatic potential φ. The carrier concentrations and the current densities can be derived from these three potentials. By introducing the quasi-neutrality condition outside of the SCR, the model of charge carrier transport is reduced from a set of three coupled differential equations to a set of two coupled differential equations[111], and, hence, needs to be solved for the two quasi-Fermi potentials only.
Quokka is based on the Conductive Boundary (CoBo) model, which was introduced by Brendel in 2012[115]. The diffused layers are modeled as conductive boundaries, which are infinitely thin layers with no spatial resolution of the junction. The continuity equation in the diffused layers has therefore one space dimension less than the cell volume. This approach is legitimate because the resolution of the dopant-diffused layers as well as the recombination within the depletion

region are not essential for the cell's output power[115]. Already in 1984, Alamo and Swanson published their computer simulation results, showing that charge carrier diffusion in shallow emitters could be treated as a recombinative boundary condition[116]. The recombination parameter of the junction J_0 and its sheet resistance R_{sheet} are therefore the key quantities that define the boundaries' physics, such as the current flow in the diffused surfaces.
While these simplifications are very useful to accelerate and facilitate the simulation process, there are limitations to the CoBo model. Since it neglects the effects that take place in the space-charge region, it fails whenever the physics in the space-charge region is the main effect. The recombination in that area can become dominant for a low bulk SRH lifetime for example. Likewise, and more significant for this work, no overlap between highly doped regions can be resolved and no tunneling recombination between highly doped regions can be accounted for.
Although Quokka is a very accessible simulation program, it is also a complex tool which can fail to produce correct results if the input arguments do not correspond to a possible physical condition. As explained above, there are also limits to the solvable conditions. Especially for low performing solar cell structures and extreme conditions, the result might not converge. This is why in this work every simulation result was checked to have a FELA balance $\varepsilon_{\text{FELA}}$ (see equation 3.1) below 1%, which is an indication of the overall quality of convergence. The FELA balance mathematically compares the sum of the FELA contributions (Chapter 2.5) subtracted from the generated power with the output power, weighted with the maximum of the generated power and the output power:

$$\varepsilon_{\text{FELA}} = \frac{\phi_g - \phi_{\text{t,e}} - \phi_{\text{t,h}} - \phi_{r,b} - \phi_{r,s} - J_Q V_Q}{max\left(\phi_g, J_Q V_Q\right)} \tag{3.1}$$

In addition, all presented simulations were double checked with the finest standard mesh, to prove mesh independence[110]. The finite volume method is applied for the discretization of the model equations in Quokka[111] (as it is done in Sentaurus[115]). A non-equidistant orthogonal conformal mesh is employed on a cuboidal solution domain, which leads to a low total number of elements. The element sizes are adapted to the local features of the cell and typical settings are predefined for coarse, medium and fine standard meshing. The predefined settings can be altered by the user.

3.2 Comparison Quokka and Sentaurus

In this section, a comparison between IBC solar cell simulation results achieved with Quokka and Sentaurus is made. For this comparison not only the characteristic quantities, namely J_{sc}, FF, V_{oc} and η, are considered but also all results obtained by FELA. Matching results in this comparison are used as evidence in this work, that Quokka simulation is adequate for the simulation of this solar cell concept. The base for this conclusion is formed by the assumption that Sentaurus simulations provide accurate results.
With the knowledge of Chapter 2.5 about the characteristic quantities and the general composition of the FELA, alone the FELA is left to be broken down in the following. As discussed in Chapter 2.5, the FELA calculates the free energy density dissipation rate due to charge carrier transport $\phi_{\text{t,e/h}}$ and the recombination loss $\phi_{\text{r,b/s}}$. These dissipation rates are calculated by the simulation program for the different regions of the solar cell, namely bulk (base), emitter, BSF and FSF, at the MPP. Accordingly, the FELA describes the loss due to transport and recombination in the different regions of the solar cell evaluated at the MPP. In addition, external series and shunt resistance loss can be calculated by the simulation programs, they are omitted in these Quokka simulations, by inserting a low series resistance and a high shunt resistance.

Input Parameters

The parameters that are input into both simulation programs are listed in Table 3.1. In addition, the generation profile described in Chapter 2.1.2 and a path-length profile are inserted into the simulation programs. In both simulation programs, an intrinsic non-recombinative gap region with a thickness of about 2 μm, separating the highly p- and n-doped regions on the rear of the solar cell, is introduced. It is to be reminded, that further input parameters are necessary for the simulation with Sentaurus (e.g. the doping profiles).
Next to the fixed parameters, the cell width and the emitter to BSF fraction are varied on a

Table 3.1: Input parameters for the simulation of an IBC solar cell.

Parameter	Value	Units
Cell thickness	180	μm
Contact width	80	μm
Bulk material	n-type	
τ_{eff}	10	ms
Base resistivity	3.86	Ωcm
Total generation current	43.9	mA/cm^2
$R_{\text{sheet,emi}}$	63	$\Omega/\square$
$R_{\text{sheet,BSF}}$	53	$\Omega/\square$
$R_{\text{sheet,FSF}}$	130	$\Omega/\square$
$R_{\text{c,p}}$	0.71	mΩcm^2
$R_{\text{c,n}}$	0.52	mΩcm^2

certain interval. This is done to check the accuracy of the simulations in different situations. While for a large emitter fraction (f_{emi}), minority charge carriers are more likely to reach the emitter without recombination in the bulk due to a large emitter coverage of the rear side, this probability is reduced for a small f_{emi}.

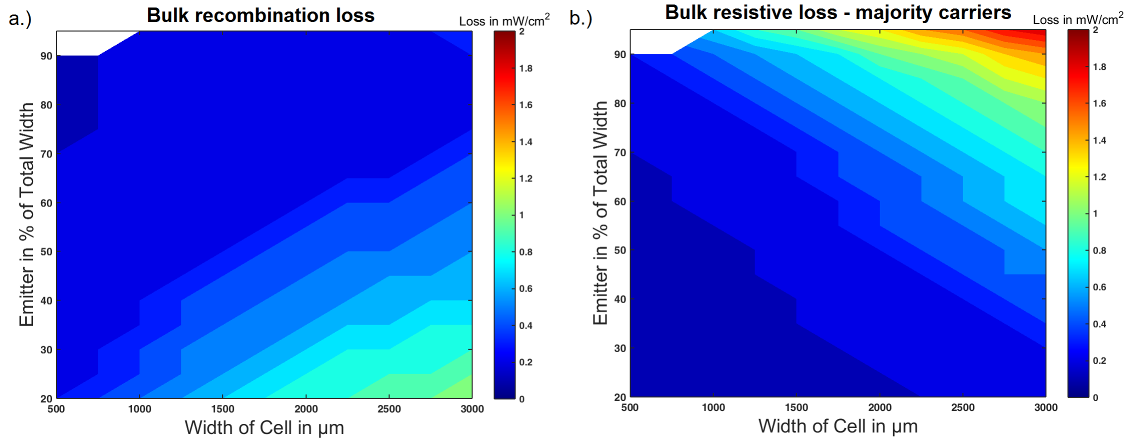

Figure 3.1: FELA obtained from Quokka simulation of the a.) bulk recombination loss, and b.) bulk resistive loss of majority charge carriers.

This can be seen in Figure 3.1a, where the recombination in the bulk is displayed as a function of the emitter fraction and the cell width. The recombination loss is a result from the FELA of Quokka simulation. The recombination in the bulk is primarily attributed to the lack of extraction of the minority charge carriers from the bulk and increases for a decreasing emitter

fraction. On the other hand, the reduction of f_{emi} decreases the resistive loss of the majority charge carriers in the bulk (see Figure 3.1b), because the majority charge carriers have to be transported for a shorter distance in the bulk before they can drift into the BSF. This exemplarily illustrates that different transport and recombination mechanisms are relevant in varying situations. Altering the cell width furthermore changes the loss mechanisms in the cell and gives more insight into the loss mechanism differences in the simulations. Figure 3.1 demonstrates well, that the explained effects become more significant for an increased cell width as the charge carriers are required to travel further distances.
For the discussion of this chapter, two parameter intervals can be distinguished. The high efficiency area, which is correlated to the red color ($\eta > 20\%$), see Figure 3.2, and the area of low efficiency (blue). Since in photovoltaic high cell efficiency is desired, the region of high efficiency is of interest. A high correlation between the simulation results is therefore aimed at in the high efficiency sector, while larger disparity is accepted in the area of low performance.

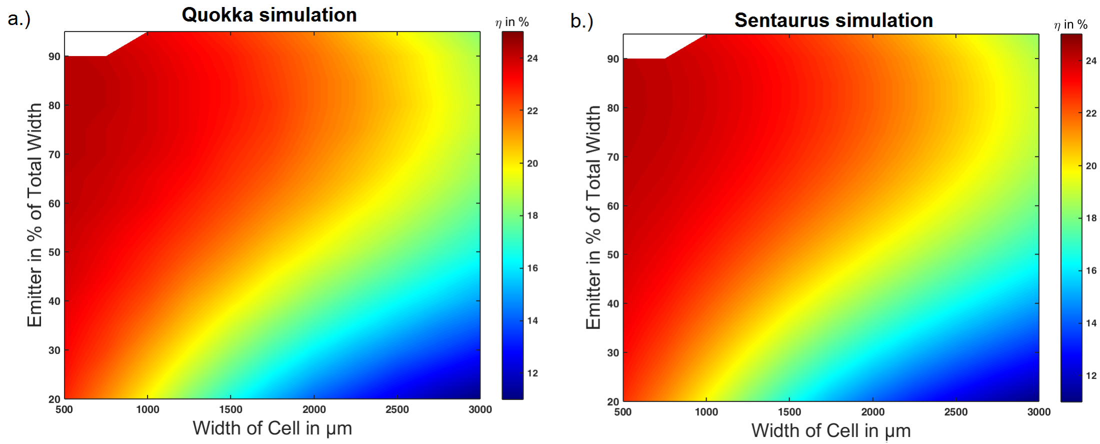

Figure 3.2: Simulation result of the power conversion efficiency obtained with a.) Quokka, and b.) Sentaurus Synopsys.

One parameter, that is differently input into Quokka and Sentaurus, concerns recombination. The recombination parameter J_0, which corresponds to an experimentally accessible measure unit, can be directly inserted into the Quokka simulation program. In Sentaurus, on the other hand, the recombination is defined by the surface recombination velocity S. The recombination parameter J_0 can be extracted from the Sentaurus simulation results to bring the Quokka recombination parameter input into line with that of Sentaurus. For this purpose, the 'one-diode model' is used, which is an approximation of an ideal solar cell[16]

$$J_Q = J_0 \left[\mathrm{e}^{\frac{V_Q}{V_{th}}} - 1 \right] + J_{\mathrm{sc}} \tag{3.2}$$

where V_{th} is the thermal voltage. The recombination parameter is calculated in V_{oc} condition under consideration of the various recombination paths in the different regions of the solar cell. Each loss current i (surface, Auger- and SRH-recombination) is subtracted under J_{sc} and V_{oc} conditions and summed up for the respective region (emitter, BSF, FSF) to calculate the J_0 value in each region according to (results from equation 3.2)

$$J_0 = \left[\sum_i \left(J_{i,V_{\mathrm{oc}}} - J_{i,J_{\mathrm{sc}}} \right) \right] \cdot \left(\mathrm{e}^{\frac{V_{\mathrm{oc}}}{V_{th}}} - 1 \right)^{-1} \tag{3.3}$$

This approach is not applicable in the entire parameter interval, however. This becomes apparent, when plotting the acquired J_0 values as a function of the emitter fraction and the cell's

width (see Figure 3.3). The J_0 value is chosen to correspond to a value in the area of high power conversion efficiency for each region, the values are depicted in Table 3.2.
The variation of the extracted J_0 value to the chosen J_0 on the entire parameter interval is

Table 3.2: J_0 input parameters for the simulation of the IBC solar cell; The J_0-values are used for the simulation with Quokka, while the S-Values are used for the simulation with Sentaurus Synopsis.

Parameter	Value	Units
$J_{0,\text{emi}}$	127	fA/cm^2
$J_{0,\text{c,emi}}$	580	fA/cm^2
$J_{0,\text{BSF}}$	107	fA/cm^2
$J_{0,\text{c,BSF}}$	340	fA/cm^2
$J_{0,\text{FSF}}$	25	fA/cm^2
S_{emi}	$10{\cdot}10^3$	cm/s
$S_{\text{c,p}}$	$2{\cdot}10^7$	cm/s
S_{BSF}	$32{\cdot}10^3$	cm/s
$S_{\text{c,n}}$	$2{\cdot}10^7$	cm/s
S_{FSF}	$1{\cdot}10^3$	cm/s

$\pm 9\%_{\text{rel}}$ and $\pm 4\%_{\text{rel}}$ for $J_{0,\text{emi}}$ and $J_{0,\text{c,emi}}$, respectively. The relative variation of the other J_0 values is much higher (see Figure 3.3).

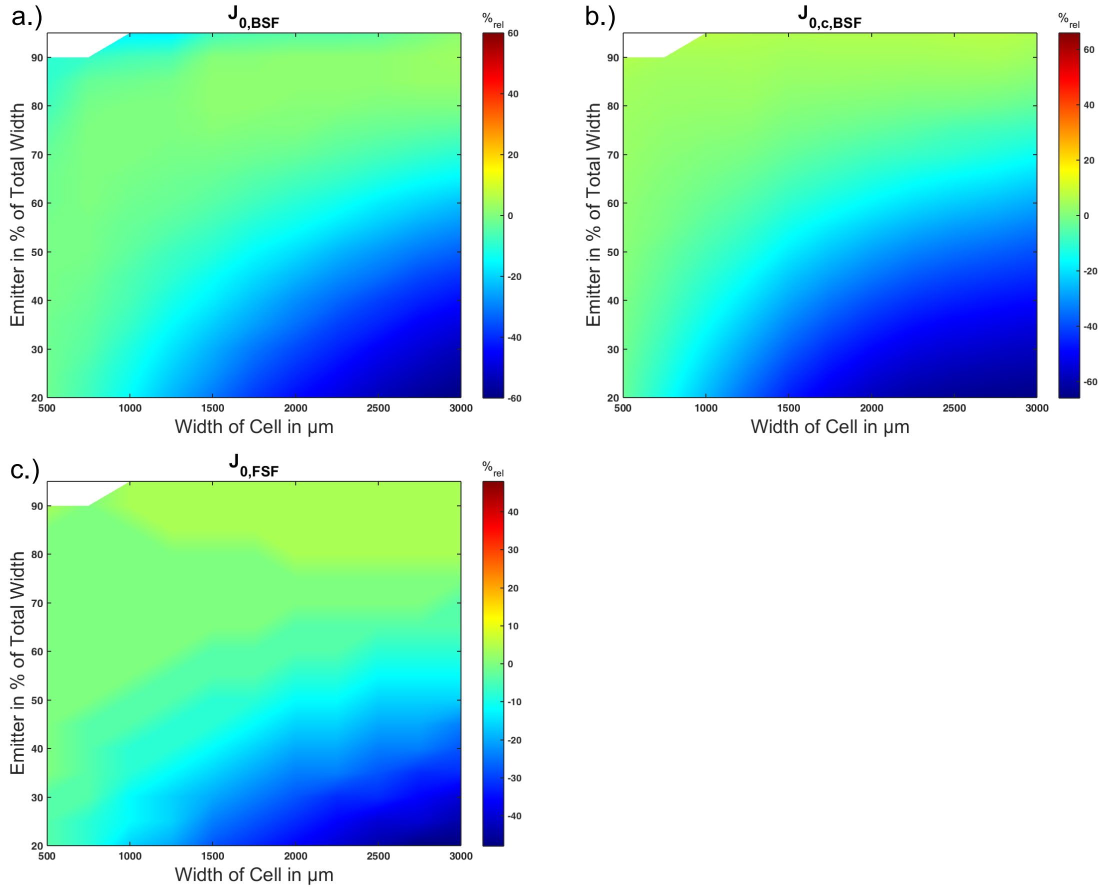

Figure 3.3: J_0 values extracted from Sentaurus Synopsis simulation according to equation 3.3 in a.) the BSF region, b.) the contacted BSF region and c.) the FSF region.

As can be seen in Figure 3.3, the J_0 values extracted from the Sentaurus simulation for the BSF and FSF correspond well in the area of high efficiency. This is due to the fact, that the J_0 values are chosen to fit one of the extracted values in this region and that the variation is not very high in that area. Much lower recombination parameters are yielded for J_0 values in the sector of low performance. This is probably related to the fact, that equation 3.3 cannot be applied to a cell with low performance, thus leading to a high inaccuracy in this area.

Comparison of the Characteristic J-V Quantities

The main focus of this section consists in comparing the characteristic quantities of the J-V curve resulting from Quokka and Sentaurus simulations for the IBC solar cell. A detailed analysis of the physical processes limiting the solar cell conversion efficiency is given in the dissertation of Daniel Sommer[80]. In that dissertation, the characteristic quantities are used to explain efficiency's behavior, and the limits of the characteristic quantities are attributed to different effects in the solar cell.
Comparison of the results obtained with Quokka and Sentaurus is done by subtracting the mapped simulation results. As an example, serve Figure 3.2 and Figure 3.4a, that display the conversion efficiency's dependence on f_{emi} and the cell's width. The results obtained with Quokka (Figure 3.2a) and Sentaurus (Figure 3.2b) are difficult to distinguish because they follow the same pattern. This is why Sentaurus simulation results are subtracted from the Quokka simulation results and standardized to the Quokka simulation results in Figure 3.4a, according to

$$\frac{\Delta\eta}{\eta_{\text{Quokka}}} = \frac{\eta_{\text{Quokka}} - \eta_{\text{Sentaurus}}}{\eta_{\text{Quokka}}} \tag{3.4}$$

The color gradient serves as a visual indicator of how well the two simulation results stack. A color between green and red (see color bar) corresponds to a higher value obtained by the Quokka simulation, while for a color between green and blue the Sentaurus simulation yields a higher value. The color map of $\Delta\eta/\eta_{\text{Quokka}}$ shows a gradient from a small emitter fraction and cell width to a large emitter fraction and cell width.
Not all cell concepts that are theoretically possible can be realized in production. In the BC-BJ solar cell concept, major difficulties are the alignment of the doped areas and the metal grid (see Chapter 2.4.2), as well as large R_{series} when adopting a thin metal grid. Accordingly, the geometrical cell parameters have to be large enough to be viable in production. The most relevant sector owing to the high efficiency and feasibility in production therefore lies within $70\% < f_{\text{emi}} < 90\%$ with a cell width of 1000-1500 μm, which is located in the area of high efficiency (correlated to the red color, $\eta > 20\%$, in Figure 3.2). This sector is called 'relevant sector/area' in the following. The conversion efficiency in the sector of high performance is approximately 23% with the chosen input parameters. The subtraction map in Figure 3.4a shows, that the absolute value of the relative difference in the relevant area has a maximum of about $0.2\%_{\text{rel}}$. This difference increases for a large emitter fraction and large cell width to a maximum of around $0.8\%_{\text{rel}}$ and for a small emitter in combination with a small cell width to $0.5\%_{\text{rel}}$.
The color spectrum of the subtraction maps for η, FF, J_{sc} and V_{oc} in figure 3.4 is normalized, a certain color does therefore correspond to a specific relative difference. The conversion efficiency is a quantity, that comprises the FF, J_{sc} and V_{oc} according to equation 2.16. These quantities are therefore of relevance to establish where the differences between the simulation results in η originate from. Since all three quantities are linked to the conversion efficiency by multiplication, the relative differences of FF, J_{sc} and V_{oc} are added to amount the relative difference of the

conversion efficiency (deduced from the total differential)

$$\frac{\Delta\eta}{\eta} \approx \frac{\Delta \mathrm{FF}}{\mathrm{FF}} + \frac{\Delta J_{\mathrm{sc}}}{J_{\mathrm{sc}}} + \frac{\Delta V_{\mathrm{oc}}}{V_{\mathrm{oc}}} \tag{3.5}$$

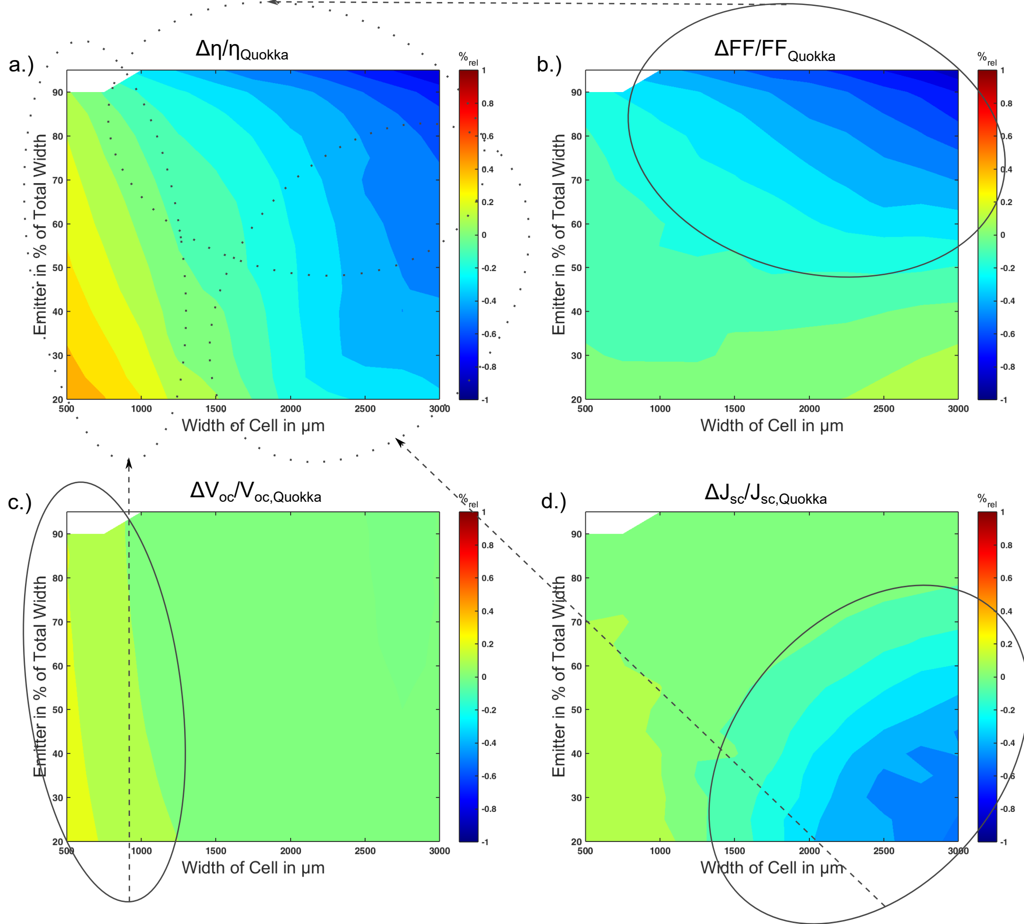

Figure 3.4: Subtraction of the simulation results obtained with Sentaurus from those of Quokka, normalized to the Quokka results for a.) η, b.) FF, c.) V_{oc}, and d.) J_{sc}.

As a result, the normalized subtraction maps in Figure 3.4 for FF, J_{sc} and V_{oc} can be visually added to amount in the normalized subtraction map of η (as indicated in Figure 3.4). Accordingly, the characteristic behavior of $\Delta\eta/\eta_{\mathrm{Quokka}}$ can be attributed to features in the other subtraction maps. The characteristic blue area in $\Delta\eta/\eta_{\mathrm{Quokka}}$ for large f_{emi} and W_{cell} can be put down to $\Delta FF/FF_{\mathrm{Quokka}}$ and the area of small f_{emi} and large W_{cell} to $\Delta J_{\mathrm{sc}}/J_{\mathrm{sc,Quokka}}$. The higher J_{sc} value yielded by the simulation in Sentaurus, is possibly related to the discrepancy of the recombination parameters in this parameter interval, displayed in Figure 3.3. The higher efficiency in the simulation with Quokka for small W_{cell}, on the other hand, mainly results from $\Delta V_{\mathrm{oc}}/V_{\mathrm{oc,Quokka}}$. The overall comparison of the simulation results therefore appears to be consistent. The characteristic behavior mostly inflicts on the verge of the variation interval, thus corresponding to 'extreme' simulation conditions (small/large cell width/f_{emi}), while only a limited effect is observed in the relevant section which results from an effect on the FF.
Considering the relevant area only, the maximum relative difference of η is found to be $(\Delta\eta/\eta)_{\mathrm{max}} = 0.2\%$ (see earlier). If the Sentaurus simulation is considered to yield an 'ideal' simulation result, the minimum efficiency resolution of the Quokka simulation in the relevant area corresponds to this relative difference. For an efficiency of 20% in this area, the error corresponds

Table 3.3: Quokka simulation minimum resolution of the characteristic quantities in the relevant area for the presented IBC solar cell.

Quantity	Minimum resolution
η	$0.04\%_{\text{abs}}$
J_{sc}	$0.04\ \text{mA/cm}^2$
FF	$0.3\%_{\text{abs}}$
V_{oc}	$0.6\ \text{mV}$

to $\delta_{\eta,\text{Quokka}} = 0.04\%_{\text{abs}}$, which is a negligible value for an error in the efficiency of high performance solar cells. Accordingly, the resolution of the Quokka simulation in the relevant area for the characteristic quantities is calculated and displayed in Table 3.3.
No conclusion from the FELA can be derived for the characteristic quantities since the FELA describes the loss mechanisms at the MPP only. However, the FELA gives a much closer insight into the differences in the simulations conducted with Quokka and Sentaurus. This is why a comparison of the FELA is conducted in the next section.

Comparison of the Loss Channels

The FELA breaks the loss in a solar cell down to the resistive and recombination loss channels in the different regions of the cell, namely FSF, BSF, bulk and emitter. In the following, a comparison of the results obtained with Quokka and Sentaurus is conducted. Subtraction maps are generated that cover the same f_{emi} and W_{cell} intervals than in the last section. These subtraction maps are not normed, because only loss channels that actually have an influence on the solar cell efficiency are to be considered, hence a comparison of the absolute values is required. Furthermore, all loss channels are declared in the units mW/cm^2 and are thus comparable.
To begin with, the generated power is investigated. The generated power is an important value

Table 3.4: FELA results obtained from Quokka and Sentaurus Simulation broken down for each loss channel; Δ_{max} is the maximum value resulting from the subtraction of the Quokka simulation result and that of Sentaurus simulation on the entire parameter variation interval.

Loss channel	Δ_{max} [mW/cm^2]
Resistive FSF	0.03
Resistive majorities bulk	0.06
Resistive minorities bulk	0.07
Recombination bulk	0.08
Resistive emitter	0.10
Resistive BSF	0.15
Recombination FSF	0.17
Resistive emitter contact	0.19
Recombination emitter	0.30
Recombination BSF	0.65
Resistive BSF contact	0.71

for comparison, because a different power loss is expected in the different loss channels, if the generated power in the cell does not match in the simulations. The generated power mainly depends on the illumination of the cell and the applied generation profile. Since the same input

is used in both simulation programs, a very similar result for the generated power is expected. This is indeed the case, since the generated power varies between the simulations over the entire simulation map by less than $0.2\%_{\mathrm{rel}}$ with no apparent trend in the values, featuring values between 26.6 and 29 mW/cm^2.
A high correlation is yielded by the FELA results of the simulations conducted with Quokka and Sentaurus on the parameter interval. The results are presented in Table 3.4. Not all loss plots detailing the different loss mechanisms in the solar cell are discussed, but only those where the difference between the Quokka and Sentaurus simulation noticeably exceeds 1% of the generated power. This is the case for the recombination loss in the BSF and the resistance loss at the BSF contact.
The recombination loss in the BSF obtained from simulations with Quokka and Sentaurus follows the same behavior in the mapped parameter interval. This is not an evident result because of the J_0 values' uncertainty for the BSF, especially in the area of low efficiency (displayed in Figure 3.3). The subtraction map reveals a low correspondence for a small emitter fraction, thus in the area of low efficiency. For the relevant area, the values correspond with an error of < 0.2 mW/cm^2.

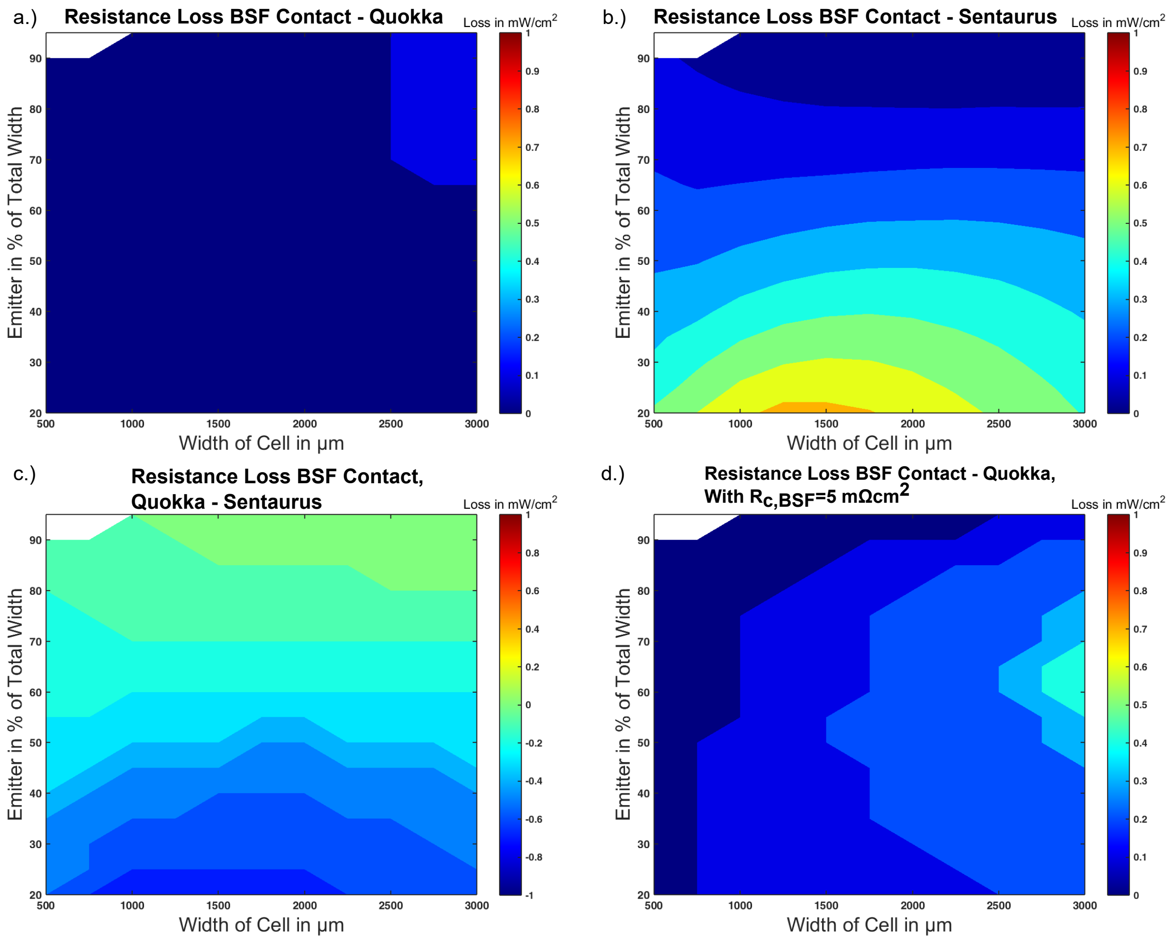

Figure 3.5: FELA simulation result obtained with Quokka and Sentaurus Synopsis for the BSF contact resistance loss, a.) Quokka simulation result, b.) Sentaurus Synopsis result, c.) subtracted result Quokka-Sentaurus Synopsis, d.) Quokka simulation with increased contact resistance loss.

The simulation results of the resistance loss at the BSF contact present a different picture. While no noticeable BSF contact resistance loss is observed in the Quokka simulation (see Figure 3.5a),

a considerable resistance loss at the BSF contact is obtained in the Sentaurus simulation for a small emitter fraction (see Figure 3.5b). The BSF resistance loss behavior is the only loss channel that appears to show a different behavior on the variation interval for Quokka and Sentaurus simulation. This difference has above all an impact for a small emitter fraction, thus not inflicting much in the high efficiency area (see Figure 3.5c). Another Quokka simulation is performed with an increased $R_{\mathrm{c,n}} = 5\,\mathrm{m\Omega cm^2}$ (original value: $R_{\mathrm{c,n}} = 0.52\,\mathrm{m\Omega cm^2}$) to investigate, whether the increased contact resistance leads to a similar behavior on the parameter interval. As visualized in Figure 3.5d, an increased BSF contact resistance mainly impacts on the BSF resistance loss for a large cell width according to the Quokka simulation result. In conclusion, the difference between the FELA simulation result for the BSF resistive loss obtained with Quokka and Sentaurus is not related to a differently assumed $R_{\mathrm{c,n}}$. As a consequence, Sentaurus must implement an additional loss effect at the BSF contact which the Quokka simulation does not account for.

Conclusion

In this chapter, a high correlation between the Quokka and Sentaurus simulation results is observed in the relevant area of high efficiency. The correlation is investigated for the characteristic J-V quantities as well as with consideration of the FELA. The FELA shows a discrepancy between the simulation results for the BSF resistance loss. In general the correspondence is much higher for more efficient solar cells that are not at the edge of the simulation interval.

3.3 Simulation of the pn-Junction

In this chapter, the influence of an intrinsic gap region between the highly n- and p-doped regions of a BC-BJ solar cell on the J-V curve's characteristic quantities is investigated by simulation. As mentioned earlier, the simulation program Quokka considers the doped regions as a 2 dimensional surface with no depth into the Si material. Therefore, Quokka is not fit for the simulation of the pn-junction on the rear of a BC-BJ solar cell, as will become apparent in the following. Accordingly, Sentaurus is used for theses simulations.
For this investigation, two simulation situations are observed: One with an intrinsic gap between the two highly doped regions (fig. 3.6a), and another one, where the two doping profiles fully overlap (fig. 3.6b), which is a probable situation due to lateral dopant diffusion. The recombination mechanisms that could occur in this physical constellation with adjacent highly doped regions are explained in Chapter 2.2.3 and the dependence of the charge carrier lifetime on SRH recombination, τ_{SRH}, is detailed in equation 2.8. By defining a trap density profile, that can be determined experimentally in certain situations[45], τ_{SRH} solely depends on the capture cross section σ and in this specific case on the overlap of the two highly doped regions.

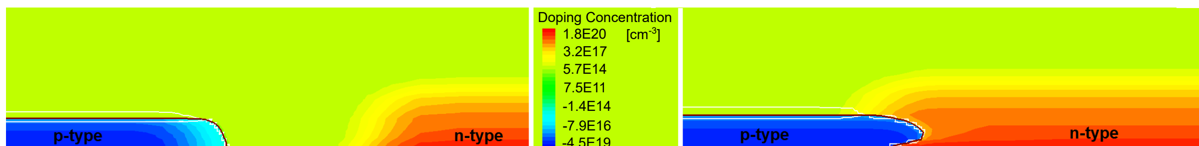

Figure 3.6: Cross section generated with Sentaurus Synopsys of the pn-junction with a.) an intrisic gap, and b.) an overlap of the highly doped regions; The p-type emitter is colored in blue, while the n-type BSF is colored in red to yellow, depending on the doping concentration; (not to scale, based on[80]).

Current Knowledge Base

This kind of simulation is investigated in detail in the dissertation of Sommer[80]. The results obtained by Sommer are mentioned in the following while the adapted simulation results achieved in this work are discussed in the next section. The simulation results in[80] show that a low charge carrier capture cross section σ ($\sim 10^{-25}$ cm^2) does not influence the cell efficiency, even for a large overlap of the highly doped regions. This changes for higher values of σ ($> 7.5 \cdot 10^{-18}$ cm^2). For a higher capture cross section, the SRH recombination decreases the cell efficiency in general and significantly reduces the cell efficiency for an overlap due to the increased trap capture cross section. More details about the influence on the J_{sc}, V_{oc} and FF and the resulting η are given in[80]. As a result, the simulations performed by Sommer reveal, that no intrinsic gap is required between the highly p- and n-doped regions on the rear side of an IBC solar cell, as long as those regions are defect-free (cross-section of $\sigma \sim 10^{-25}$ cm^2).
These simulation results also apply to the investigation in this work. Simulations in this work are run with the same defect profile (appropriate because of the similar P doping profile) and the simplification of placing the energetic level of the trap states in the center of the band gap. Nevertheless, different doping profiles can alter the effects taking place, which is why the doping profiles are adapted to experimentally measured profiles. Sommer experimentally observed that tunneling recombination was no dominant recombination effect for his samples. This could be different in the experimental part of this work, which is why tunneling recombination ought to be taken into consideration for the experimental analysis of this effect.

Simulation Results

The input parameters from Table 3.1 are used in these simulations. Additionally, the capture cross section is chosen to be $\sigma = 10^{-17}$ cm^2 and only local recombination mechanisms are considered (no tunneling recombination). Furthermore, one single pn-junction on a 50x50 mm^2 Si wafer is simulated. The pn-junction is illuminated on a width of 1000 μm with a ratio of 1/1 for the emitter/BSF coverage on the back of the illuminated section. These parameters are chosen according to the experimental viability conditions.

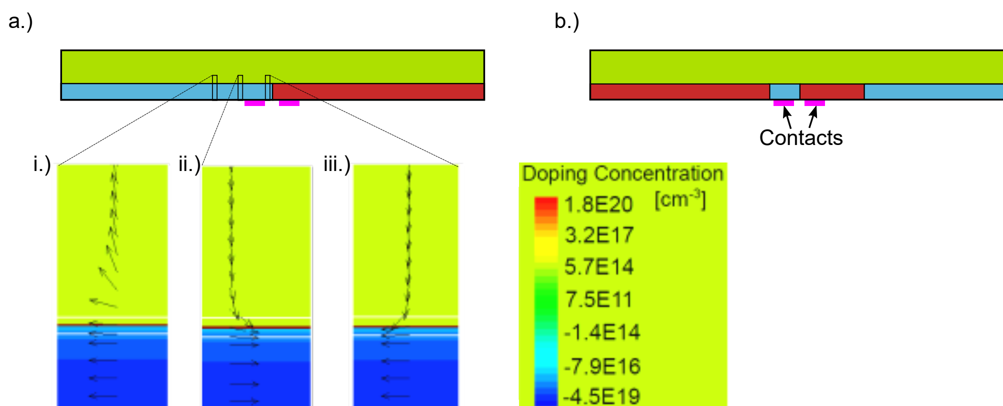

Figure 3.7: Schematic cross section of the sample with pn-junction with a.) half-half structure, b.) zebra-structure; Base doping: green, emitter: blue, BSF: red; Sentaurus Synopsis simulation results: hole current flows away from the contact i.) in regions of the emitter that are further away from the contact and hole current flow towards the contact, which is located in ii.) right of the enlargement, and in iii.) left of the enlargement; (not to scale).

The two situations introduced earlier (see Figure 3.6) are simulated and subtracted from one another in Table 3.5. These simulations are performed for a 'half-half structure' (see Figure 3.7a),

where the emitter and BSF each cover half of the rear surface of the entire wafer. Furthermore, the simulations were also executed for a 'zebra structure' (see Figure 3.7b), that consists of a striped structure on the rear side with alternating p- and n-doped regions.
The difference in characteristic quantities obtained with and without a gap is to be as high as possible to experimentally distinguish samples with and without an intrinsic gap region between the emitter and the BSF. This can help to determine, to what extent the intrinsic gap region inflicts on the cell performance. The results in Table 3.5 show, that the saturation current density does not change with regard to the gap for both structures. The V_{oc} yields a 9 mV higher voltage for the simulation with a gap region for both sample structures. The results display that the zebra structure generally provides higher V_{oc} and higher FF values than the half-half structure. Due to the increased FF in the zebra structure, the difference between the samples with and without a gap increases from 1.5% to 1.9%. This gain of approximately 27%$_{rel}$ is useful in the experimental evaluation, which is why the zebra structure is applied in the experimental part of this work. It is to be mentioned, that even larger differences are achieved between the simulation results with and without gap, when tunneling recombination is considered in the simulations. The given values are therefore modest estimations.
The gain in FF for the zebra structure results from the shortened emitter width. The junctions

Table 3.5: Simulation results achieved with Sentaurus Synopsys of one pn-junction illuminated on a width of 1000 μm with and without an intrinsic gap for the half-half structure and the zebra structure.

	half-half			zebra Structure		
	Gap	Overlap	Δ	Gap	Overlap	Δ
J_{sc} [mA/cm^2]	35.7	35.7	0	35.7	35.7	0
V_{oc} [mV]	633	624	9	636	627	9
FF [%]	77.9	76.4	1.5	80.8	78.9	1.9
η [%]	17.6	17.0	0.6	18.4	17.7	0.7

in the cell typically lead to a hole current flow from the base into the emitter and through the emitter to the contact. If the emitter is much wider than the metal contact, holes that diffuse through the emitter in some distance to the contact, don't perceive the drift current towards the contact. For a wider emitter (e.g. 25 mm for the half-half structure), the holes can diffuse far into the shaded area of the wafer and recombine there without ever reaching the contact. This effect can be seen by the hole current density vectors in Figure 3.7. While the hole current in (ii) and (iii) flows into the emitter (blue) towards the contact that is located in between the two enlarged sectors, the current in (i), which is located in some distance from the contact, flows away from the contact and back into the base. A more narrow emitter region is therefore favorable for the cell performance, because it features a pn-junction at the extremity of the shorter emitter, which limits the diffusion of holes into that direction.
As mentioned in Chapter 3.2, higher conversion efficiency is obtained for a larger emitter fraction at the rear of the cell. Nevertheless, simulations with that emitter fraction of about 80% reveal that while the J_{sc} is increased by 15%$_{rel}$ in comparison to a ratio of 1/1 for the emitter/BSF coverage on the rear side, the FF decreases for a higher emitter fraction. The FF is the relevant quantity to distinguish samples with a gap from samples with an overlap, as apparent from Table 3.5. The absolute decrease of that value also lowers the Δ, and therefore leads to a lower resolution, which is disadvantageous for experimental distinctness.

Conclusion

In conclusion, these simulations show that the introduction of an intrinsic gap region can be favorable for the characteristic quantities of non-defect free pn-junctions. The difference in FF with and without a gap region, and accordingly the experimental distinctness, can be increased by decreasing the emitter width, which is done in the so-called zebra structure.

4 Analysis and Results

The aim of this Master Thesis is to experimentally realize a single pn-junction (see Chapter 2.1.5) and to characterize that pn-junction by its J-V curve (see Chapter 2.5). The theoretical simulations supporting the experimental approach are presented in Chapter 3.3. The passivation layers and the technique for removal of the dielectric material are varied on characterized samples, while the manufacturing process is kept as simple as possible.
A schematic of a processed sample is displayed in Figure 4.1, where the sample is displayed with the rear side facing to the top and an illumination mask at some distance from the front surface for a better overview. The regions that are diffused from a patterned CVD layer and $POCl_3$ gas, namely emitter and BSF, form the pn-junction on the rear side. The rear side is passivated and SiN_x coated, besides in the opened contact areas, that are metallized to form the emitter, BSF and TLM contacts. The textured, passivated and SiN_x coated front surface faces towards the bottom. The procedure to align the sample and the illumination mask is indicated in the figure. For this purpose, the reference holes in cross-shape that are shot-through the sample, are aligned with the cross-shaped openings in the illumination mask. With an aligned illumination mask, the sample is suited for illuminated J-V curve measurement. The required processing steps and the related challenges are presented in the following of this chapter.

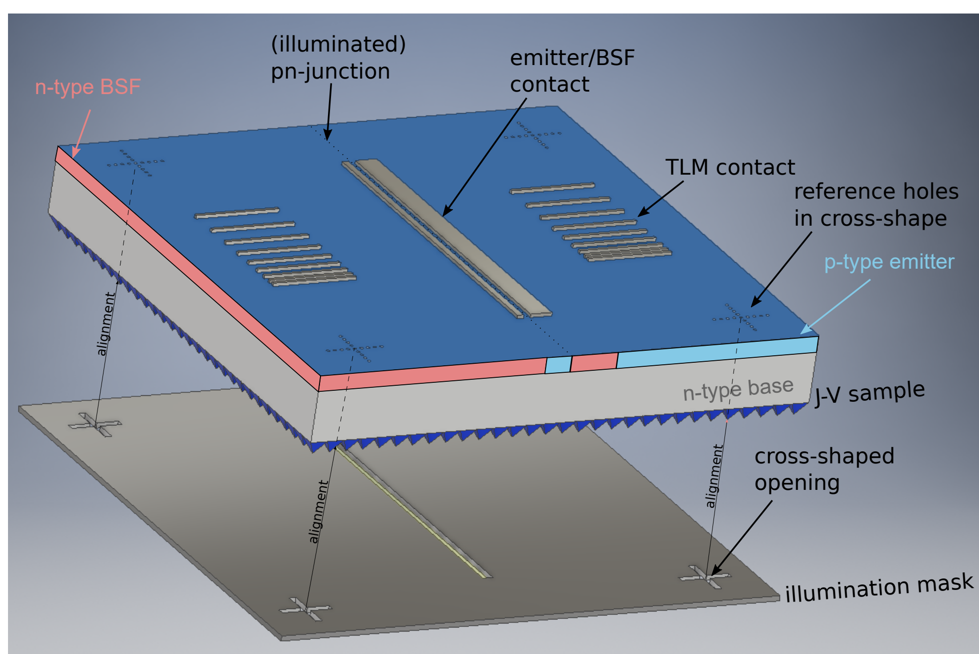

Figure 4.1: 3D schematic of a J-V sample with illumination mask; The sample's rear faces to the top; (not to scale).

The sample production process starts with n-type (7.5 Ωcm) float-zone Si material with a thickness of 250 μm and a 100-orientation that is reduced in size to quadratic samples with an edge length of 5 cm. These samples are successively chemically cleaned. In the first cleaning step the native oxide[117],[118] is etched by a 2% HF solution. This step is followed by a Piranha cleaning process[119], where the Si surface is oxidized in a solution of hydrogen peroxide and sulfuric acid

(ratio 4:1) at 80 °C to eliminate the risk of having metal or organic impurities in the top surface layer. This SiO_x layer is then removed in a clean 2% HF solution.

4.1 Chemical Vapor Deposition (CVD)

Chemical Vapor Deposition (CVD) is used to produce thin films of solid materials in this work, such as Si Oxide (SiO_x), SiO_x:B, SiN_x and a-Si. These layers serve for capping, for ARC, for passivation (detailed in Chapter 2.2.2), or as diffusion source (detailed in Chapter 2.1.4).
At this stage of the sample processing, a SiN_x layer is deposited on the front surface, while a SiO_x:B/SiN_x stack is deposited on the rear surface of the cleaned samples. In the following, the SiO_x:B layer is the B diffusion source to create the p-type emitter. The emitter plays a significant role for the effects in the pn-junction, nevertheless no full analysis of the SiO_x:B layer is performed in this work. Instead, this work relies on the experience of previous studies, such as published in the dissertation of Gloger[25] and the article of Engelhardt[27]. The large variety of parameters that have to be adjusted to produce a suitable emitter from the SiO_x:B CVD layer in the diffusion process are laid out briefly in the following.
Besides varying the type of CVD device, several parameters can be adjusted on the device itself to alter the growth of the SiO_x:B layer. One of those parameters is the gas flux that can be changed for silane (SiH_4), carbon dioxide (CO_2) and diborane (B_2H_6). Additionally, the power input, the temperature and the deposition duration can be adjusted accordingly. Furthermore, the capping layer and the post-deposition diffusion process are of high relevance for the B diffusion into the wafer and emitter formation (see Chapter 4.2.3).
These parameters are ideally adjusted to obtain an emitter of 60-80 $\Omega/\square$ with a depth of 500 nm or more with no Boron-Rich Layer (BRL) and no B depletion towards the surface. A deep emitter is necessary to prevent the emitter contact from shunting, which happens as a consequence from metal penetration through the emitter region into the base (see Chapter 4.3.3). As detailed in Chapter 2.1.4, a BRL increases the charge carrier recombination and is therefore to be avoided. A B depletion towards the surface of the wafer is disadvantageous for a low contact resistance due to the low doping concentration (see Chapter 2.3).

4.2 Local Removal of Dielectric Material

In this work photolithography and laser-ablation are employed to locally remove dielectric material. The patterning of dielectric material is used to structure the p- and n-doped areas of the wafer's rear side and the contact opening. This patterning is a highly relevant processing step since it defines the pn-junction, which is the key feature of the processed samples. This chapter therefore elaborates in detail on the removal techniques as well as on the related challenges and on the results achieved.
A comparison of local dielectric material removal with laser ablation and laser-exposed photolithography is displayed in Figure 4.2 (Scanning Electron Microscopy is explained in Chapter 4.2.2). On this exemplary sample, the CVD layer on the sample is structured with laser-exposed photolitography, thus forming a contrast line towards the center of the image (see also close-up). This line corresponds to the pn-junction of this particular sample. The contact areas are opened with laser ablation, therefore, laser spots can be observed in these areas, that appear bright on the left hand side side of the image.
Several differences between the resulting structure, achieved with laser ablation and laser-exposed photolithography, can be observed. While single laser spots can be distinguished in the ablation area, due to melting on the wafer's surface (see Chapter 4.2.2), no laser remains

can be seen with the Scanning Electron Microscopy for laser-exposed photolithography. This is due to the fact, that the laser light, used to expose the photoresist in the photolithography process, is absorbed in the photoresist, while laser light is absorbed by the Si substrate during direct laser ablation of the dielectrics. Furthermore, if the laser spots are not overlapping to a large extent during laser ablation, the edge of the ablated area is not straight but defined by the laser spots' shape (see Figure 4.2). In contrast, the pn-junction created by photolithography is defined as a rather straight line. These differences and their origin are discussed in the following two sub-chapters.

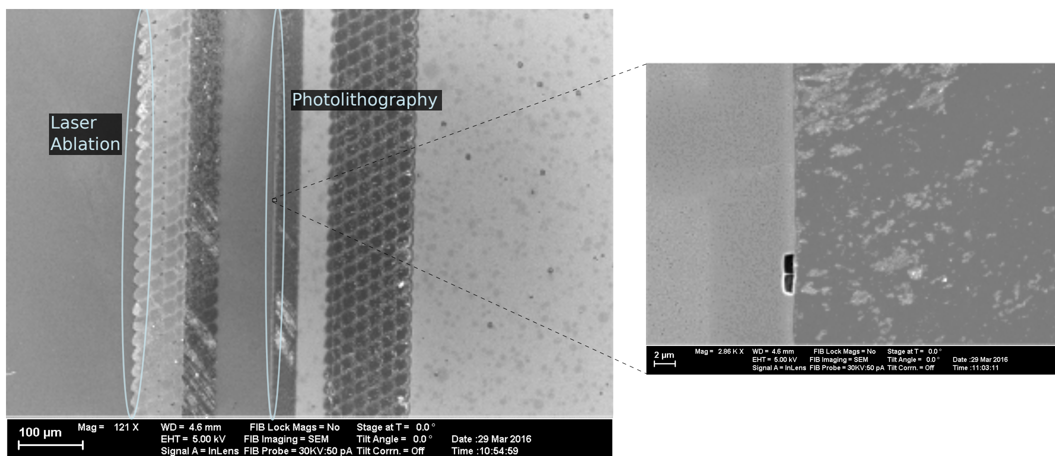

Figure 4.2: SEM image for comparison of laser-exposed photolithography and laser ablation used to pattern dielectric material.

4.2.1 Photolithography

Photolithography is a process that serves to pattern the wafer's rear side in this work and is used as a reference process to laser-ablation. Photolithography consists of a series of processing steps, of which some are more crucial than others. A compact description with detailed information about photolithography processing can be found in[120].

The laser-exposed photolithography process begins with photoresist application, followed by exposure with a laser light source. The photoresist is then developed and finally the uncovered area is chemically etched to form the pattern. In the following, some key challenges are mentioned and solutions are proposed.

Photoresist Application

The first step in photolithography is to apply the photoresist on the substrate, which in this work consists of a Si wafer covered by a CVD layer. A nitrogen gun is used to blow potential dust particles off the surface before heating the substrate to 170 °C for 30 min for dehydration. The hot wafer is placed in a petri dish, in which the primer Hexamethyldisilazan (HMDS, $C_6H_{19}NSi_2$) is evaporated and acts as an adhesion promoter for the photoresist in the next step. The undiluted photoresist AZ 4562 from MicroChemicals is spin coated onto the substrate in a two-step spin coating program. After a soft-bake in the oven, the wafer is placed in a black box over night with an open water container for rehydration.

Laser Exposure

The next step consists of laser exposure. A picosecond-microstruct laser system from 3D-Micromac with a ps pulsed laser beam and a wavelength of 355 nm is chosen for exposure. It is to be mentioned, that the laser spots overlap to a large extent to form a sharp edge of the exposed surface. This does not inflict damage on the substrate because the laser energy is absorbed by the photoresist. As can be seen in[120], the absorption of the photoresist AZ 4562 has its absorption peak very close to the 355 nm wavelength. Therefore the combination of laser and photoresist match well. Using laser exposure in contrast to exposure with a mercury-vapor lamp holds the benefit of not needing an aligned mask and therefore of freely being able to adapt the exposure pattern.

Photoresist Development

The exposed surface of the sample is developed in this processing step with the developer AZ 351B that is based on buffered NaOH and used in a 1:3 dilution. The progress can be tracked by investigating the exposed areas under the microscope. It is to be mentioned, that the compatibility of photoresist and developer is declared as a possible combination, only, by the manufacturer[120]. The development is followed by a hard-bake in the oven to increase the physical, thermal and chemical stability of the developed photoresist.

Chemical Etching

The uncovered surface is typically chemically etched in a Buffered HF solution (BHF), which is a HF solution with an addition of ammonium fluoride (NH_4F). The added NH_4F maintains a constant pH value and provides fluoride ions, hence, leading to a stable etching process[18],[121]. Usually no concentrated HF solution is used at this point because it increases the risk of peeling, stripping or dissolving the photoresist.

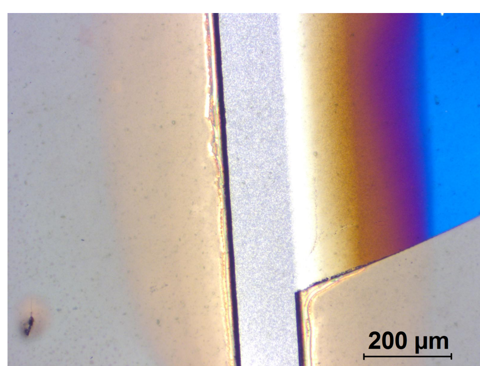

Figure 4.3: Microscope image of an under-etched photoresist; while the stripe-like opening in the photoresist is etched all the way to the silicon substrate, severe under-etching can be observed around that opening.

Depending on the CVD layers on the substrate, this step can be rather challenging. While commonly the aim is to etch the CVD layers in the direction of the surface only, under-etching of the photoresist can occur. Prominent differences are apparent in the etch rate depending on the deposited CVD layers. While as-deposited SiN_x layers show etch rates of 80 nm/min (deposited at 230 °C) and 5 nm/min (deposited at 400 °C), SiN_x layers after passing through a firing furnace occur to etch at a rate below 1 nm/min. Particularly the slowly etched samples

happen to be under-etched because the HF solution tends to strip the photoresist off the samples' surface the longer the etching takes. Increasing the HF concentration in the solution is observed to be unfavorable because it strips the photoresist more swiftly.
Figure 4.3 displays an under-etched photoresist. The image shows a contact opening that is etched to the Si in the desired stripe-like area in the center, while severe under-etching has taken place around that area. It is normal for an isotropic etchant to etch as far underneath the photoresist as it etches in depth. On this sample, however, it etched about 75 nm in depth and several hundred of μm in lateral direction. It can be seen, that the photoresist is under-etched on the left side (lighter area), while it is entirely taken off on the right hand side. The color gradient reveals that the SiN_x layer (in the thickness of an ARC) is left untouched by the HF solution on the very right hand side and is then etched thinner towards the opening, where it reaches the Si surface.
To avoid such under-etching, short etching duration in BHF are advised. If the etching duration is bound to be long due to process requirements, several preceding steps can be optimized. One solution could be to improve the photoresist's adhesion to the substrate by optimizing the pre-treatment of the substrate. Increasing the thickness of the photoresist film can prevent the film to lift off due to swelling of the photoresist film. Extending the duration and raising the heat of the soft-bake or the hard-bake can be taken into consideration to increase the cross-linking of the photoresist. It has to be remembered, that the resist removal after a more intense hard-bake is more difficult.

Photoresist Removal

After patterning the wafer's surface, the remaining photoresist is to be removed from the sample. This is done by successive immersion of the sample in three different acetone beakers that are standing in an ultrasonic bath, a beaker with isopropanol and a last one with purified water before drying it with a nitrogen gun. As mentioned earlier, an intense hard-bake can make the removal quite challenging.

Cleaning

One last cleaning step is necessary when the photoresist removal is performed with acetone. Due to its high vapor pressure, stripped photoresist re-depositions onto the substrate. This was observed during removal and is mentioned in[120]. A proposed cleaning process is the Piranha cleaning with a consecutive dip in a 2% HF solution.
This leads to the following difficulty. The HF solution dip should preferably not remove the layers deposited on the Si wafer at this stage, because they are essential for the next processing steps. Therefore, slowly etched CVD layers are useful for this etching step. At the earlier chemical etching step, however, quick etching of the CVD layer is more practicable. For this reason, a CVD layer that is etched by a 2% HF solution at a suitable speed of 5-20 nm/min is required. Making CVD layers with this property is a challenge, while meeting all other demands on the layer. This challenge cannot be pursued in this work, since no full analysis of the CVD layers is carried out (as mentioned in Chapter 4.1). The cleaning step is therefore skipped, unless stated otherwise.

Conclusion

On one hand, the photolithography process is improved up to a point, where patterning of the sample results in sharp edges with laser exposure. On the other hand, the last cleaning step

cannot be performed on the opened areas due to an unfit etch rate of the CVD capping layers (see last section). As a consequence, impurities can find their way into the wafer, leading to an increased charge carrier recombination rate.

4.2.2 Laser-Ablation

Laser-ablation is another method used in this work to locally remove dielectric material that can be realized in large-scale production. The advantages and challenges are presented in the following.

Basics of Laser Ablation

Single or multiple layers of dielectric material can be removed from a substrate by direct and indirect laser ablation. During direct laser ablation, the laser light is primarily absorbed in the dielectric covering layer, hence, clearing this layer away. Indirect laser ablation works by light absorption in deeper layers, which creates pressure, leading to the layer's lift off. Under real circumstances, laser ablation is a mix of direct and indirect ablation. Direct ablation is favorable if deeper layers should be protected from laser damage, a thin layer of the covering material is typically left on the surface. Specifically in the context of this work, damage to and melting of the Si substrate is to be reduced to a minimum.
The laser pulses' timescale has a major impact on the working principle of laser ablation. Differences in excitation, thermal effects and damage inflicted on the material are apparent. Laser pulses in the ns timescale lead to thermal laser ablation due to electron-phonon interaction and therefore thermally damage the material and alter the surface of the substrate[122]. Shorter pulses in the ps timescale still lead to linear absorption with highly reduced thermal damage, accompanied by reduced surface alteration. The effect taking place at this timescale is called cold ablation. During cold ablation, a plasma is created, that causes the ablation of the layers above[123]. For an even shorter timescale high light intensities are required, because non-linear effects play a major role. Laser ablation at the fs timescale is therefore likely to inflict damage to the substrate[124].
In this work, depending on the processing step and on the applied passivation layer, different stacks of dielectric layers are to be removed, such as SiO_x:B/SiN_x, a-Si/SiN_x and Al_2O_3/SiN_x. The varying absorption behavior of different dielectric layers, can have a major impact on the ablation process. The particularly high light absorption of a-Si is to be mentioned (detailed in Chapter 4.4.6). In the context of this work, only a one-step ablation process is considered, resulting in areas opened all the way to the substrate's surface. This implies, that laser damage is inflicted on the substrate's surface. This damage is to be reduced to a minimum.
A one-step defect-free laser ablation process is reported by Haase et al.[125],[126]. The study presents a method for local contact opening of the dielectric layer by laser ablation before metallization. The method relies on the strong absorption of a-Si (35 nm), which is coated on the Si substrate and covered by a 75 nm thick SiN_x. As a result of this study, a defect-free ablation of the SiN_x is presented, with a remaining thinned-out a-Si layer that still passivates the surface. The contact formation is performed with the COSIMA approach explained in Chapter 4.3. Since an a-Si layer covering the Si substrate is required and a thinned-out a-Si layer remains on the surface, this method can be used under certain circumstances only.
Further more complex patterning methods have been suggested by other authors, one of which was lately reported by Ring et al.[127]. This method combines laser processing and wet etching in the opened areas, with the possibility of re-passivation of the opened areas. Since this method implies a multi-step process, it is not considered as a possible ablation method in this work.
In the context of this work, a ns and a ps laser are used for laser ablation. As explained earlier,

the ps laser reduces the damage inflicted on the substrate, thus leading to a lower recombination rate at the wafer's surface. Another advantage of the ps laser is the accuracy of the ablation pattern, leading to straight lines of laser spots with non-noticeable variation of the laser spot's size, shape and ablation behavior. While the ps laser uses a mechanically movable work table to align the sample underneath the laser, the ns laser handles the laser beam with a mirror system. Consequently, the laser ablation with the ns laser proceeds at a much higher speed, hence, reducing the ablation time for large surfaces from up to 8 h to several minutes.

Laser Ablation Results

Laser ablation is performed at wavelengths of 355 and 532 nm in this work. Several other parameters can be adjusted for an appropriate ablation result, such as the laser power, the focus and the density of the ablation points. In this work, entire surface areas are to be uncovered by laser ablation. The ablation process aims at a complete removal of the covering layers while inflicting as little damage to the Si substrate as possible.
To illustrate the parameter optimization process for laser ablation, Figure 4.4 displays differently ablated areas, visualized with an optical microscope. The sample is covered with a stack consisting of a passivating Al_2O_3 layer and a 75 nm thick SiN_x layer, which gives the surface a blue color. The parameters mentioned above are varied. The laser spot density is increased from widely spaced ablation spots in (a) to adjacent laser spots touching one another in (c) for a nearly complete removal of the covering layers. While the interference patterns in the laser spots in (a) prove that not all covering layers are fully ablated, the laser spots in (b) are fully uncovered. The laser power is increased by 5% and the laser beam is fully focused to achieve this change. These parameters are altered again for overlapping laser points in (c), to reduce the damage inflicted to the substrate in the overlap region. Nevertheless, it can be seen, that the surface is 'roughened' in the overlap areas and that some covering layer domains remain in those areas.

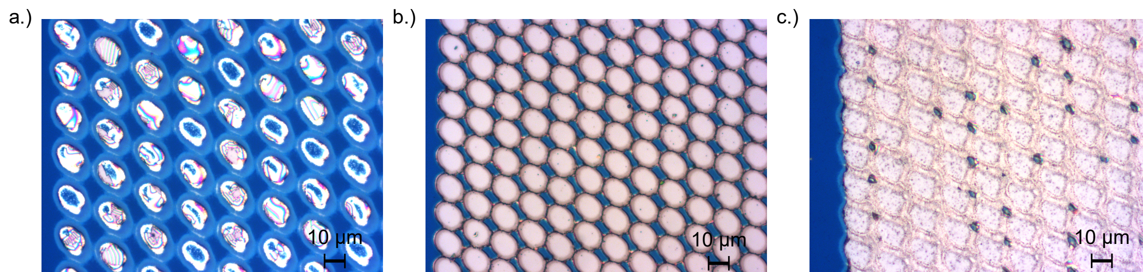

Figure 4.4: Microscope images; Variation of the laser power, the focus and the density of the ablation points on a ps pulsed laser for laser ablation resulting in a.) widely spaced not fully ablated laser spots, b.) more densely spaced fully ablated laser spots, and c.) overlapping laser spots that nearly ablate the complete surface.

For a more detailed analysis, Scanning Electron Microscope (SEM) images are taken of a laser ablated surface with a 'Neon40EsB' SEM from Zeiss. SEM measurements achieve a resolution down to the nm scale. The SEM is an electron microscope that uses a focused electron beam to scan the sample. The signals resulting from the interaction of the electron beam with atoms of the sample are received by a detector. Topography images (SE2-detector, an Everhart-Thornley detector) as well as contrast images (InLens-detector) can be taken with the SEM. These specifications are displayed at the bottom of each image obtained from the SEM. It is to be mentioned, that the contrast images are well suited to display the sample's surface composition.

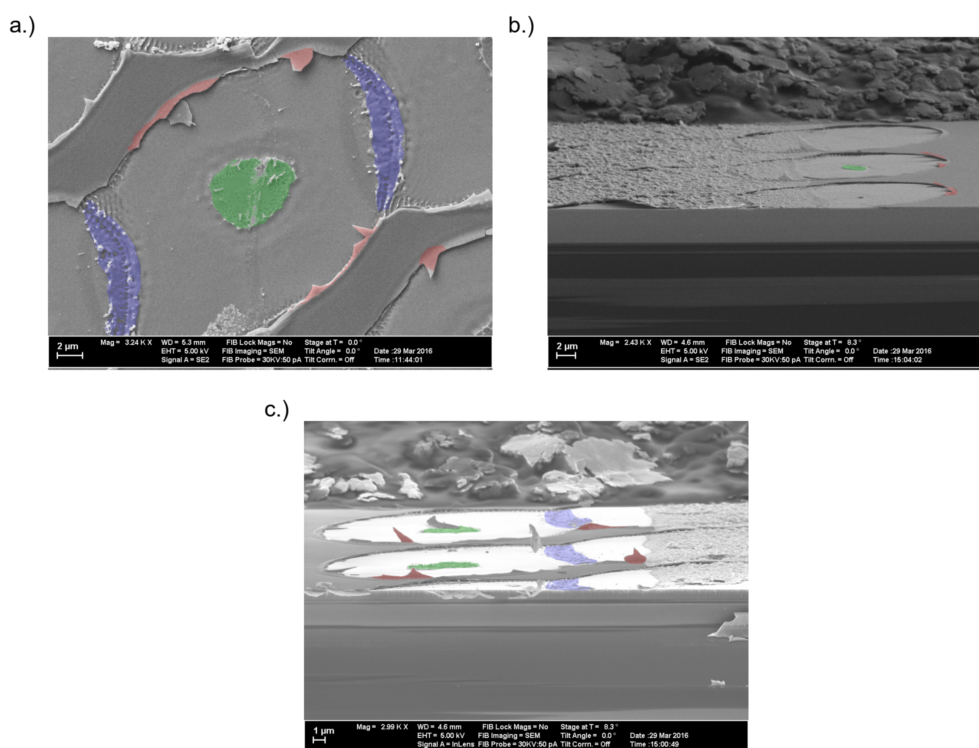

Figure 4.5: SEM images of a ps pulsed laser treated area showing roughness in the overlap area (blue), remaining covering layer in the center of the ablation spot (green) and overhanging CVD residue around the ablation points (red); a.) top view, b.) and c.) angled view.

The SEM images are displayed in Figure 4.5. The images show contact openings, that are partly covered by metal. While image (a) is a top view, images (b) and (c) are angled views on the sample. It can be seen, that coated areas remain between fully ablated lines. As apparent from the optical microscope images in Figure 4.4, in the overlap areas (colored in blue in Figure 4.5) the surface is roughened, possibly due to melting of the substrate.
To analyze the sample's surface, additionally to the SEM images, Energy-Dispersive X-ray spectroscopy (EDX) measurement is performed. For this purpose, the atoms in the sample are excited in the spot of irradiation by the focused electron beam. An EDX detector, that is integrated in the SEM, measures the X-rays emitted by the atoms. Since these X-rays are characteristic to the various atoms, corresponding to energy levels in the atomic structure, the element composition of the analyzed spot on the sample can be determined.
Two additional features can be seen in the SEM images, that are not visible in the optical microscope images. One of which is an area in the center of the laser spot that seems to be not ablated. This area is created by a high laser power concentration in the center of the laser point. Since the intensity profile of the laser beam corresponds to a Gaussian beam, the highest laser power strikes the material in proximity of the spot's center. If the power attains a certain threshold, the layers covering the Si are melted without extrication from the Si and solidify again on the Si substrate. EDX measurements indicate, that a considerable amount of N is contained in this layer. The detachment process of SiN_x layers on Si is discussed and correlated to mechanical stress in the wafer in[128]. In that study, also non-detached spots in the center of the laser point are identified.
Another important aspect are the numerous overhanging SiN_x edges around the ablation points. The overhanging CVD residue (colored in red) uncover the surface, while shading it. This can be rather problematic for further layer deposition, because the desired layers might not fully cover the opened surface in the shaded areas.

Laser Doping

As mentioned earlier in this chapter, ns laser ablation is thermally induced. Besides inflicting damage to the substrate, the thermal input can also have further consequences, depending on the covering layers that are removed. One specific effect, that has been identified in the course of this work, is laser induced doping. During the process of making the single pn-junction samples, a SiO_x:B/SiN_x stack, with a layer thickness of 40 nm each, has to be removed from the Si substrate to allow B doping in the covered areas and P doping in the opened areas during the ensuing diffusion step.
If the layer stack is removed by ns laser ablation, doping at the sample's surface is observed. This does not occur when the layer stack is ablated with a ps laser. The dopant diffusion into the substrate is generally deduced from Four Point Probe (4PP) Resistivity Measurement and the doping profile is measured by Electrochemical Capacitance-Voltage profiler (ECV) measurement on several samples.
A 4PP measurement device has four aligned equidistant point probes that serve to induce a current or to measure a voltage between the probes. A current is induced by the two outer pins while a voltage is measured between the two inner pins to measure the sheet resistance R_{sheet} by 4PP. The sheet resistivity of an infinite sheet is calculated by the formula[129]

$$R_{\text{sheet}} = \frac{\pi}{\ln(2)} \frac{V}{I} \tag{4.1}$$

$$[R_{\text{sheet}}] = \frac{\Omega}{\square} \tag{4.2}$$

For an accurate measurement, it is essential that the current only passes through the layer that is to be measured. Ideally a pn-junction separates the generated charge carriers from the bulk and only the layer to be measured shows a low resistivity. The sample should be measured in a dark environment to prevent the generation of additional free charge carriers.
The ECV measures the electrically active dopant concentration as a function of the depth and draws a doping profile with that data. The measuring procedure consists of consecutive CV measurements and etching cycles. The etched depth can be calculated by the Faraday's law of electrolysis[130]. Since a Schottky-like contact (see Chapter 2.3) is formed between the electrolyte etchant and the semiconductor on the entire contact surface, the Mott-Schottky equation[131] can be used to calculate the carrier concentration at the border of the depletion layer in the semiconductor. Adding etched depth and depletion width results in the total depth that is combined with the carrier concentration to draw the doping profile.
The pre-diffusion doping profile measured by ECV measurement in Figure 4.6 reveals, that p-type doping occurs in the first 300 nm from the surface due to ns-laser ablation of the SiO_x:B/SiN_x stack. The in-diffusion of acceptor atoms is expected to result by B diffusion from the thermally ablated SiO_x:B layer into the substrate. Since the opened area is to be n^+ doped in the ensuing diffusion process, p doping in this area is inconvenient for the resulting doping profile (see Chapter 4.2.3) and the amount of recombination centers. The B profile appears to reach approximately 200-300 nm into the substrate and is therefore much deeper than the initial layer stack's thickness, and the peak p-doping concentration is in the order of 10^{20} cm^{-3}. It can therefore be expected, that the ECV does not measure remains of the covering layers but an actual doping profile in the Si substrate. As a confirmation, the samples are dipped in a HF solution until they are hydrophobic and measured again, resulting in the same profiles. Due to the laser-altered surface, the evaluation of the ECV measurement results generally leaves a certain room for interpretation, however.

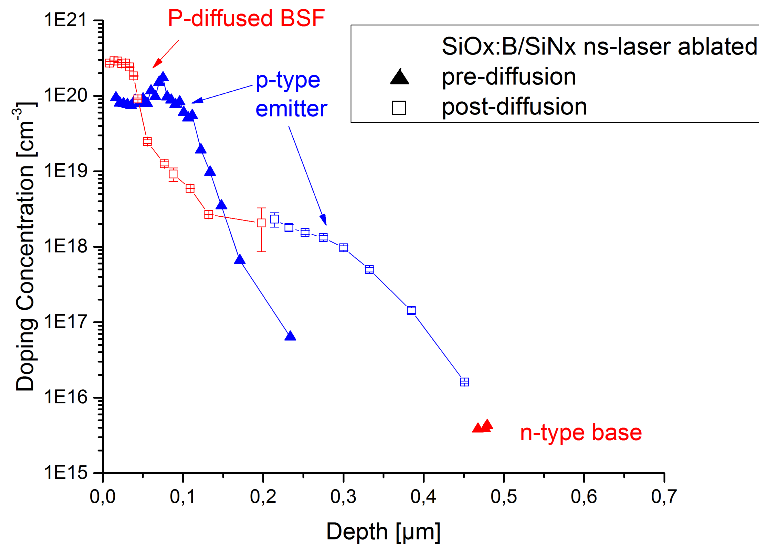

Figure 4.6: ECV measured doping profiles revealing laser doping into the substrate due to ns-laser ablation of a SiO_x:B/SiN_x layer, measured before and after the diffusion step.

The same laser doping effect could be observed for SiN_x/SiO_x:B/SiN_x stacks, resulting in a much lower peak B doping concentration of $\sim 5{\cdot}10^{18}$ cm^{-3} and a B doping profile's depth of less than 100 nm. This indicates that the p-type doping is not a product of the deposition process, since the substrate is capped by SiN_x before the SiO_x:B deposition, which does not yield acceptor atoms.
While doping due to ns laser treatment is an undesired side effect in the context of this work, it can be of relevance for other processes. The composition of the covering layers can most likely be adjusted to achieve higher and deeper doping profiles with the ns pulsed laser.

Conclusion

Several difficulties related to laser ablation, such as melting of the substrate, overhanging CVD residue of the ablated layers and laser doping, make the use of laser ablation challenging. The implementation of laser treatment to remove dielectric layers has to be reviewed in every new occurring situation. Nevertheless, satisfactory results can be achieved with laser ablation if all difficulties are overcome.

4.2.3 Creating pn-Junctions

At this stage of the sample processing, certain areas of the SiO_x:B/SiN_x stack, that fully covers the rear side of the sample, have to be locally removed to pattern the sample (see Figure 4.7ii). This is done by photolithography or laser ablation, as explained in the last two sub-chapters. In the next step, the sample is heated in a diffusion furnace while running a sequential diffusion process with the introduction of $POCl_3$ gas in the second part of the diffusion process (more information in Chapter 2.1.4). The resulting doped Si substrate after diffusion consists of an emitter in areas that are covered by the SiO_x:B/SiN_x stack and a BSF in opened areas that are doped by the $POCl_3$ gas (see Figure 4.7iii). The front side and areas on the rear surface that

are covered by a SiN_x layer are left undoped.
The most important component, that is created in this diffusion step, is the pn-junction on the rear of the sample. As mentioned in the introduction, pn-junctions formed by photolithography are straight, while the pn-junctions created by laser ablation follow the laser spot's edge. If the laser spots do not overlap to a large extent, the laser treated pn-junction is not formed in a straight line, thus increasing the effective length of the pn-junction over a certain distance.

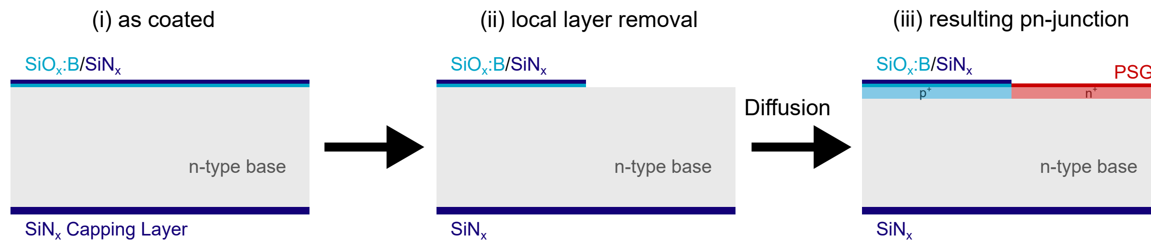

Figure 4.7: Schematic cross section showing the process from a coated sample to a pn-junction after in-diffusion (not to scale).

For this doping to be successful, it is essential, that the CVD layers are entirely removed in order to avoid B is diffused into the BSF region during the diffusion process. As detailed in Chapter 4.2.1, this procedure is fruitful with photolithography, if the HF solution etches the CVD layers at a suitable speed, as to be able to perform the last cleaning step. Without this cleaning step, impurities on the substrate's surface are likely to diffuse into the substrate during the diffusion process and to noticeably increase the recombination. For full removal of the CVD layers with laser ablation, the experience shows that the laser spots have to slightly overlap, thus leading to a roughened surface in the laser spot overlap region as a side effect (explained in Chapter 4.2.2).
The realization of this laser ablation procedure is accompanied by a difficulty related to laser doping, discussed in Chapter 4.2.2. The ablation of the SiO_x:B/SiN_x stack with the ns pulsed laser results in B doped regions. This is a problem, because these areas are to be doped with P or entirely undoped instead (gap region, see next section). The sequential diffusion process, that contains a $POCl_3$ diffusion step, does not overcompensate for the B doping with P doping on the entire depth for the chosen diffusion parameters. Instead, B limits the diffusion of P into the wafer and itself diffuses into the wafer up to a depth of more than 400 nm, as revealed by ECV measurements (see Figure 4.6), therefore creating a p-doped region. In the 200 nm closest to the surface, the B doping is overcompensated by the n-type BSF that results from the $POCl_3$ diffusion. The result is a p-doped region between the BSF and the base. For this reason, the ns laser is not suitable for the SiO_x:B/SiN_x stack ablation close to the pn-junction and ideally, the ns laser is not used to ablate this stack at all. Laser ablation with the available ps laser takes much longer, however. Since the ablation duration for the standard structure is about 1:10 h long, only a limited amount of samples can be processed. Owing to uncertainty concerning the stability of the SiO_x:B layer, the samples should be deposited, ablated and diffused on the same day, therefore reducing the amount of samples processed in a day and increasing the processing costs.
A capping layer such as SiN_x covering the SiO_x:B layer is essential to hinder P diffusion through the SiO_x:B layer into the emitter region (see Chapter 2.1.4 and simulation in[25]). P diffusion through the SiO_x:B layer during the diffusion process is observed in this work on test samples. As a result of the diffusion process, samples diffused with a SiO_x:B/SiN_x stack yield a B doped emitter, while samples diffused with a SiO_x:B layer, only, additionally feature a P doped region close to the surface. This leads to two pn-junctions along the depth in the surface region (see Figure 4.8).

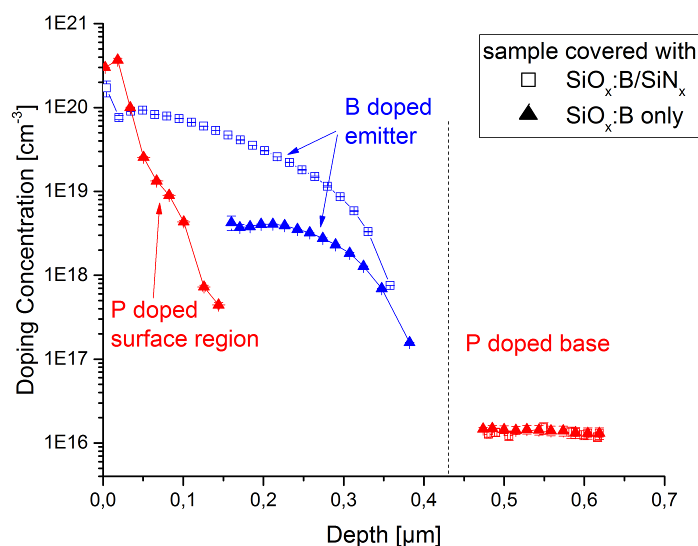

Figure 4.8: Doping profiles measured with ECV after sequential diffusion of a sample covered by a SiO_x:B/SiN_x stack and a sample covered by a SiO_x:B layer only; the samples with non-capped SiO_x:B layer feature an additional unwanted P doped region at the Si surface.

Creating Gap Regions

The pn-junction is to be formed with and without an intrinsic gap region on different samples. For the investigation of gap's impact, laser ablation is chosen as industry-based process for the creation of samples with a gap region in the pn-junction. While one single ablation step is sufficient to make samples with no gap region, more than one laser treatment is necessary to form the gap, thus implying further processing challenges.
In a first laser treatment, the SiO_x:B/SiN_x stack is ablated in the area that is to form the intrinsic gap region (see Figure 4.9ii). In a further CVD step, an additional SiN_x layer is deposited on the sample's rear side, and a supplementary ablation step removes the SiO_x:B/SiN_x/SiN_x layer stack in the BSF areas, while leaving the layers in the gap and emitter area intact (see Figure 4.9iii). This creates an area, between the opened area and the surface coated with the SiO_x:B/SiN_x stack, which is coated with a SiN_x layer only. This SiN_x layer caps the surface from the $POCl_3$ gas and does not act as a dopant source during diffusion. This area will therefore result in an undoped region that forms the intrinsic gap. As a consequence, the surface of the BSF region is uncovered before diffusion, while the gap region is covered by SiN_x and the emitter region is covered by a SiO_x:B/SiN_x stack (see Figure 4.9iii).

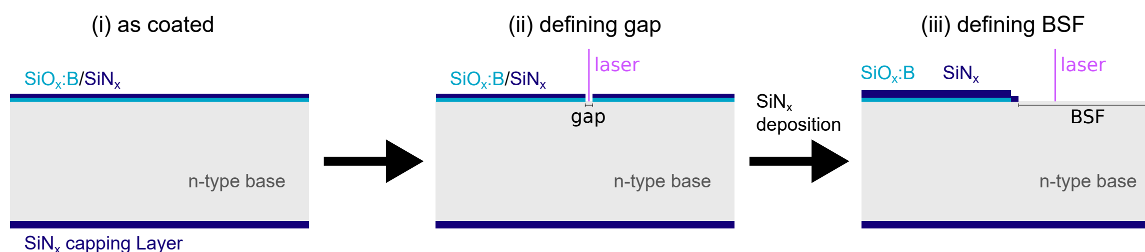

Figure 4.9: Schematic cross section showing the process from a coated sample to a coating pattern, which allows the diffusion of a pn-junction with an intrinsic gap (not to scale).

A difficulty, related to the creation of a gap region, is the alignment of the laser lines to form a gap with even width. This difficulty is illustrated in Figure 4.10 with SEM images of samples that are processed slightly differently, than the procedure introduced above. The difference consists in laser ablation of the SiO_x:B/SiN_x stack in the entire BSF and gap area during the first laser treatment step instead of ablating the gap area only (see Figure 4.9ii). As a result, the BSF area is ablated for the second time, when uncovering it from the deposited SiN_x. The laser processing difficulties occurring in this laser ablation procedure are transferable to the procedure introduced earlier.
The SEM images in Figure 4.10 display the sample's patterned rear surface. The bright part at the bottom of the images in Figure 4.10 is the area that is laser treated twice, while the darker area at the top of the images is coated with the SiO_x:B/SiN_x stack and again with SiN_x. Between these two areas, an uneven line can be seen. The SiO_x:B/SiN_x stack in the area of that line is removed in the first laser treatment, while the SiN_x layer remains in that area after the second deposition step. The purpose of this line is therefore the creation of the gap between the doped regions. The formation of the intrinsic gap area with laser ablation introduces several difficulties, that are presented in the following. These difficulties mainly result from the laser ablation artifacts presented in Chapter 4.2.2, namely the roughened surface in the laser spot overlap area and overhanging CVD residue at the laser ablation spot edges.

Roughened surface: It can be observed that the gap does not have the same width at all positions. This is due to a lower adhesion of the single SiN_x layer on the roughened surface. Figure 4.10c displays an opened double line on the right hand side, that is ablated one single time. The roughened surface at the edge of the laser spots can be seen. The SiN_x layer that covers areas that are laser treated one single time reproduces this pattern (as can be seen at the bottom of Figure 4.10c). Due to the topography in that area, voids between the SiN_x layer and the substrate are possibly created, suggesting that P could diffuse underneath the SiN_x layer during the ensuing diffusion process. Furthermore, this uneven surface in the overlap area between the laser spots is unsuited for SiN_x adhesion. The second laser treatment, conducted in extension of the double line from the right in Figure 4.10c (indicated by ellipses drawn in the image), makes this apparent. As intended, the ablation fully removes this layer along the ablation lines, but ablation also occurs in areas at a distance of up to 5 μm above the actual ablation lines, in an area where the gap ought to be and where consequently a SiN_x capping layer is required. The SiN_x layer is lifted-off in the area of roughened surface. As a consequence, the gap is not well defined, which is problematic for the interpretation of the experimental results of the *J*-*V* characteristic. By adjusting the laser parameters and by shifting the second ablation line to an adequate position, the variation of the gap's width can be limited.

Overhanging CVD Residue: Furthermore, overhanging CVD residues are revealed by the SEM images in Figure 4.10 (colored in red). The overhanging residue around the ablation points of the first laser treatment shades the surface underneath. This could result in uncovered surface areas near the SiO_x:B/SiN_x layer after the SiN_x deposition step. As a consequence, $POCl_3$ gas would reach that surface during the diffusion process and P would diffuse into the Si substrate in areas adjacent to the created emitter region. As a consequence, unwanted BSF regions would be created in the designated gap area, which would highly inflict on the pn-junction's performance. This P diffusion is not looked into in this work, however, a procedure to investigate whether a considerable amount of P diffuses into the substrate is proposed. For this purpose, a p-type sample can be prepared by covering it with SiN_x. This first SiN_x layer is then ablated in a pattern that uncovers a considerable amount of the surface to create a large amount of overhanging CVD

residue (e.g. thin stripes that consist of one single laser ablation line each). The surface is then covered by another SiN_x layer and processed in a $POCl_3$ diffusion, followed by a dip in a HF solution. There is a chance of measuring P with ECV measurement, which would be a sign for the in-diffusion of P in the shaded areas.

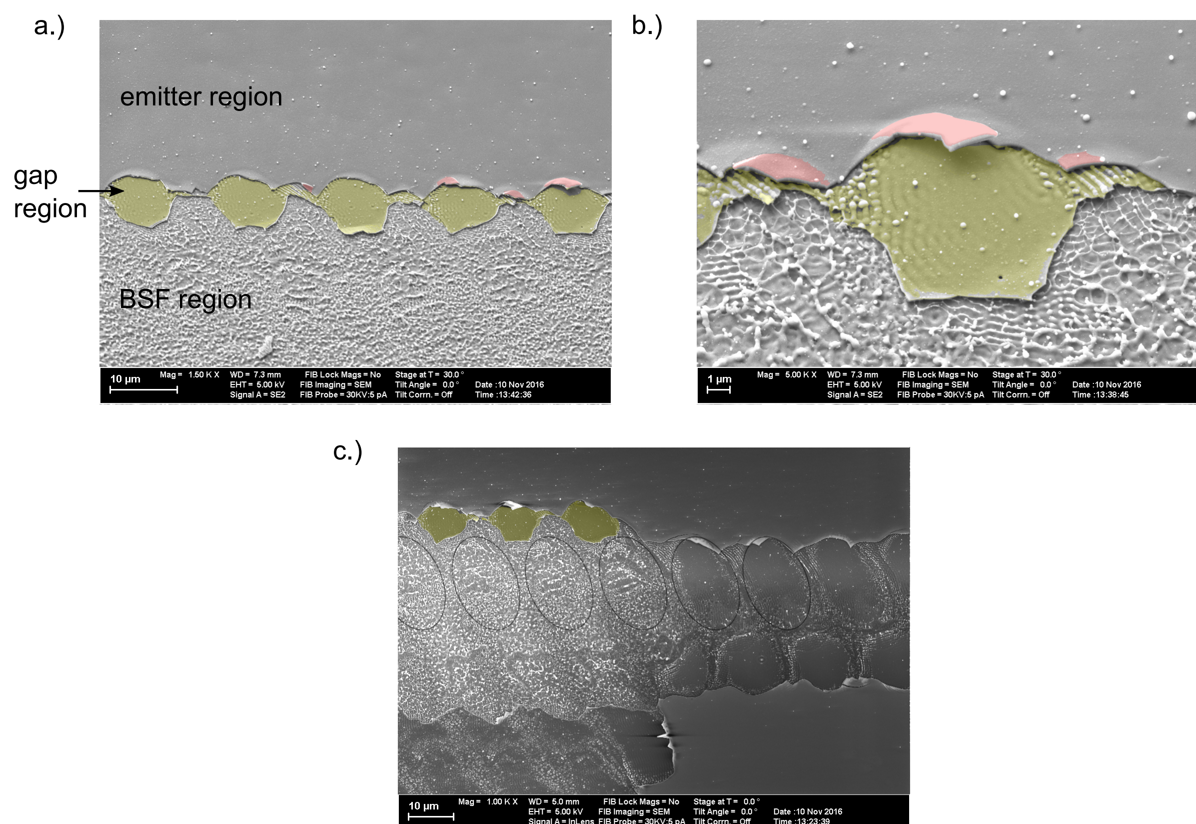

Figure 4.10: SEM images illustrating the challenges in making a gap region between the highly doped regions of a pn-junction with laser ablation; The smooth looking area on the top is the designated emitter region, the bright area at the bottom the BSF region and the 'line'-shaped area in between the gap (yellow); a,b: angled view at 30°; c: top view;.

Applied Laser Process: In conclusion, the applied laser treatment used to create a pn-junction with gap, that takes some of these problems into consideration, is recapitulated and further detailed in the following. In a first laser treatment, the SiO_x:B/SiN_x stack is only ps ablated in the area of the gap and the sample is covered with another SiN_x layer. In this step the formation of some overhanging CVD residue around the laser spots, that shade areas from SiN_x deposition, are likely. However, no laser doping is performed during the ablation process, due to the usage of the ps-laser. In a second laser treatment, only the BSF region is ablated. Therefore, no surface is required to be ablated twice, which limits the damage inflicted to the substrate. The laser lines of the two laser treatments are aligned to create a gap region with a rather constant width. As displayed in Figure 4.11, part of the SiO_x:B/SiN_x/SiN_x stack is ablated with the ns laser and while the area around the gap area is ablated with the ps laser. At the point of processing these samples, the difficulty concerning laser doping was not yet known to the author. Potential laser doping was believed to be overcompensated in the ensuing $POCl_3$ diffusion, which was however not the case with the chosen diffusion parameters. It can be observed, that, regardless of the problem introduced by laser doping, the border of the ns laser ablated line is too rough to create a well defined pn-junction with the ns pulsed laser, which is why the ps laser is always employed to define the junction.

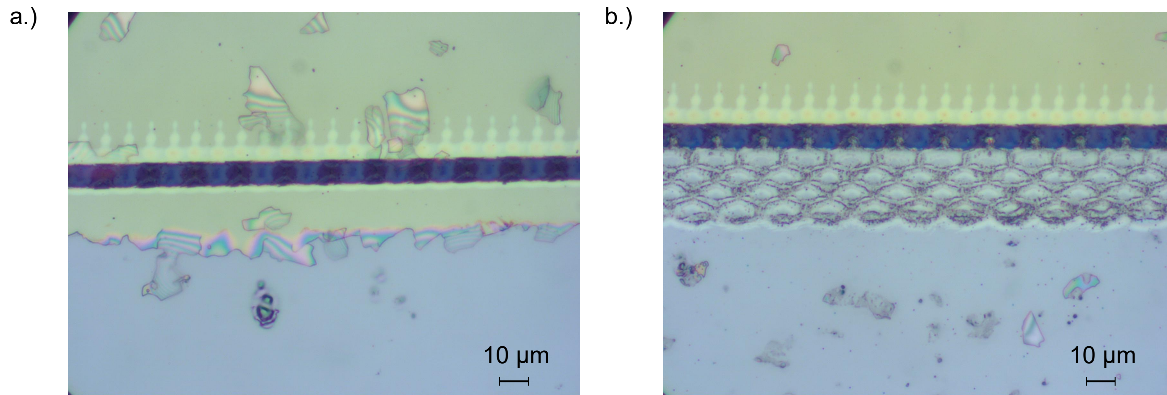

Figure 4.11: Microscopy images of samples in two stages of the laser treatment applied to create samples with a gap region between the highly doped regions on the rear side; a.) the dark blue gap area in the center is covered by the SiN_x layer, the light blue top area is uncovered by ns laser ablation and the green areas are covered by a SiO_x:B/SiN_x/SiN_x stack; in b.) the area close to the pn-junction is additionally ablated by the ps laser.

KPFM Analysis of the pn-Junction

One idea for further investigation of the pn-junction is to use Kelvin Probe Force Microscopy (KPFM). KPFM measurements combine Atomic Force Microscopy with a work function measurement of the surface. Resolving the work function of the surface helps to identify the pn-junction and to investigate its properties. Differences in doping of diffused regions can be recognized and the shape of the gap region can be analyzed. This measuring method has therefore the potential to give insight into the characteristic of the pn-junction[132].
Even more information can be gained from resolving the pn-junction in dependence of the depth by polishing the sample down in a certain angle[133]. A polishing procedure is required that produces a flat surface with no scratches. Due to the angled polish, the surface resolution of the work function measured with KPFM corresponds to a resolution in depth. This information is relevant to understand the dopant co-diffusion at the junction.

4.2.4 Contact Opening

After creating the pn-junction by dopant diffusion, the samples are immersed in HF solution to chemically etch the SiN_x, SiO_x:B and PSG layers off the Si substrate. The uncovered rear side is capped with a SiN_x layer that resists the isotropic texture etch solution in which the samples are immersed in the next processing step to texture the front surface. The reason for texturizing the samples at this processing stage, only, is explained in Chapter 4.4.6. Another immersion in HF solution frees the rear side from SiN_x and both surfaces are cleaned in a Piranha cleaning process. This step is followed by deposition of a passivation layer and a SiN_x layer on both surfaces. The SiN_x layer functions as ARC on the front and as protection layer on the rear side. The 'cold' SiN_x layer covering the passivation layer is deposited at 230 °C, only, in order to influence the passivation layer to minimum due to a limited thermal input. Thereafter, the dielectric layers covering the areas, where the contact openings ought to be, have to be locally removed. This can be done by photolithography as well as by laser ablation. In the same processing step, cross-shaped reference holes are shot through the sample, which are relevant for the alignment method discussed in Chapter 4.5.2.
Photolithography is used on several samples to remove the dielectric layers from the contact openings. Due to the high etch rate of the cold SiN_x layer in HF solution, the last cleaning step after photoresist removal cannot be performed (see Chapter 4.2.1). Due to the resulting

impurities on the contact openings' surface, the recombination is expected to be rather high at the contacts.
In this work, direct laser ablation of the contact openings is performed with the ps laser, thus inflicting some damage to the substrate (detailed in Chapter 4.4.4). Alternative methods that are mentioned in the first part of Chapter 4.2.2 are not performed as to reduce the risk of introducing processing difficulties to a minimum. Different laser patterns to remove the dielectric layers on the rear side are imaginable. Three of those are presented in Figure 4.4, where the opened fraction is varied. Samples processed in this work, are fully freed from the dielectric layers in the contact openings, unless stated otherwise. The advantage of this approach is, that the problems occurring at the edge of the laser spots are moved to the verge of the ablation field, only. Furthermore, the size of the contact openings can be reduced if the opened fraction is increased, while maintaining the same contact resistance (detailed in Chapter 4.3). The difficulties arising during the metallization process, resulting from overhanging CVD residue and a roughened surface, are discussed in Chapter 4.3.3.

4.3 Metallization

The locally created contact openings (see Chapter 4.2.4) are to be metallized for contact formation. In general, IBC solar cells feature a complex metallization pattern on the rear side, such as the ones reported in[80],[134]. For this single pn-junction, a simple metallization along the pn-junction is sufficient. For this purpose, a mask is positioned on the sample (see Chapter 4.3.2) and the metal is deposited with an electron gun.
The deposition of evaporated metal on the Si substrate inflicts damage to the substrate, due to the thermal input of the impinging metal particles and the creation of stress between the metal layer and the substrate[135],[136]. A post-deposition thermal anneal can reduce the recombination centers in the substrate[135]. While this effect is not further investigated in this work, a thermal anneal is performed anyway. The thermal input during the thermal annealing process can simultaneously help to form a contact between the deposited metal and the substrate, thus reducing the contact resistivity (discussed in Chapter 4.3.1). Furthermore, thermal annealing is required to activate the passivation layers covering the substrate material (discussed in Chapter 4.4.4).

4.3.1 Contact Formation

Contact formation between the metal and the substrate in the contact opening areas is discussed in this section. A measure of the contact's quality is the specific contact resistivity ρ_c, which is measured in the units mΩcm^2. The Transfer Length Method (TLM) measurement technique is used to determine the contact resistance. Every J-V sample features a TLM structure on the BSF and emitter region to measure the contact resistance during the annealing process (see Figure 4.1).
To perform a TLM measurement, metal contacts with a defined length and width are variously spaced in a specific region of the sample. Pins measure the resistance between pairs of contacts by applying a voltage and measuring the resulting current. The total resistance consists of the two contact resistances R_c and the resistance of the semiconductor in between the contacts, thus following[137]

$$R_\mathrm{total} = 2R_\mathrm{c} + \frac{R_\mathrm{sheet}}{W}L \qquad (4.3)$$

where W is the width and L the length of the area between the contacts. Therefore, measurements of the total resistance between contacts of varying distance L from one another yield the

contact resistance and the sheet resistance. With knowledge of the contact area, the specific contact resistivity ρ_c can be calculated.
TLM measurement results on emitter and BSF regions are displayed in Table 4.1. First of all

Table 4.1: Results of the TLM measurements performed on emitter and BSF regions with varying R_{sheet}.

Emitter				BSF			
	Contact pre-anneal		Annealed		Contact pre-anneal		Annealed
R_{sheet} [$\Omega/\square$]	Al_2O_3	a-Si	ρ_c [mΩcm^2]	R_{sheet} [$\Omega/\square$]	Al_2O_3	a-Si	ρ_c [mΩcm^2]
75	Yes	Yes	20±1	16	Yes	n/a	9±2
100	Yes	No	23±3	30	Yes	No	11±2
140	Yes	No	24±5	75	Yes	No	24±1

it is to be mentioned, that ρ_c values correspond for samples with both passivation layers in the annealed state independently of R_{sheet}. Furthermore, no difference in ρ_c is observed in dependence of technique used to remove the dielectric layers from the contact openings. ρ_c values are therefore listed independently of the passivation layer and the contact opening technique used.
It can be seen, that ρ_c does not change, while the R_{sheet} of the emitter varies between 75 and 140 $\Omega/\square$. This contact resistivity applies for annealed samples only, however. While Al_2O_3 passivated samples, that are metallized with Ti/Pd/Ag, are well contacted before the annealing step, a-Si passivated samples, which are metallized with Al/Ag, need an annealing step of about 5 min at 400 °C to form a decent contact with the substrate for samples with an R_{sheet} of 100 and 140 $\Omega/\square$. The samples with $R_{\text{sheet}} = 75\ \Omega/\square$ are well contacted without an annealing step for either passivation layer.
While ρ_c yields a very similar value for an emitter and a BSF with $R_{\text{sheet}} = 75\ \Omega/\square$, differences in the specific contact resistivity are obtained for highly doped BSF regions. A noticeable difference in ρ_c is realized when altering the R_{sheet} from 75 to 30 $\Omega/\square$. This reduces ρ_c from 24±1 to 11±2 mΩcm^2. While Al_2O_3 passivated samples are well contacted in the pre-annealed state, all a-Si samples need a thermal annealing step before the contact between metal and substrate is formed.
The optimum values of the specific contact resistivity reported in[93] are $\rho_{c,\text{Ti/Pd/Ag}} = (0.9 \pm 0.3)$ mΩcm^2 and $\rho_{c,\text{COSIMA}} = (0.75 \pm 0.1)$ mΩcm^2 on a 90 $\Omega/\square$ n^+ emitter. In comparison, the values obtained in this work are high. This discrepancy in contact quality can result from several factors, that are not further investigated in this work. The contact areas for the pn-junction contacts are comparatively large, which is why a specific contact resistance in the order of $\rho_c = 20$ mΩcm^2 is sufficiently low for the current transport of an illuminated pn-junction.
In conclusion, no significant difference in ρ_c is observed, when contacting a n- and p-doped region with the same sheet resistance. The fact that Al and Ti, both of which are used in direct contact with the Si substrate, are able to form ohmic contacts on both Si semiconductor types, was mentioned in Chapter 2.3. This appears to hold up for these findings. While the contact forms more easily on highly doped surfaces, no noticeable difference in ρ_c is seen for $R_{\text{sheet}} \geq 75\ \Omega/\square$. In general, a lower contact resistance is expected for regions with high doping concentration (see Chapter 2.3). According to the results, this has an impact on the highly P doped BSF region only. The results show that the contact formation on samples with a-Si passivation typically requires a thermal annealing step. The necessity for an annealing step is explained by the COSIMA technique, which is depicted in Chapter 2.3.

4.3.2 Metallization Mask

A metallization mask is used to define the surface area, which is to be coated with metal. The metallization mask consists of magnetic V4A steel (1.4031Mo) and is laser cut into the desired shape. During the metal deposition in the electron gun, the mask is placed between the metal source and the sample, in direct contact with the rear side of the sample. Accordingly, the mask prevents metal deposition where it covers the sample and allows metal deposition in open areas of the metal mask. The sample is 'sandwiched' between the mask and a 50x50 mm^2 square metal sheet (made out of the same material than the mask) and held together by placing NdFeB magnets on that sheet. This way, the metal mask lies tightly on the sample's rear surface.
The alignment of the mask on the sample's rear surface is key for a precise metallization of the sample. Since the opened surface areas are clearly visible on the sample's rear side, an alignment error is unusual. The laser shot-through crosses (see Chapter 4.5.2) allow alignment fine tuning. The final alignment procedure is conducted with help of a microscope, as to achieve a mask alignment accuracy of 20 μm or higher.

4.3.3 Shunting

While the alignment concept to avoid shunting is explained in Chapter 4.5.2, this section concerns itself with shunting due to an error in the metallization concept. The general problem of shunting a BC-BJ solar cell is discussed in Chapter 2.4.2. Severe shunting is observed on several sample batches, this is why a detailed analysis of this problem is given in the following.

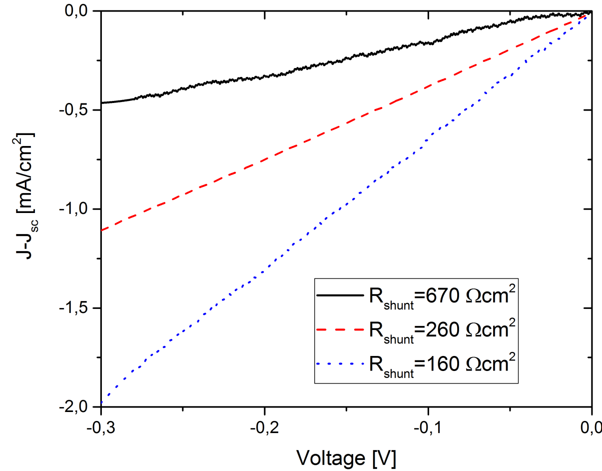

Figure 4.12: Measured J-V curves at reverse bias voltage with varying shunt resistance R_{shunt} of 670, 260 and 160 Ωcm^2; The short circuit current is subtracted from each of the curves for better comparison.

In this work, shunting is first observed on samples where the pn-junction is formed by photolithography as well as by laser ablation, resulting in an emitter with $R_{\text{emi,sheet}} = 75\ \Omega/\square$ and a BSF with $R_{\text{BSF,sheet}} = 16\ \Omega/\square$. An Al_2O_3 passivation in combination with laser ablated contact openings and a Ti/Pd/Ag metallization is used. TLM measurements yield results as displayed in Table 4.1 of Chapter 4.3.1. Some of the samples are thermally annealed for 30 min at 400 °C in a furnace. These samples feature a shunt resistance of $R_{\text{shunt}} = 160\ \Omega\text{cm}^2$ and lower, thus leading to poor FF and V_{oc} values. This is described in Chapter 2.5.1, where

$R_{shunt} = 160\ \Omega cm^2$ corresponds to the blue J-V curve in Figure 2.11. According to Quokka simulations, this shunt lowers the FF by $9\%_{rel}$, hence, having a large impact on the experimental distinctness, that is discussed in Chapter 3.3. One exemplary measured J-V curve at reverse bias voltage with $R_{shunt} = 160\ \Omega cm^2$ is displayed in Figure 4.12, where J_{sc} is subtracted from the total measured current in the cell, as to facilitate the comparison with other measured J-V curves.
A shunt current path is created, if the emitter contact touches the base or BSF doped region or if the BSF contact touches the emitter doped region. A current path between the two contacts of different polarity is then available that circumvents the pn-junction by passing through the BSF and base region or the emitter region, only. Several hypotheses to explain the low shunt resistance are developed. One of which suspects an electric contact between the contacts of different polarity via a conductive path on the sample's surface. Further possible explanations of the shunt problem imply a shunt of the emitter contact through the emitter region into the base (see Figure 4.13iv).

Conductive layer on sample's surface: As the samples are metallized by an electron gun with use of a shading mask (see Chapter 4.3.2), an alignment error has to be taken into consideration as a cause for the shunt (see Figure 4.12ii). In this context, a misalignment of the contacts represents itself as metallization of one contact being deposited on the area of the opposite doped region. A misalignment of the contact metallization is possible even if the mask is perfectly aligned on the sample, because the area of contact separation is shaded by a part of the mask that is 200 μm wide and 36 mm long, and thus easily distorted by the influence of magnets. As a result of contact metallization misalignment, incomplete SiN_x covering of the oppositely doped region (e.g. due to pinholes) can cause a shunt path between the contact and that region. Furthermore, a severe shunt is expected if one contact touches both contact openings. However, investigation with an optical microscope reveal (see Figure 4.14), that the alignment method (presented in Chapter 4.5.2) works well on all samples and that no misalignment of the contacts occurs.
Imperfect covering by the metallization mask is also taken into account. As a consequence, metal could creep underneath the mask during the deposition process, which would lead to a thin metal layer that connects the two contacts (see Figure 4.12iii). Removing the layers covering the substrate along the pn-junction by laser ablation, leads to a perfect separation of conductive material that could possibly connect and shunt the two contacts across the pn-junction. Performing laser ablation along the pn-junction does not solve the shunt problem however.
Samples are furthermore prepared featuring the BSF on one surface and the emitter on the opposite surface of the sample to definitely exclude a shunt between the contacts. The contacts are opened with laser ablation and contacted with Ti/Pd/Ag on both sides, still featuring a low shunt resistance in the dark J-V curve, thus not solving the shunt problem.

Shunt through the emitter region: Shunting through an emitter is more likely for narrow than for deep emitter regions (see Figure 4.13iv-a) because metal can more easily penetrate through a narrow emitter. The shunt resistance of samples, where the emitter depth was reduced from 400 to 300 nm (ECV measurement results) decreased from values $R_{shunt} > 670\ \Omega cm^2$ to about $R_{shunt} \sim 260\ \Omega cm^2$ and lower, thus inflicting on the FF by $3\%_{rel}$ (Quokka simulation). The resulting J-V curve at reverse bias voltage is displayed in Figure 4.12.
Independence of the shunt from the B doping source and the resulting emitter (considering that both emitters are deep enough) is investigated. Therefore, a comparable reference emitter is formed by direct thermal diffusion from boron tribromide (BBr_3). For this diffusion process, nitrogen is bubbled through liquid BBr_3 and introduced with oxygen into the diffusion furnace,

which leads to the formation of a boron trioxide (B_2O_3) layer on the Si substrate[47]. B_2O_3 at the interface forms SiO_2:B, thus offering B for in-diffusion into the substrate[47]. Samples with emitters diffused from BBr_3, with laser ablated contact openings (similar to the ones on the CVD-diffused emitters) and a Ti/Pd/Ag metallization, yield a R_{shunt} as high as 400 Ωcm^2. These samples are therefore not shunt-free, which is why the shunt problem has to have another origin.

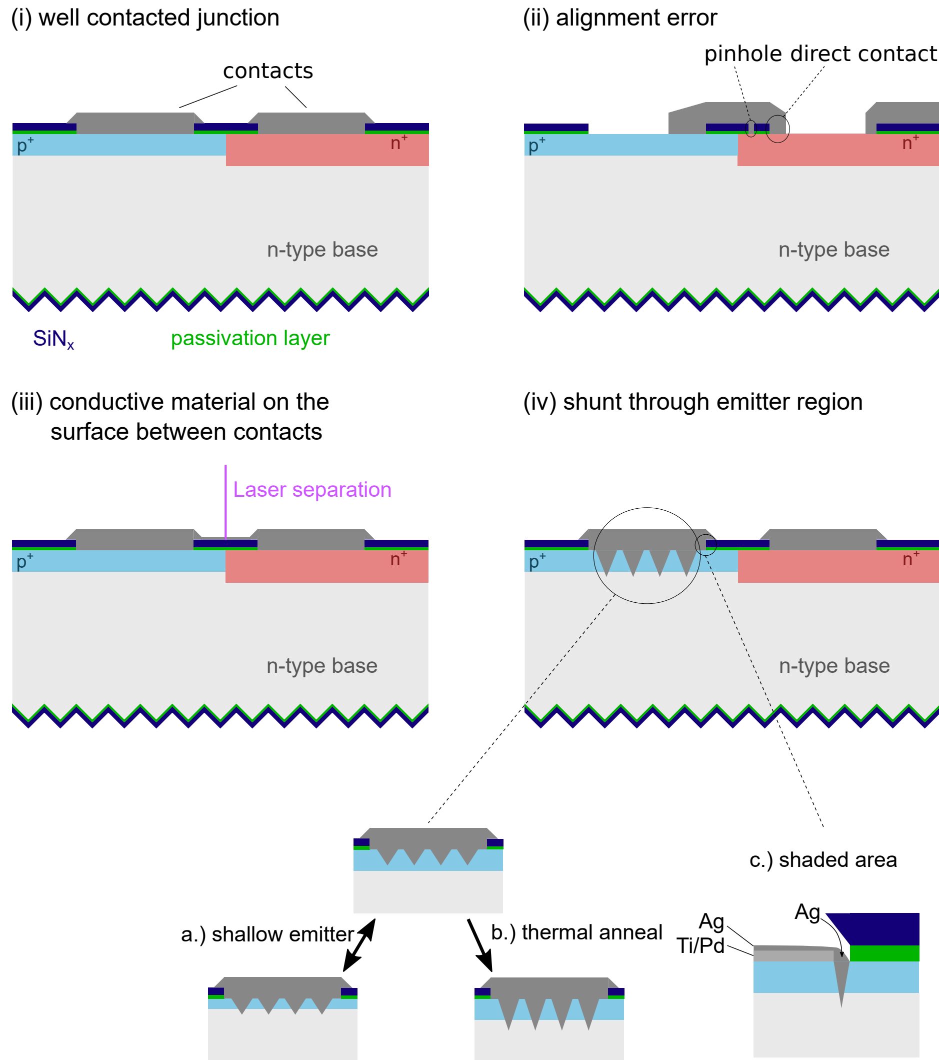

Figure 4.13: Schematic cross sections illustrating possible shunt paths; (i) ideally contacted pn-junction, (ii)alignment error of the metallization, (iii) conductive material on the samples rear surface, connecting the contacts of different polarity, (iv) shunt through the emitter due to a.) a shallow emitter region, b.) thermal annealing, c.) shaded areas that provide uncovered surface on Ag deposition and crystal formation; (not to scale).

Another processing step that could bring about the shunt, is the thermal anneal after the metal deposition (see Figure 4.13iv-b). The thermal input promotes the penetration depth of metal in Si, e.g. by crystal formation. As mentioned above, this step is important to decrease the recombination centers after metal deposition and to activate the passivation layer. Typically it is also performed to enhance the contact between the metal and the Si substrate. Anyway, the results of Chapter 4.3.1 show, that no such annealing step is required for a decent contact formation with Ti/Pd/Ag on an Al_2O_3 passivated surface. Nevertheless, omitting this important processing step does not decrease the shunt problem. The samples are therefore shunted already directly after the metallization process.

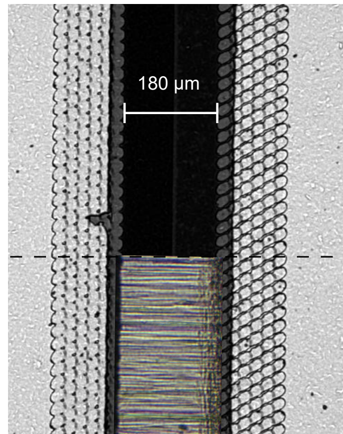

Figure 4.14: Optical microscope image of a pn-junction featuring contact openings and metallized surfaces; The metallized areas appear bright, the laser ablated contact openings are apparent due to the vertical lines of laser spots and the pn-junction in the un-metallized area between the contact openings is visible due to a contrast between the BSF and emitter region; An image of the metallization mask used is added at the bottom of the image.

Laser-related shunts through the emitter region: Since the contact openings of all samples with the shunt problem are performed by laser ablation, the origin of the shunt is possibly related to the laser treatment. The relevant issues resulting from local dielectric layer removal with laser ablation for contact openings, such as the roughened surface in the laser spot overlap areas and the overhanging overhanging CVD residue around the laser spots, are explained in Chapter 4.2.2. SEM images in Figure 4.15 help to identify the problems resulting from these laser treatment artifacts in this specific context.

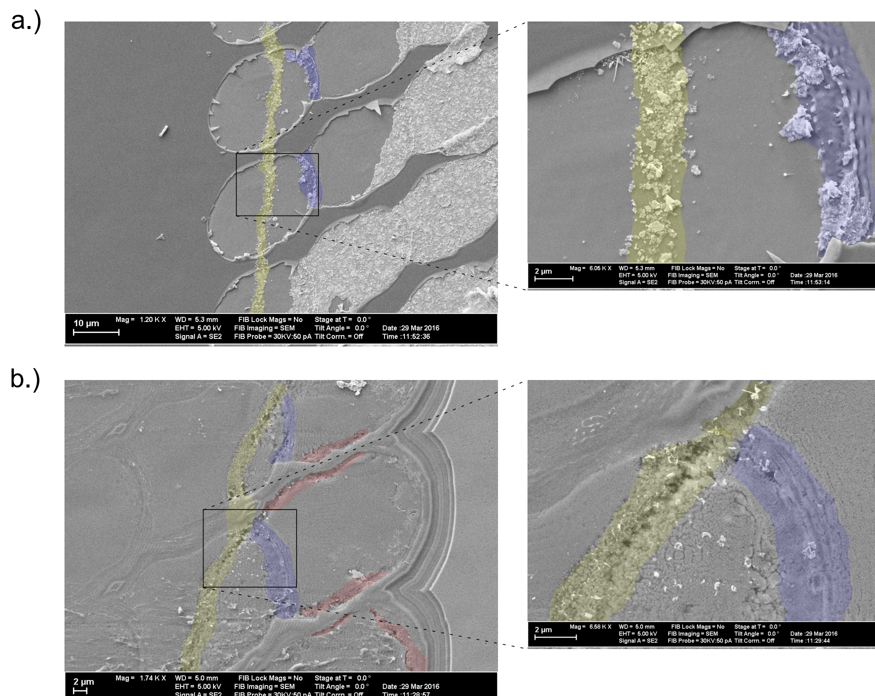

Figure 4.15: SEM images showing contact openings with a.) metal remains at the metallization edge (yellow) and the roughened laser spot overlap area (blue) on a sample etched with HCl, b.) hollows at the metallization edge (yellow) and less densely at the laser spot edge (blue) on a sample etched with HCl and HF solution consecutively; both samples are processed equally.

The SEM images in Figure 4.15a show the emitter contact openings of a shunted sample which is etched in HCl (at 50 °C) to remove the metal in the contact areas. As can be seen, the metal is only partly lifted off and therefore remains in some areas. It is particularly interesting that metal outlasts the etching process in the roughened overlap areas of the laser spots (colored in blue) and along a vertical line, which is identified as the metallization edge (colored in yellow). The metal layers appear to be more tightly bound to the surface in these areas. The sample displayed in Figure 4.15b is etched back with HCl and HF solution as to entirely remove the metal from the Si surface and to furthermore etch the dielectric layers off the Si substrate. While the metal is removed from the area on the right hand side, the left half of the sample in the image was never metallized. The uncovered area reveals some dark sites around the ablation spots (colored in red and blue). A much higher accumulation of these dark sites can be observed along the metallization edge though (colored in yellow). These sites appear dark because they are hollow, with an estimated depth of several μm, hence, the etchant has removed material that does not consist of pure Si in these regions. In conclusion, the metallization must have formed crystals on the Si surface that spiked through the emitter region. It is to be mentioned, that no hollows are visible on the non-metallized surface and the surface covered by SiN_x.
Ti/Pd/Ag metallization of Si is generally performed in a way, such that the Si surface is entirely coated with the thin Ti and Pd layers, while Ag is added as additional coating on the existing metal layers for better conductance only and, hence, to reduce the series resistance. Ag is not meant to get into direct contact with Si because it forms crystals in Si with thermal input[138],[139]. These crystals have the potential to spike through the emitter region.

Discussion: The conclusion of this investigation is, that Ag gets into direct contact with the bare Si substrate where it forms crystals. The metal in these areas is therefore more tightly bound to the Si surface (see Figure 4.15a). According to Figure 4.15b, Ag can get into direct contact with Si to a limited extent in the areas shaded by overhanging CVD residue (colored in red) and on the rough surface in the laser spot overlap area (colored in blue). It reaches the Si surface to a large extent all along the metallization edge however (colored in yellow). This is due to a Ag deposition that is less directed than the deposition of Ti and Pd. It yields the possibility for Ag to reach areas, which are closer to the metallization mask (by about 2 μm) and to the areas shaded by the overhanging CVD residue of dielectric layers, and areas on the roughened surface (see Figure 4.13iv-c). The main reason for shunting is therefore believed to be an error in the metallization concept, that will be explained in the following. Furthermore, since no hollows are observed in the Si that is capped with SiN_x, no penetration of Ag through the capping layer is expected (see Figure 4.15b).
The result of the metallization concept error is, that the contact opening areas are not entirely metallized. If the metallization area extends beyond the contact openings, no crystals penetrate the Si substrate along the metallization edge, as the substrate is then covered by a SiN_x layer at the verge of metallization. The missing metallization in some areas of the contact openings, is due to the fact that the metallization mask shades a larger area from metal deposition than the area that it covers. While the metallization mask has a width of 180 μm along the pn-junction and therefore covers the sample on the same width accordingly, the metallization gap is 230 μm wide (see Figure 4.14). This shading effect is likely to be related to the rotation and the angled sample position during the metal deposition process.
Changing the metallization concept, as to metallize the samples beyond the contact openings, leads to $R_{\text{shunt}} > 670\ \Omega\text{cm}^2$. The theoretically attained FF lies less than $2\%_{\text{rel}}$ below the absolute shunt-free cell (Quokka simulation). The attained shunt resistance of 670 Ωcm^2 and above is therefore sufficient for the experimental procedure in this work.

4.4 Effective Lifetime and Surface Passivation

This chapter discusses the effective lifetime and surface passivation related to this work. As explained in Chapter 2.4.2 and 2.2.3, these quantities are essential for an efficient BC-BJ solar cell and to resolve the recombination process related to the pn-junction on the rear of a BC-BJ cell. The effective minority charge carrier lifetime τ_{eff} is measured for samples with no emitter, while the recombination parameter J_0 is determined for samples with a doped surface region.

4.4.1 Effective Lifetime Measurement

A Sinton Lifetime Tester WCT-120[140] is employed to measure these quantities. A coil, located underneath the sample, measures the change in inductance that is caused by variation of the sample's resistivity. Illumination of the sample generates free charge carriers, thus, increasing the excess carrier density Δn and lowering the resistivity of the sample (see Chapter 2.1.3). In the experimental setup, the sample is illuminated by a flash light with a wavelength >700 nm, as to obtain a relatively homogeneous charge carrier generation along the sample's depth. The generation rate of the light illumination can be separately measured by a reference cell. Since the charge carriers are not extracted from the sample, they recombine within the sample.
Nagel et al. derive the following basic differential equation for the excess carrier density from the generally valid continuity equation[141]

$$\frac{\mathrm{d}\Delta n}{\mathrm{d}t} = G(t) - R(t) = G(t) - \frac{\Delta n(t)}{\tau_{\text{eff}}(\Delta n)} \tag{4.4}$$

where G is the generation rate and R is the recombination rate.
The Quasi-Steady-State Photoconductance (QSSPC) method, introduced by Sinton et al.[142], applies to samples with a low charge carrier lifetime. The inductance of the sample is measured, while slowly-decaying the light illumination. As mentioned earlier, the inductance is linked to Δn. By furthermore knowing the optical constant, the generation rate can be calculated from the light illumination. The sample's charge carrier lifetime must be much lower than the light illumination decay, so that the excess carrier population is at all times in steady-state condition $R = G$. The differential equation 4.4 then transforms into

$$\tau_{\text{eff}}(\Delta n) = \frac{\Delta n}{G} \tag{4.5}$$

In this setup, the QSSPC method is valid for an effective lifetime of 200 μs or lower because of a decay constant of about 2 ms.
A method to measure the effective charge carrier lifetime for samples with longer effective lifetimes is the transient Photoconductance Decay (PCD) method. The amount of free charge carriers decreases according to an exponential decay after a short light flash. Due to the shortness of the light pulse, the generation can be omitted from the differential equation 4.4, thus making the exponential decay apparent in the resulting equation

$$\tau_{\text{eff}}(\Delta n) = \frac{\Delta n}{\mathrm{d}(\Delta n)/\mathrm{d}t} \tag{4.6}$$

This method is solely applied for longer effective lifetimes because a significant excess carrier density should still be measurable after the light flash has terminated.

Passivation Quality Characterization

For samples without doped surfaces, the effective minority charge carrier lifetime τ_{eff} is measured as discussed above at an excess charge carrier density $\Delta n = 3 \cdot 10^{15}$ cm^{-3}. This effective lifetime is Auger-corrected (see equation 2.6), according to

$$\tau_{\text{eff}}^{-1} = \tau^{-1} - \tau_{\text{Auger}}^{-1} \tag{4.7}$$

where τ_{Auger}^{-1} is calculated as reported in equation 2.7. The higher the effective lifetime, the higher the passivation quality of the surface by the covering layers.

Emitter Passivation Quality Characterization

For samples with doped regions at the surface, the base doping and the diffusion process are chosen accordingly, so that the doped regions form an emitter on the front and rear surface. The effective lifetime of these symmetric samples is measured as depicted above. The recombination parameter J_0 is extracted from the slope of the Auger-corrected inverse lifetime versus injection level curve under high injection conditions, $\Delta n = 3 \cdot 10^{15}$ cm^{-3}, according to the method of Kane and Swanson[143].

4.4.2 Photoluminescence

Photoluminescence is a simple, fast and non-destructive technique to measure the effective lifetime spatially resolved. This measurement technique gives insight into the spatial resolution that cannot be measured with the effective lifetime tester introduced above. Photoluminescence measurements are performed to accompany the lifetime measurements as to identify processing errors and to determine local fluctuations of the effective lifetime on samples. However, no physically relevant effects were observed.
For the purpose of photoluminescence measurement, the sample is optically excited by spatially homogenized infrared (808 nm) laser light. The illumination generates charge carriers in the sample that are not extracted from the sample and therefore recombine within the sample. The luminescence of the sample, which results from radiative recombination (see Chapter 2.2.1), is acquired by a camera.

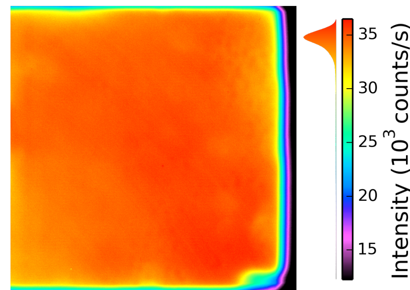

Figure 4.16: Photoluminescence image of a float-zone sample with a p-type base and a 45 $\Omega/\square$ emitter passivated with Al_2O_3 and capped with SiN_x.

As mentioned in Chapter 2.2.1, radiative recombination is rather unlikely in an indirect semiconductor such as Si, thus proceeding in a ms timescale. Charge carriers, located in regions of the sample where other recombination mechanisms are more likely to take place, recombine earlier. These charge carriers are therefore not available for radiative recombination, thus leading to a

reduced photoluminescence emission in these regions. Accordingly, a high photoluminescence signal is a sign for a reduced recombination. Well processed float-zone lifetime samples feature a homogeneous photoluminescence intensity pattern with a lower lifetime at the sample's edge (see Figure 4.16). The homogeneous passivation quality was observed for the Al_2O_3 as well as for the a-Si passivated samples.

4.4.3 Sample Preparation

Different samples are analyzed in the following, always with the aim to gain knowledge about recombination effects taking place in the bulk or at the surface. This way, the impact of different processing steps on the effective lifetime is investigated. These samples have a size of 40x40 mm^2 or larger, as to fully cover the a area measured by the coil of the lifetime tester.

4.4.4 Rear Side Passivation

The rear side of the samples is divided into three differently doped regions: the emitter, the BSF and the gap region. As mentioned in Chapter 2.2.2, a-Si and Al_2O_3 are not expected to passivate all surfaces with the same quality. This is due to the fixed negative charges that are contained in Al_2O_3 and are absent in a-Si, and to a possibly different chemical passivation quality. Additionally, damage at the surface in the BSF and gap region is expected when laser treated, thus increasing the recombination at the surface. The recombination parameter J_0 is only investigated in the non-contacted areas.

Thermal Anneal

As mentioned in Chapter 2.2.2, Al_2O_3 and a-Si both require a thermal anneal to develop their full passivation quality. Furthermore, the annealing step can decrease the amount of recombination centers that are induced by laser ablation for instance. The major improvement in the overall passivation quality, as a result from thermal annealing, is due to a better chemical passivation. Therefore, the thermal annealing effect on the behavior of the emitter's passivation quality should be applicable to that of the FSF, BSF and gap region. The main investigation is therefore solely performed on an emitter region and well-performing thermal annealing parameters are applied on the other samples. In this work, the passivation layer covering the sample is always coated by a SiN_x layer that serves as an ARC on the font and as a capping layer on the rear. The samples can be thermally annealed in a furnace or on a hot-plate. Samples annealed in the furnace are loaded onto a quartz carrier and inserted into the furnace in a vertical position. The annealing in the furnace is performed in vacuum condition. The temperature of the samples in the furnace is known, therefore the actual temperature of the sample is mentioned in the follow. Samples annealed on the hot-plate are 'sandwiched' between two thick Si wafers. The sample temperature is not precisely tracked during this process, therefore the set temperature is used as indication of the thermal input. At a temperature of 400 °C, an offset of approximately 30 °C is measured between the set temperature and the actual temperature of the sample.
Thermal annealing results in the dissertation of Lüder[144] serve as a reference for the Al_2O_3 passivation. The conclusion for thermal annealing in that work, is that annealing at 420 °C for 30 min yields the best result for the effective lifetime. A lower lifetime is achieved for lower annealing temperature, and a temperature of up to 500 °C does not improve the passivation quality any further. A clear increase of the surface passivation is observed in the first 30 min of annealing, followed by a slow decline of the passivation quality for longer annealing duration.
Non-columnar a-Si passivation layers are ideally annealed at temperatures of 300 °C and lower,

as reported by Gloger in[25]. This is due to the fact that annealing at higher temperature leads to hydrogen dissipation from the substrates surface to the ambient atmosphere, thus leading to a deterioration of the passivation quality[71]. This annealing temperature applies to uncapped a-Si passivation layers, however. In this work, a-Si passivation layers are capped by a SiN_x layer, which contains a considerable amount of hydrogen, therefore possibly providing hydrogen for a better surface passivation. Higher annealing temperatures are therefore imaginable for these capped samples.
Since some J-V samples will feature both types of surface passivation (one on each surface) on the same sample, the thermal anneal in this work aims at an annealing temperature that is applicable to achieve a high passivation quality with both passivations. Furthermore, shorter annealing times of 30 min or less are preferred for processing reasons.

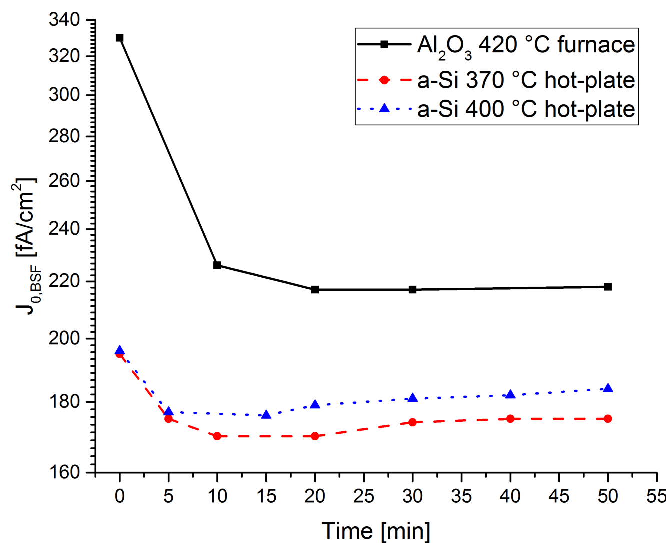

Figure 4.17: Thermal annealing J_0 results of a n-type 45 Ω/□ emitter with Al_2O_3 and a-Si passivation.

A comparison between Al_2O_3 and a-Si passivation on a n-type 45 Ω/□ (ECV measurement) emitter is performed. Owing to the fact that n-type base material is used for the J-V samples, this n^+ emitter, which is diffused into p-type base material, corresponds to a BSF region on the J-V samples. This n^+ emitter is therefore referred to as BSF in the following. For thermal annealing, Al_2O_3 samples are tempered at 420 °C (as proposed in[144]) and two temperatures above 300 °C are used to anneal the a-Si samples (see Figure 4.17). It is apparent that the Al_2O_3 passivated samples start at a much higher recombination parameter value in the non-annealed state than the a-Si passivated samples, hence, yielding a lower passivation quality in the non-annealed state. Furthermore, during the entire annealing procedure, the Al_2O_3 passivated samples never reach a passivation quality that is comparable to that of the a-Si passivated samples. The lower passivation quality of Al_2O_3, in spite of the suitable annealing conditions (see the investigations of the p-type 140 Ω/□ emitter), is attributed to the fixed negative charges in the passivation layer. These charges are not convenient for the passivation of n^+ doped regions because they create an electric field that attracts minority charge carriers to the highly recombinative surface, thus increasing the total recombination in the n^+ doped region. Nevertheless, an increase in surface passivation can be observed for the samples passivated with Al_2O_3, with a minimum reached at 20 and 30 minutes and a slight decrease for longer annealing times. This corresponds well to the behavior observed in[144]. As mentioned, the a-Si passivation

in general yields a lower surface recombination. The annealing optimum appears to be reached between 10 and 20 min at 370 °C set temperature, while an annealing temperature of 400 °C features a lower passivation quality, which is reached after 5 min already. It can be seen, that annealing temperature above 300 °C are applicable to increase the surface passivation quality of a-Si.
The resulting recombination parameters on a p-type 140 Ω/□ (ECV measurement) emitter are displayed in Figure 4.18. As for the BSF, the passivation quality before annealing is higher with the a-Si passivation. This shows that a-Si yields a higher chemical passivation quality than Al_2O_3 after deposition without annealing step. The recombination parameter value decreases during the annealing process for all Al_2O_3 passivated samples. Longer annealing duration than 40 min is not measured, because no further development is expected for the sample annealed at 420 °C due to the observation of the BSF passivation quality behavior earlier, that shows saturation for samples annealed at 420 °C, and due to the investigation performed in[144]. The annealing at higher temperature appears to be performed at a higher rate, thus leading to the best result for 30 min at 420 °C annealed in the furnace.
The a-Si passivated samples show a different behavior in the same temperature range. While annealing at a set temperature of 300 °C leads to an increase of the surface passivation during the first 50 min of annealing, the samples processed at higher temperature show an an increase of the passivation quality in the first minutes of annealing followed by a passivation quality decrease after 5-10 minutes. The highest passivation quality is attained by samples annealed for 10 min at 370 °C on the hot-plate. This result corresponds well to the measurements of the BSF passivation quality.

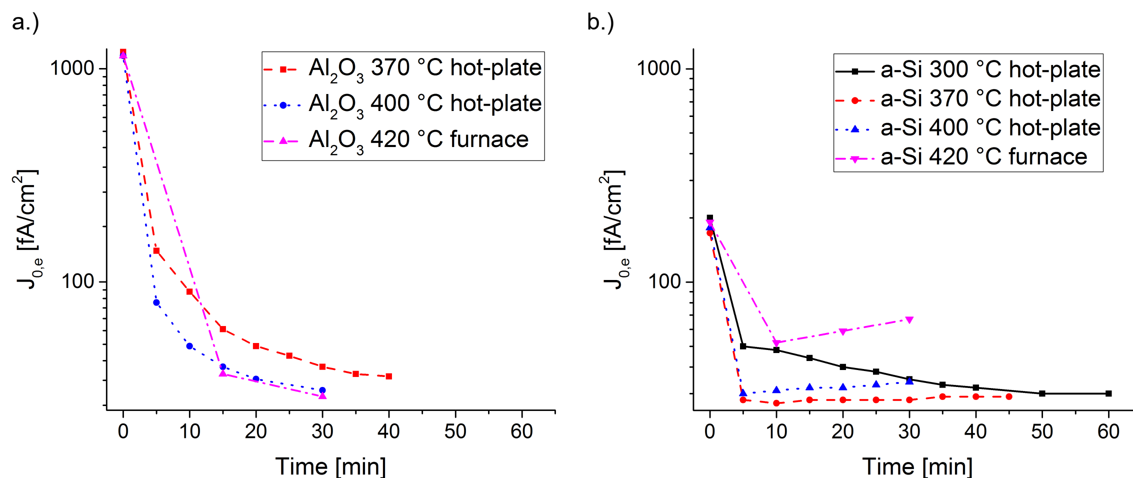

Figure 4.18: Thermal annealing J_0 results of a p-type 140 Ω/□ emitter with a.) Al_2O_3 and b.) a-Si passivation.

If both passivation layers are to be annealed at the same temperature for the same duration, a compromise for a decent passivation quality of both layer has to be found. Both passivation layers yield a similarly high passivation quality when annealed at 400 °C on the hot-plate for 25 min. While shorter annealing duration and a cooler temperature would be favorable for the a-Si passivation, the Al_2O_3 passivation performs better for longer annealing duration and hotter annealing temperature.

Emitter Passivation

Since the emitter region in this work is formed by B diffusion from a SiO_x:B/SiN_x stack on a smooth surface, the surface is not laser treated at any moment. The recombination parameter is therefore solely dependent on the emitter doping profile and the passivation layer used. Some passivation results are presented in the section above, nevertheless, the best $J_{0,e}$ values of two emitters are discussed in the following.
The highest passivation quality attained for a lowly and a highly doped emitter are displayed

Table 4.2: Emitter passivation quality results.

$R_{sheet,emi}$	140	60	$\Omega/\square$
$J_{0,e}$, Al_2O_3 Passivation	29	40	fA/cm^2
$J_{0,e}$, a-Si Passivation	28	90	fA/cm^2

in Table 4.2. Al_2O_3 and a-Si yield similarly high passivation quality results on the lowly doped emitter. The fixed negative charges in the Al_2O_3 passivation layer lead to a favorable field effect passivation on a p-type emitter, keeping the minority charge carriers from the surface. For this reason, the chemical passivation quality of the a-Si layer must be superior to that of Al_2O_3, as to compensate for the lacking field effect passivation. A clear difference in passivation quality of the two layers can be observed for the highly doped emitter. The higher doping in the emitter with lower sheet resistance, increases recombination, hence, generally leading to a higher recombination parameter. As a consequence, a slight increase in $J_{0,e}$ can be observed for Al_2O_3 passivated samples. The $J_{0,e}$ of a-Si passivated samples triples from 28 to 90 fA/cm^2 however. It is believed, that the field effect passivation of the Al_2O_3 layer has an increased importance for the more highly doped emitter, thus keeping $J_{0,e}$ at a low level.

BSF Passivation

While some thermal annealing results of the BSF region are presented earlier in this chapter, the best passivation results achieved on a 45 $\Omega/\square$ BSF are presented in this section (see Table 4.3). The results are obtained with samples that are not laser treated, the laser treatment results are shown in the next section.
As mentioned in the context of thermal annealing, a-Si passivates the BSF region better than

Table 4.3: BSF passivation quality results.

$R_{sheet,emi}$	45	$\Omega/\square$
$J_{0,e}$, Al_2O_3 Passivation	217	fA/cm^2
$J_{0,e}$, a-Si Passivation	170	fA/cm^2

Al_2O_3. This can be attributed to the inconvenient field effect of Al_2O_3 on a BSF region and the lower chemical passivation quality of Al_2O_3.

Laser Processed Surfaces

Furthermore, the recombination parameter of ps- and ns-laser treated surfaces is investigated. The recombination parameter is determined for P diffused surfaces since laser ablation is performed on surface areas, where the BSF region ought to be diffused. For this study, the surface

is coated with a SiO_x:B/SiN_x stack and ablated with the ps- or the ns-laser on the entire surface area on both surfaces. The ns-laser treated samples are subsequently coated with SiN_x and ablated once more on the entire surface. The resulting J_0 values are displayed in Table 4.4. It is to be mentioned, that the difference in sheet resistance between the two diffused regions is primarily due to the laser doping that results from the ns-laser ablation of the SiO_x:B/SiN_x layer stack (see Chapter 4.2.2).
The results reveal, that the recombination parameter is increased in comparison to the BSF

Table 4.4: a-Si passivation quality results of a laser treated BSF region.

Laser treatment	$J_{0,\mathrm{BSF}}$	$R_{\mathrm{sheet,BSF}}$
ps-laser ablation of SiO_x/SiN_x stack	(453±168) fA/cm^2	45 Ω/□
ns-laser ablation of SiO_x/SiN_x stack and subsequent ns-laser ablation of SiN_x	(645±56) fA/cm^2	90 Ω/□

passivation of surfaces which are not laser treated. The laser treated surfaces are exposed to CVD deposition and laser ablation. A recombination investigation concerning the exposition of samples to SiN_x CVD deposition is presented in Chapter 4.4.6. The conclusion is, that SiN_x deposition does not impact on the samples lifetime. Due to a SiO_x:B/SiN_x deposition at the same temperature, the main effect on the recombination is expected to result from laser ablation. The impact of laser ablation on the surface topography is presented in Chapter 4.2.2, and is expected to have a considerable effect on the recombination at the surface. A J_0 increase from 170 to 453 fA/cm^2, and 645 fA/cm^2 respectively, is therefore explained by the impact of the altered surface. It is apparent, that the recombination parameter is higher for the ns-laser ablated samples. This can be explained by the higher induced damage, due to the ns pulse timescale and the double-ablation of the surface.
It is furthermore to be mentioned, that the high temperature treatment during the diffusion process possibly reduces the laser-induced damage to a certain extent, which is favorable for the recombination in the BSF.

4.4.5 Bulk Lifetime

The importance of a high bulk lifetime for a decent BC-BJ solar cell is explained in Chapter 2.4.2. Float-zone material obtained directly from the producer is considered very clean and is regularly tested for its effective lifetime. The resulting lifetime for samples passing through standard cleaning procedures in our research group is clearly in the ms range.
Some samples used in this work, are obtained from a batch of n-type float-zone wafers that had previously been textured on one side, already, and therefore appeared to be suitable for this process. Having doubts about the quality of the material, the bulk material is tested by performing a standard passivation procedure, that consists of a Piranha cleaning process, coating of the sample with a 25 nm Al_2O_3 passivation layer on both sides and annealing it at 420 °C. The effective lifetime measurements amount to 530±70 μs in average. In comparison, symmetric samples that are freshly textured, cleaned and passivated, show effective lifetimes of 3 ms and higher.
The cleaning procedure directly following the texturing did, most likely, not entirely remove the impurities on the surface at the time, thus making the diffusion of impurities into the bulk possible during the long resting time. Due to the limiting effective lifetime and the risk of deterioration during the ensuing processing steps, this material is not further used.
Simulating the lifetime decrease from 3000 μs to 500 μs in Quokka shows, that the efficiency of a high performance BC-BJ solar cell drops from 22.3% to 20.1% as a result. The low effective

lifetime has as consequence, that the highest loss contribution is bulk recombination. This recombination loss severely inflicts on the J_{sc}, lowering it by $5\%_{\text{rel}}$. In conclusion, a low effective bulk lifetime has a major impact on the cell performance.

4.4.6 Front Side Passivation

Texture

The front surface of a BC-BJ solar cell is textured to allow better incoupling of impinging photons (see Chapter 2.4.2). Samples in this work are processed accordingly. Texturing (see Chapter 4.2.4) of the front surface is ideally performed after the diffusion step and before the surface passivation. In theory, the texturing can also be carried out at an earlier processing stage. This, however, leads to a lifetime drop that is discussed in the following.

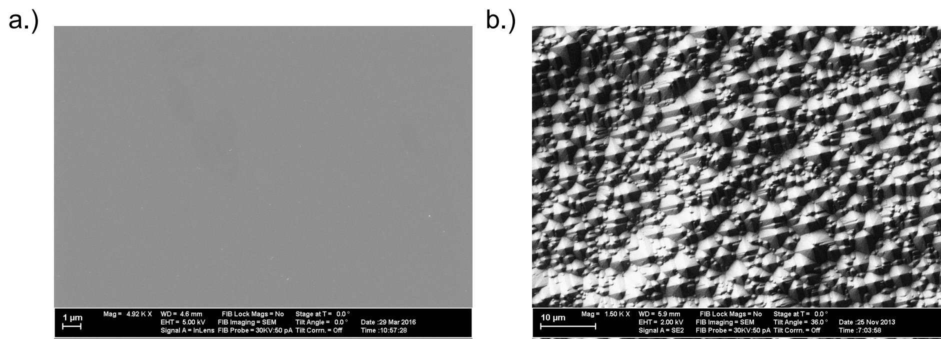

Figure 4.19: SEM top-view image of a.) a smooth surface and b.) a textured surface.

As mentioned in Chapter 4.4.5, samples that are textured, cleaned and passivated, yield high effective lifetimes of about 3 ms for a 7.5 Ωcm n-type bulk, while 3-8 ms are attained with a 200 Ωcm p-type bulk. No dependence of the effective lifetime on the surface passivation (a-Si or Al_2O_3) can be identified, which is a sign for a high surface passivation quality with both passivation layers. Furthermore, the effective lifetime appears to be independent of the additional SiN_x layer (deposition temperature: 230 °) covering the passivation layer. It is important, that the SiN_x deposition does not lower the effective lifetime, because the passivation layer on the front side (as well as on the rear side) is covered by SiN_x that functions as an ARC at the front and capping layer on the rear.
If the sample is textured before the diffusion process, the textured surface is to be formerly capped because the samples should be undoped on the front side. During this study, symmetric textured samples are therefore coated with SiN_x and inserted into a co-diffusion process. For this purpose, SiN_x capping layers from different CVD instruments are utilized. The capping ability of these layers on textured surfaces is tested with ECV measurement. No dopant diffusion into the substrate is observed. However, the effective lifetime decreases to values of 300 μs and less. Several possible explanations for the lifetime drop are taken into consideration: Problems related to the SiN_x capping layer deposition, a general bulk deterioration and a correlation to different surface passivation layers are looked at, to finally come to the conclusion, that the combination of texture and diffusion of the sample cause the lifetime deterioration.

SiN_x deposition: A lifetime deterioration resulting from SiN_x deposition on the blank textured sample is considered. For this purpose, SiN_x is deposited (deposition temperature of 400 °C) and removed in HF solution. The un-diffused symmetric samples are passivated and their effective bulk lifetime is measured. The SiN_x processing step has no noticeable impact on the effective

bulk lifetime. In addition, impurity diffusion from the SiN_x layer into the substrate during the diffusion process is investigated by inserting smooth coated samples in a diffusion process. No decline in the effective lifetime is noticed, however. An impact of the SiN_x layer on the effective lifetime is consequently ruled out.

Bulk deterioration: Another explanation would result from an effective lifetime deterioration in the bulk, that is not triggered by the textured surface. The missing lifetime drop, after diffusion-processing samples with a smooth surface, contradicts this thesis. During further investigation, the surface of textured samples, with a low effective lifetime after diffusion, is etched down by a depth of 3 μm, cleaned and passivated again. The effective lifetime again reaches the level of 3 ms. In conclusion, a general degradation of the bulk material can be excluded and the effective lifetime reduction can be attributed to surface-near effects.

Surface passivation: The surface passivation is studied in more detail earlier in this work. Nevertheless, in this context a-Si and Al_2O_3 are applied as passivation layers on samples before and after the diffusion process. The high effective lifetime of samples prior to diffusion with either of the passivation layers, is presented earlier. In contrast, textured samples processed in the diffusion process, provide very low effective lifetime with either of the two passivation layers. As a result, the effective lifetime drop does not appear to be related to the surface passivation.

Discussion: In conclusion, the diffusion process itself must have a relevant impact on the effective lifetime of textured samples. Since the samples are capped by SiN_x, which does not provide an evident amount of impurities, the lifetime deterioration is bound to result from impurities on the surface itself. Even though the textured surface is cleaned in a Piranha cleaning process, impurities must be present on the textured surface after the cleaning process. During the diffusion process, that is performed at high temperatures, these impurities are able to diffuse into the substrate and increase the recombination in the wafer. In consequence, this problem is ideally avoided by postponing the process step of texturing the sample to a stage after the diffusion process.
The lifetime deterioration is expected to be linked to the low bulk lifetime presented in Chapter 4.4.5. Impurities at the wafers' opened textured surface are expected to have moved into the wafer during the resting time before usage. Since processed samples are stored with passivated surfaces, this deterioration process might not occur with processed samples. The lifetime samples presented earlier in this chapter yield with no exception effective lifetimes of 2.7 ms or more after a resting time of more than 100 days in the dark. Therefore, no noticeable impact of the impurities on the J-V samples is expected.
Unfortunately, this problem was revealed only while processing the last batch of samples that are relevant in the context of this work. Therefore, all samples discussed in this work, have an effective lifetime problem. According to Sentaurus simulations, this lifetime problem decreases the V_{oc} and the FF of the zebra characterization structure (see Chapter 3.3) by $3\pm0.5\%_{\mathrm{rel}}$. The difference between the samples with and without an intrinsic gap is reduced to $\Delta V_{\mathrm{oc}} = 7$ mV and ΔFF=1.0, thus making the comparison more challenging.

Surface Passivation

The front surface is coated with a passivation layer and an ARC, as mentioned earlier. The ARC is adapted in thickness to the passivation layer below, as to enhance the photon absorption. In this cell concept, the passivation layer ought not to absorb impinging photons, which are supposed to reach the c-Si substrate. Al_2O_3 is an insulator with a large band-gap (see Chapter

2.2.2) and thus does not absorb photons. a-Si, on the other hand, is a semiconductor material, which is why photon absorption in the a-Si passivation layer is a relevant factor. The absorption of photons in the a-Si layer is therefore investigated in the following.
A Woollam W-VASE Ellipsometer[145] is used to obtain the optical constants, such as the refractive index n and the extinction coefficient κ, and the layer's thickness. For this purpose, the ellipsometer uses polarized light and measures the relative phase and intensity change of the reflectance beam[146]. The Fresnel equations are the physical basis for ellipsometry. The angle and the wavelength can be varied during the measurement to enhance characterization of the thin material layer. Modeling of the measurements is verified to be consistent with the Kramers-Kronig relationships. The relationships link the refractive index and the absorption coefficient to one another, because they are part of one single parameter, the complex refractive index.
The measurement results for the extinction coefficient κ are used to calculate the absorption coefficient α according to equation 2.2 and α serves to draw a light intensity graph (normalized equation 2.1) in dependence of the penetration depth and the wavelength of the penetrating light. These results are displayed in Figure 4.20.

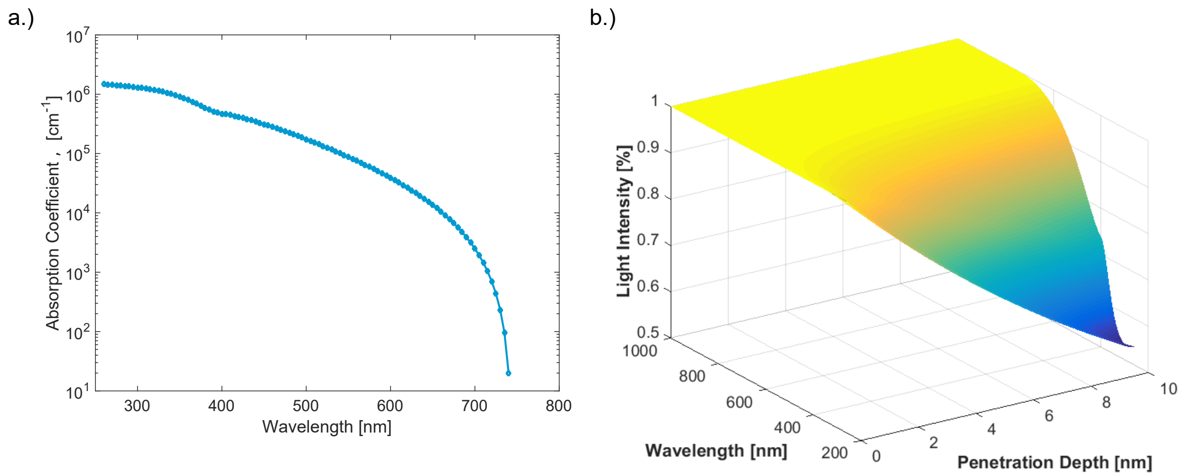

Figure 4.20: a.) absorption coefficient of a-Si as a function of wavelength, and b.) light intensity in a-Si as a function of wavelength and penetration depth.

The resulting absorption coefficient corresponds well to the literature[147] and confirms, that a-Si absorbs much more light than c-Si in the relevant wavelength interval around 500 nm. In consequence, as shown in Figure 4.20b, the light intensity noticeably declines when the light penetrates the a-Si layer. At short wavelengths of about 250 nm, the light intensity decreases to a value below 80% for a penetration depth of 5 nm into the a-Si layer and to about 55% at a penetration depth of 10 nm. As apparent from Figure 4.20a, the absorption coefficient is lower at longer wavelengths. Nevertheless, a considerable amount of light can be absorbed in the a-Si passivation layer. The a-Si passivation layer on the textured front surface is therefore kept as thin as possible, while maintaining a high passivation quality. An a-Si layer thickness of 5 nm is chosen for the front surface passivation, resulting in effective lifetimes above 1.5 ms on n-type 7.5 Ωcm material.

4.5 Characterization Method

After metallization and annealing, the *J-V* characteristics of the so prepared samples are measured. The illumination of the front surface is defined to a certain area by an illumination mask

(see Chapter 4.5.1) that has to be accurately aligned with regard to the pn-junction. An alignment concept (see Chapter 4.5.2) is developed for this purpose, which yields precise alignment results and is an experimental viable method. With a well-aligned illumination mask, the *J*-*V* curve is measured under illumination.

4.5.1 Illumination Mask

The illumination mask is laser cut from a steel sheet. The mask defines the illuminated surface for the illuminated *J*-*V* curve measurement (see Figure 4.21) and therefore features an illumination slit towards the center of the 50x50 mm^2 mask, which is positioned on the opposite sample's surface (front) along the pn-junction. The slit width of the illumination masks varies on different masks between 1 and 2 mm while the height is set to 35 mm. Sentaurus Synopsis simulation results show, that the slit width decrease leads to a better experimental distinctness of the samples with and without a gap (see Chapter 3.3). Furthermore, a more narrow illumination slit is an advance towards the reality of a BC-BJ solar cell with closely alternating p$^+$- and n$^-$-doped regions. A much more narrow illumination slit is not taken into consideration, because possible alignment inaccuracy is expected to have a much higher influence on the *J*-*V* characteristics for a more narrow slit width. Details about the alignment method and the resulting accuracy are given in Chapter 4.5.2.

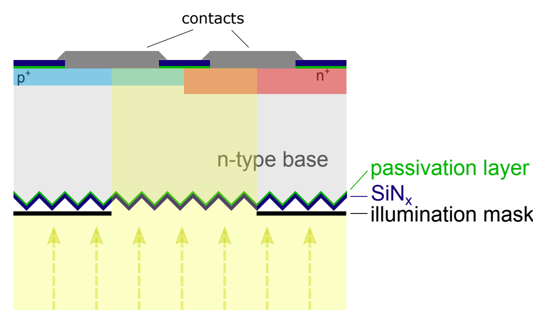

Figure 4.21: Schematic cross section of an illuminated pn-junction; The illuminated surface is defined by the illumination mask (not to scale).

4.5.2 Alignment Method

Along the sample's processing, several alignment procedures are required to line up the pn-junction, the contact openings, the metallization and the illuminated area. An alignment procedure is introduced for this purpose, which enables the alignment of structures at the rear of the cell (pn-junction, contact openings and metallization) with the illumination mask on the front side. The accurate and reproducible alignment of the sample's different structures is essential for the characterization method to achieve consistent results.
The first structure that is created on the sample, is the pn-junction in zebra structure on the rear surface (see Chapter 4.2.3). The alignment of the pn-junction is performed with a four-point orientation to the sample's edges, which defines the pn-junction towards the sample's center (see Figure 4.22i). All further alignment steps are related to the location of this pn-junction.
The contact openings are directly aligned with the pn-junction according to a two-point orientation (see Figure 4.22ii). Furthermore, reference holes in four cross-shapes are shot through the sample in this processing step. These laser shot-through crosses facilitate the alignment of masks on the sample and increase the positioning accuracy. More importantly, the reference holes enable the alignment of a mask on the front surface. While the front surface previously

demonstrates a homogeneous surface, the reference holes are the only alignment reference on the sample's front surface.

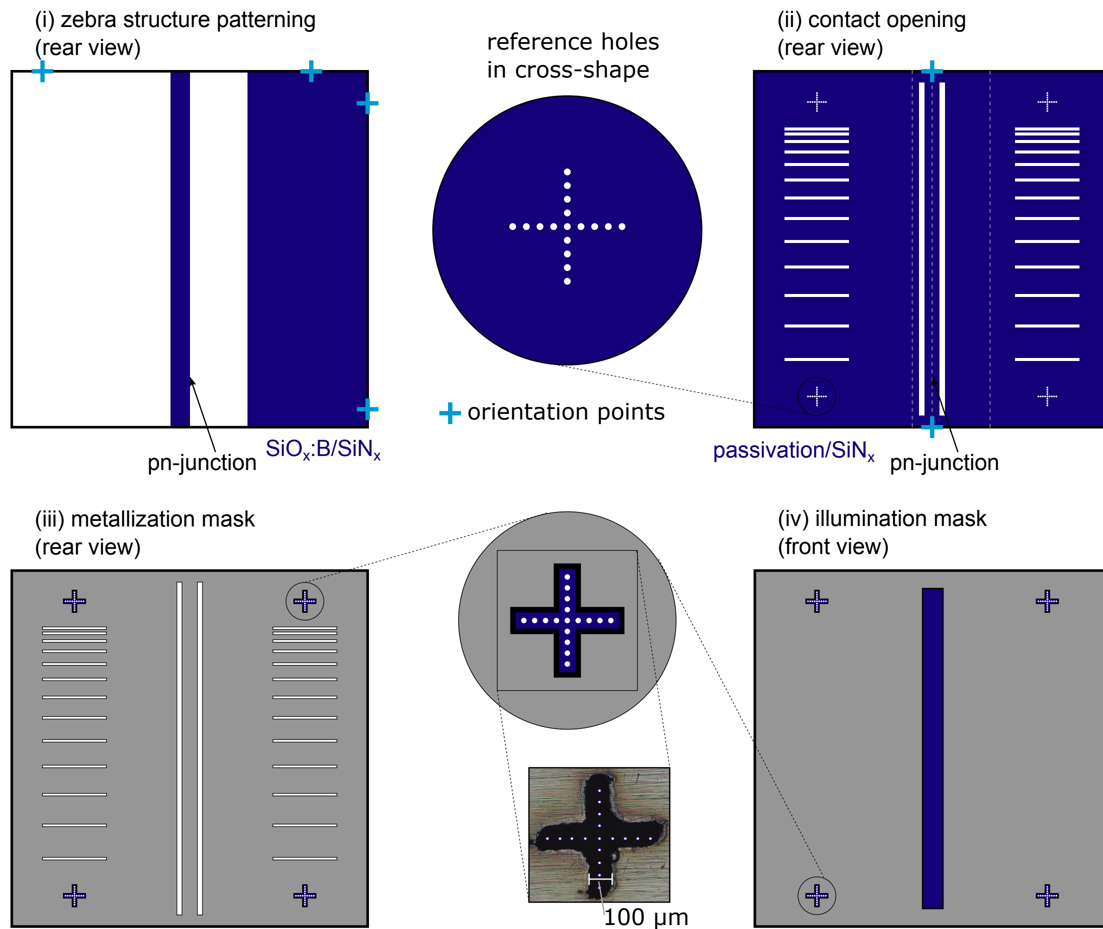

Figure 4.22: Schematic illustration of the alignment steps during the sample processing; Top-view of the rear/front surface, close-ups and a microscope image of an aligned cross-opening in the mask and the reference holes in cross-shape; i.) zebra structure patterning of the SiO_x:B/SiN_x layer stack with four-point orientation, ii.) contact openings aligned with the pn-junction with two-point orientation - laser formed reference holes, iii.) alignment of the metallization mask with the pn- and TLM-contact openings and the reference holes, iv.) illumination mask aligned with the reference holes on the front side; (not to scale).

During the metallization process, the metallization mask (see Chapter 4.3.2) covers the surface that is not to be metallized. The alignment is achieved by matching the mask openings with the contact openings and further accuracy can be obtained with the reference holes (see Figure 4.22iii). During the illuminated J-V curve measurement, the illumination mask has to be placed on the front surface (see Figure 4.22iv). The shot through reference holes are key for the alignment of the illumination mask on the front surface because they are the only reference point on the sample's front (see also Figure 4.1).
Mask alignment is performed by hand under an optical microscope. Cross-shaped openings are laser-cut into the mask in the positions on the mask corresponding to the reference holes in cross-shape on the sample to be able to use the reference holes for alignment. All four crosses on the sample are matched with the four crosses of the mask for alignment. An alignment error can occur due to rotation or displacement of mask and sample. The advantage of having several crosses in different extremities of the sample is, that not all crosses match if the sample and the mask are twisted to each other. The reference holes have a diameter of 5-10 μm and the cross-shaped openings in the mask have an opening width of approximately 100 μm. A

displacement of 20 μm or more can be identified and corrected. A minimum accuracy with this alignment approach of 20 μm is therefore estimated. The structures on the sample are in the order of 200 μm and larger, such as the illumination slit of $\geq$1000 μm and a distance from the metallization mask edge to the contact opening of $\geq$ 200 μm. A mask misplacement of 20 μm or less is therefore negligible. A shunt due to misalignment of the metal contacts on the sample, such as discussed in Chapter 2.4.2 and 4.3.3, is consequently unlikely.

4.5.3 J-V Curve Measurement

The J-V curve of the fully processed samples, which are covered by the illumination mask on the front surface, is measured. For this purpose, the pn-junction contacts on the sample's rear side are contacted by the pins of the measuring chuck. The sample is then moved in a calibrated solar simulator for the measurement duration, during which the applied voltage is varied in a certain interval and the resulting current is measured. This measurement typically takes up to 5 s.

4.6 J-V Curve Measurement Results

The characteristic quantities obtained by J-V curve measurement of the single pn-junctions are discussed in this chapter. These quantities are believed to contain important information about the samples. Expected values for the characteristic quantities of an ideally processed sample can be found in Chapter 3.3.
Several processing difficulties are discussed in the course of this work. As described in Chapter 4.4.6, all J-V samples that are presented in this chapter, have a reduced effective lifetime. Since the various other complications exposed in this work were revealed during processing of the samples, all J-V samples have one further issue, which is mentioned in the discussion that follows whenever relevant. Due to the difficulties in processing the samples, no resulting pn-junction's characteristic quantities are of high performance. As a result, no conclusion about effects at a high efficiency pn-junction can be reached. This would have been done by comparing samples with and without an intrinsic gap region for instance.
In this work, samples are exposed to different processing procedures, the resulting characteristic quantities therefore vary widely. For this reason, the characteristic quantities of similarly processed samples are compared to one another. Conclusions can be drawn to whether the variation of a single processing step has an influence on the J-V curve as such. This chapter is structured accordingly.

4.6.1 Patterning of the pn-Junction

The SiO_x:B/SiN_x stack on the samples can be patterned with either photolithography or laser ablation to create the pn-junction on the sample's rear side (see Chapter 4.2.3). The results of samples patterned with both techniques are compared in the following. It is to be mentioned, that the investigation is performed on samples with $R_{\text{shunt}} \leq 160\ \Omega\text{cm}^2$, that correspond to the shunted samples presented in Chapter 4.3.3. The shunt has a particularly strong effect on the FF value, as explained in Chapter 2.5.1, which is why a difference in FF can be attributed to an inequality in the shunt resistance. Since the pn-junction patterning is not expected to have a noticeable impact on the shunt behavior, the FF and consequently the η are excluded from the comparison.
The averaged V_{oc} results in Table 4.5, shows no difference between the differently patterned samples. The obtained J_{sc} values, on the other hand, are slightly better for the photolithography

Table 4.5: Comparison of J_{sc} and V_{oc} of samples with pn-junctions patterned by photolithography or ps laser ablation; The samples yield a low shunt resistance.

pn-Junction patterning technique	J_{sc} [mA/cm^2]	V_{oc} [mV]
Photolithography	29.5±0.9	600±2
ps laser ablation	27.4±1.2	600±6

processed samples. In this context, it is to be mentioned, that these photolithography samples were cleaned after the photoresist removal (see Chapter 4.2.1) because the CVD etch rate was suited for this procedure. Since laser ablation is the quicker processing technique, the pn-junction in the further sample processing is defined by laser ablation anyway. It is to be noted, that the ps pulsed laser does not lead to laser doping, as explained in Chapter 4.2.2. Problems resulting from laser doping are therefore not considered in this sub-chapter.

4.6.2 Surface Passivation

It is a known fact, that surface passivation is important to decrease the charge carrier recombination in a Si wafer and, thus, in a solar cell (see Chapter 2.2.2). This sub-chapter concerns itself with samples featuring lowly to highly passivated front and rear surfaces.

Rear Surface Passivation

A low passivation quality is expected from surfaces that are solely coated with cold SiN_x, because this SiN_x is not adapted to passivate Si surfaces, since it is typically used as a protection covering layer. Samples with surfaces, which are coated by this SiN_x layer only, are therefore expected to yield low characteristic quantities. This is illustrated by results displayed in Table 4.6. All characteristic quantities of samples with a lowly passivated rear surface are considerably lower than those of samples with a passivated rear surface. It is to be mentioned, that all of these samples yield a shunt resistance of more than 400 Ωcm^2.

Table 4.6: Characteristic quantities of samples with a lowly passivated rear surface, coated with SiN_x, and with a highly passivated rear surface, coated with a-Si.

Passivation front	Passivation rear	J_{sc} [mA/cm^2]	V_{oc} [mV]	FF [%]	η [%]
SiN_x	SiN_x	9.2±1.1	530±4	63.2±0.9	3.1±0.4
SiN_x	a-Si	19.1±0.4	577±4	70.5±1.4	7.8±0.4

A further comparison of the samples' characteristic quantities according to the rear passivation is displayed in Table 4.7. While the front surface is passivated by Al_2O_3, the rear passivation of the 140 Ω/□ emitter and the 30 Ω/□ BSF is performed with Al_2O_3 or a-Si. The contact openings are formed by laser ablation. It is to be mentioned, that these samples feature a low shunt resistance, due to a narrow emitter region (explained in Chapter 4.3.3). The FF and η are therefore omitted from comparison. Furthermore, caution has to be exercised, when comparing the V_{oc} values. A large difference in shunt resistance can inflict on the V_{oc}, as apparent from Chapter 2.5.1. The shunt resistance indeed varies from values of 116 to 220 Ωcm^2 between the different samples. According to the theory in Chapter 2.5.1 and to Quokka simulations, the

maximum difference in V_{oc} due to this shunt resistance variation, in in the order of 5 mV.
It can be seen in Table 4.7, that the resulting J_{sc} values correspond, while a noteworthy inequality results in the V_{oc} values. This large inequality cannot be explained by a shunt resistance variation. It is to be considered, that changing the rear passivation also implies an adjustment in the metal for contact metallization (see Chapter 2.3) and a difference in the annealing procedure (see Chapter 4.4.4).
Using different metals for metallization does not have a noticeable effect on the specific con-

Table 4.7: J_{sc} and V_{oc} comparison of samples with a Al_2O_3 or a-Si passivated rear surface; The samples yield a low shunt resistance.

Passivation front	Passivation rear	J_{sc} [mA/cm^2]	V_{oc} [mV]
Al_2O_3	Al_2O_3	23.0±0.4	545±4
Al_2O_3	a-Si	22.7±1.1	571±3

tact resistance (see Chapter 4.3.1). The recombination parameter in the contact opening area, however, is not investigated in this work. A different recombination parameter in the contact opening area $J_{0,cont}$ due to the different contact metal and passivation layer residue is therefore possible.
For annealing, different procedures are chosen. While the a-Si passivated samples are thermally annealed for 20 min at 400 °C set on a hot-plate, the Al_2O_3 passivated samples are annealed for 30 min at 420 °C in the furnace. As apparent from Figure 4.18a in Chapter 4.4.4 the higher temperature and longer duration annealing process increases the chemical passivation quality of the passivation layer. A similar passivation behavior is expected for thermal anneal of the front surface passivation layer. In conclusion, the front surface passivated with Al_2O_3 should yield a similar effect, resulting in a reduced recombination parameter for the samples, which are Al_2O_3 passivated on the rear due to the different annealing process. As a consequence, an increased J_{sc} is expected for these samples according to Quokka simulation results.
The difference in V_{oc} is therefore narrowed down to a change in J_0 on the rear sample surface. While Al_2O_3 and a-Si both yield $J_{o,emi} \sim 29$ fA/cm^2 on this emitter, a higher BSF passivation quality is expected by a-Si passivation (see Chapter 4.4.4). According to Quokka simulations, an increased J_0 value in the contact openings or the emitter and BSF conductive area, results in a V_{oc} decrease. A higher recombination parameter yielded by Al_2O_3 passivated samples on some areas of the rear surface is therefore likely. With the decrease in V_{oc}, the simulation results show a simultaneous decline in J_{sc}, however. Since the resulting J_{sc} values are equal, the decrease in current is possibly compensated by the current increase expected from the better front surface passivation of the Al_2O_3 passivated samples, which could keep J_{sc} on the same level.
As a consequence, a-Si passivation is more promising to achieve a high performance pn-junction with the chosen annealing conditions. Changing the front surface passivation layer from an Al_2O_3 to a-Si is investigated in the next section. If a-Si passivates the front and rear surface, the annealing procedure can be adapted to achieve the best possible results.

Front Surface Passivation

Two different front surface passivation layers are used in this work, namely a 10 nm Al_2O_3 and a 5 nm a-Si layer. These samples feature an a-Si passivation on the rear and are thermally annealed for 20 min at 400 °C on a hot-plate (such as in the last section). As discussed in Chapter 4.4.6, the a-Si layer is expected to partly absorb the impinging light. This can also be observed in the resulting J_{sc} values. While samples with an Al_2O_3 passivated front surface yield

$J_{sc} = (22.7 \pm 1.1)$ mA/cm^2, the J_{sc} value for samples with an a-Si passivation are 2.2 mA/cm^2 lower. This reduced J_{sc} is attributed to light absorption in the passivation layer.

4.6.3 Contact Opening

The contact opening can be performed with photolithography or laser ablation (see Chapter 4.2.4). A comparison of the characteristic quantities extracted from J-V curve measurement of samples processed with both techniques is aimed at in this sub-chapter. The used samples feature a low shunt resistance, due to the narrow emitter region (explained in Chapter 4.3.3), accordingly, FF and η are omitted from comparison.
The photolithography process that is performed, is explained in Chapter 4.2.1. In contrast to

Table 4.8: J_{sc} and V_{oc} comparison of samples with contact opening performed with photolithography and laser ablation; The samples yield a low shunt resistance.

Contact opening technique	J_{sc} [mA/cm^2]	V_{oc} [mV]
Photolithography	14±3	522±17
ps laser ablation	22.9±0.7	555±12

laser ablation, photolithography is not considered to alter the Si surface morphology, which is likely to have a negative impact on the recombination parameter of the contact openings. Nevertheless, both characteristic quantities, J_{sc} and V_{oc}, yield considerably lower values for the samples, of which the contacts are opened with photolithography (see Table 4.8). It must be concluded, that the missing cleaning step after photoresist removal (see Chapter 4.2.1) reduces the sample's performance. As mentioned earlier, an increase of the J_0 values on the sample's rear side, lead to a J_{sc} and V_{oc} reduction, as observed in the results displayed in Table 4.8. This appears to apply in this specific case.

4.6.4 Conclusion

Several processing steps are analyzed and conclusions from the J-V results are drawn concerning the techniques used to locally remove dielectric layers and to passivate the sample's surface. However, no conclusion could be drawn about the effects occurring at the pn-junction itself. Further sample processing, with the knowledge gained from the investigations presented in this work, are necessary to attain this insight. A current project aims at the comparison of pn-junctions with and without an intrinsic gap.

5 Summary and Outlook

Due to the special cell design, BC-BJ solar cells require adapted characterization methods, in particular to investigate the junction of the highly doped regions on the cell's rear. The focus of this Master Thesis was the development and implementation of a method to characterize single pn-junctions, which are located on the back of a BC-BJ solar cell. To achieve this objective, an simple process flow was developed to produce suiting samples with a single illuminated pn-junction and two TLM fields. For this purpose, the development of a precise alignment method was essential, which allows alignment with an accuracy of $\sim 20\ \mu$m. All local processing steps are aligned directly or indirectly with the initially produced pn-junction. This applies to the contact openings, the metallization, and even the illumination mask, which is positioned on the front of the sample during the illuminated J-V curve measurement.
Simulations conducted with Sentaurus Synopsis show, that the characterization method can distinguish samples with and without intrinsic gap region between the highly doped regions on the back of the cell, if this region is not defect free. A difference in the fill factor of 1.9% between samples with and without the intrinsic gap is expected for the 'zebra structure', without consideration of tunnel recombination, which would further increase this difference. Furthermore, a comparison was made between the simulations programs Sentaurus Synopsis and Quokka, and differences were presented. In the parameter range of a highly efficient IBC solar cells, there is only a small error for the J-V characteristic quantities. In a more detailed investigation with the FELA, differences in the resistance loss at the BSF contact were found, which indicate that this loss channel is differently implemented into the two simulation programs. Due to the general consistency of the simulation results, Quokka was used as a simulation program to illustrate the influence of certain experimental parameters in the analysis.
The difficulties encountered in the preparation of samples with a single pn-junction and the results obtained, were presented in the context of the individual process steps. In particular, the local removal of dielectric layers was discussed. This layer removal is relevant for the creation of the pn-junction, which is formed in a single diffusion process from borosilicate glass and $POCl_3$ gas, but also for the opening of the contact surfaces. The local removal of dielectric layers by means of photolithography and laser ablation (ns and ps pulsed lasers) was carried out, analyzed, and comparisons were drawn between the two methods. The focus was clearly on laser ablation due to the industrial relevance of this method. In addition, J-V measurements show that the applied photolithography process does not provide performance advantages over laser ablation. Consequences of effects such as laser doping (with the ns pulsed laser), surface roughening in overlap areas, and shading CVD material remains were observed, characterized and tested for relevance in the sample production process. As a result, a process could be presented for the production of pn-junctions with and without the intrinsic region.
Furthermore, the contacts were characterized by TLM measurements. Specific contact resistances of 9-24 mΩcm^2 were measured for the deposited Ti/Pd/Ag and Al/Ag contacts. The contact formation takes place directly during the deposition or during a short thermal annealing process. The specific contact resistance values are independent of the selected method of contact opening and the deposited metal. Shunt problems were also analyzed and corrected.
Further relevant findings were obtained with regard to surface passivation. With thermal anneal, a high passivation quality could be achieved with Al_2O_3 and a-Si passivation. For this purpose, the passivation layers were coated with SiN_x and thermally annealed at a temperature

between 300 and 420 °C. A recombination parameter J_0 below 30 fA/cm^2 was obtained for a 140 $\Omega/\square$ p-type emitter passivated with Al_2O_3 or a-Si. The J-V measurements also underline the importance of adequate surface passivation. The passivation quality was tested for the rear (BSF, laser treated surface and emitter) and the front surface (texture). The absorption of a-Si was also analyzed because of its relevance for the passivation of the front surface with a-Si.

Outlook

The processing difficulties seem to be overcome at this time, which is why further sample processing with the presented manufacturing process should lead to a result with high characteristic quantities. In particular the increased lifetime, due to the postponed texturing step, and the non-existent laser doping, due to the use of the ps laser on the entire area that has to be ablated, are an improvement to the last processed samples. With these processed samples, the comparison between samples with and without the intrinsic gap can then be drawn. A clear distinction between these samples would be a milestone for the characterization method and would provide the proof-of-concept. Further investigations, with applied reverse bias voltage or with varied rear surface passivation, could provide additional information on the properties of the pn-junction.

In addition, the concept can be extended to more than one pn-junction per sample. Sufficient information on the contact formation on samples has already been collected in the course of this work, which is why the TLM structure is no longer required on all samples. Adding pn-junctions on a sample has the advantage that a considerably higher number of measurable pn-junctions can be produced. In addition, conclusions about possible processing problems can be classified more easily. Alternating p- and n-doped regions on the entire sample's rear side also represent an approximation to the structure of an IBC solar cell.

Moreover, an examination of the pn-junction using KPFM would be useful. Following the proposal in this work, the pn-junction could be polished at a small angle to the surface so as to obtain a depth resolution of the pn-junction with KPFM measurement. Accordingly, one obtains insight into the doping profile as a resolution in depth.

6 Zusammenfassung und Ausblick [german]

Aufgrund des speziellen Zellkonzeptes, benötigen BC-BJ Solarzellen angepasste Charakterisierungsmethoden, um insbesondere den Kontaktbereich unterschiedlicher hochdotierter Regionen auf der Zellrückseite zu untersuchen. Im Mittelpunkt dieser Masterarbeit stand die Entwicklung und Umsetzung einer Methode für die Charakterisierung einzelner pn-Übergänge, welche sich auf der Zellrückseite einer BC-BJ Solarzelle befinden. Zum Erreichen dieses Ziels wurde ein industrienaher Prozessfluss zur Herstellung passender Proben mit einem einzelnen beleuchteten pn-Übergang und zwei TLM Feldern erarbeitet. Dafür war die Entwicklung einer präzisen Ausrichtungsmethode wesentlich, welche eine Ausrichtung mit einer Genauigkeit von $\sim 20\ \mu$m ermöglicht. Dabei werden alle lokalen Prozessierungsschritte direkt oder indirekt am anfänglich hergestellten pn-Übergang ausgerichtet. Dies trifft auf die Kontaktöffnung, die Metallisierung und sogar die Beleuchtungsmaske zu, welche auf der Vorderseite der Probe bei der J-V Kurvenmessung positioniert wird.
Durchgeführte Simulationen mit Sentaurus Synopsis zeigen, dass die Charakterisierungsmethode Proben mit und ohne einen wenige μm breiten intrinsischen Bereich zwischen den hochdotierten Regionen auf der Zellrückseite unterscheiden kann, wenn dieser Bereich nicht defektfrei ist. Eine Differenz im Füllfaktor von 1.9% zwischen Proben mit und ohne den intrinsischen Bereich wird für die 'Zebra-Muster' Struktur erwartet, ohne Berücksichtigung von Tunnelrekombination, welche diese Differenz weiter erhöhen würde. Desweiteren wurde ein Vergleich zwischen den Simulationsprogrammen Sentaurus Synopsis und Quokka gezogen und Unterschiede dargelegt. Im Parameterbereich einer hocheffizienten IBC Solarzelle ergibt sich lediglich ein geringer Fehler für die charakteristischen Größen. Bei der genaueren Untersuchung mit der FELA konnten Unterschiede für den Widerstandsverlust im BSF Kontakt ausgemacht werden, die darauf hindeuten, dass dieser Verlustkanal in den beiden Simulationsprogrammen unterschiedliche Quellen aufweist. Aufgrund der allgemeinen Übereinstimmung der Simulationsergebnisse wurde Quokka im Lauf der Auswertung als Simulationsprogramm verwendet, um den Einfluss bestimmter experimenteller Parameter zu verdeutlichen.
Die bei der Herstellung von Proben mit einzelnem pn-Übergang aufgekommenen Schwierigkeiten und die erzielten Ergebnisse wurden im Zusammenhang mit den einzelnen Prozessschritten vorgestellt. Dabei wurde insbesondere die lokale Entfernung von dielektrischen Schichten diskutiert. Sie ist relevant für die Herstellung des pn-Übergangs, welcher in einem einzigen Diffusionsprozess aus Bor-haltiger CVD Schicht und $POCl_3$ Gas entsteht, aber auch für die Öffnung der Kontaktflächen. Die lokale Entfernung dielektrischer Schichten mittels Photolithographie und Laserablation (ns und ps gepulster Laser) wurde durchgeführt, analysiert, und es wurden Vergleiche zwischen den beiden Methoden gezogen. Dabei lag der Fokus klar auf der Laserablation aufgrund der industriellen Relevanz dieser Methode. Außerdem zeigen J-V Messungen, dass der angewendete Photolithographie-Prozess keine Leistungsvorteile gegenüber der Laserablation bietet. Konsequenzen von Effekten wie Laser-Doping (mit dem ns gepulsten Laser), Obeflächenaufrauhung in Überlappbereichen und abschattendes verbliebenes Material wurden beobachtet, charakterisiert und auf die Relevanz in dem Probenherstellungsprozess überprüft. Als Ergebnis konnte ein Prozesses zur Herstellung von pn-Übergängen mit und ohne intrinsischen Bereich zwischen den hochdotierten Regionen präsentiert werden.
Ferner wurden die Kontakte mit TLM Messungen charakterisiert. Spezifische Kontaktwiderstände von 9-24 mΩcm^2 wurden für die aufgedampftne Ti/Pd/Ag und Al/Ag Kontakte gemessen.

Die Kontaktbildung findet bereits direkt beim Aufdampfen oder während eines kurzen Sintervorgangs statt. Die spezifischen Kontaktwiderstandswerte sind unabhängig von der gewählten Methode der Kontaktöffnung und des aufgedampften Metalls. Des weiteren wurden Shunt-Probleme analysiert und behoben.
Weitere relevante Erkenntnisse wurden im Bezug auf die Oberflächenpassivierung gewonnen. Mit thermischer Behandlung konnte eine hohe Passivierqualität mit Al_2O_3 und a-Si Passivierung erreicht werden. Dafür wurden die Passivierschichten mit SiN_x beschichtet und zwischen 300 und 420 °C thermisch ausgeheilt. Für einen mit Al_2O_3 oder a-Si passivierten 140 $\Omega/\square$ p-Typ Emitter konnte ein Rekombinationsparameter J_0 unter 30 fA/cm^2 werden. Die J-V Messungen unterstreichen außerdem die Wichtigkeit einer adäquaten Oberflächenpassivierung. Die Passivierqualität wurde für die Rückseite (BSF, Laser behandelte Oberfläche und Emitter) und die Vorderseite (Textur) untersucht. Die Absorption von a-Si wurde ebenfalls analysiert, da sie relevant für die Passivierung der Vorderseite mit a-Si ist.

Ausblick

Die Prozessierungsschwierigkeiten scheinen zu diesem Zeitpunkt weitestgehend überwunden zu sein, weshalb eine weitere Probenprozessierung mit dem vorgestellten Herstellungsprozess zu einem Ergebnis mit hohen Kennwerten führen sollte. Dabei sind insbesondere die erhöhte Lebensdauer infolge des retardierten Texturierungsschritts und das nicht-vorhandene Laser-Doping aufgrund der Verwendung des ps Lasers auf der gesamten zu ablatierenden Fläche eine Verbesserung zu den letzten prozessierten Proben. Mit den prozessierten Proben kann dann der Vergleich zwischen Proben mit und ohne dem intrinsischen Bereich gezogen werden. Eine klare Unterscheidbarkeit dieser Proben wäre ein Meilenstein für die Charakterisierungsmethode und würde den Machbarkeitsnachweis liefern. Weitere Untersuchungen, bei angelegter Sperrspannung oder mit variierter Rückseitenpassivierung, könnten zusätzliche Informationen über die Eigenschaften des pn-Übergangs liefern.
Außerdem kann das Konzept auf mehr als einen pn-Übergang pro Probe ausgeweitet werden. Genügend Information über die Kontaktierbarkeit der Proben wurde bereits im Laufe dieser Arbeit gesammelt, weshalb die TLM Struktur nicht mehr auf allen Proben benötigt wird. Weitere pn-Übergänge auf einer Probe zu haben birgt den Vorteil, dass sich so eine erheblich höhere Anzahl an messbaren pn-Übergängen herstellen lässt. Außerdem sind Rückschlüsse auf mögliche Prozessierungsprobleme klarer zuzuordnen. Alternierende p- und n-Regionen auf der gesamten Probe stellen des Weiteren eine Annäherung an die Struktur einer IBC Solarzelle dar.
Darüber hinaus wäre eine Untersuchung des pn-Übergangs mittels KPFM sinnvoll. Dem Vorschlag in dieser Arbeit folgend, könnte der pn-Übergang in einem kleinen Winkel zur Oberfläche poliert werden, um so eine Tiefenauflösung des pn-Übergangs zu erhalten. Auf diese Weise erlangt man tiefenaufgelöste Einsicht in das Dotierprofil.

Acknowledgments

I carried out my Master Thesis in the 'Arbeitsgruppe Photovoltaik' at the Universität Konstanz. The results of this work were realized in cooperation with several of my colleagues and in continual exchange of scientific ideas with them. I would like to thank my co-workers for the pleasant working atmosphere and the fruitful cooperation in the research group.

My special thanks goes to

- Prof. Dr. Giso Hahn for providing me the opportunity to carry out my Master Thesis in his research team and for issuing the first report on my Master Thesis.
- Prof Dr. Thomas Dekorsy for issuing the second report on my Master Thesis.
- Josh Engelhardt, who has been an excellent tutor. He has worked with me and helped me in countless situations, constantly providing input and new ideas.
- Daniel Sommer for the information input and the good advice he has given me as a tutor.
- Dr. Barbara Terheiden for productive discussions and the management of the discussion group concerning boron emitters.
- Dr. Gabriel Micard for the patience during long discussions concerning the conducted simulations and the backgammon games during work breaks.
- Dr. Susanne Fritz for the support with SEM images.
- Lisa Mahlstaedt, Florian Mutter and Bärbel Rettenmaier for their technical support.
- Dr. Sebastian Joos for IT support.

Bibliography

[1] V. Quaschning, *Erneuerbare Energien und Klimaschutz: Hintergründe - Techniken - Anlagenplanung - Wirtschaftlichkeit*. München: Hanser, 2010.

[2] A. McMichael, D. Campbell-Lendrum, S. Kovats, S. Edwards, P. Wilkinson, T. Wilson, R. Nicholls, S. Hales, F. Tanser, D. L. Sueur, M. Schlesinger, and N. Andronova, *Comparative quantification of health risks, chapter 20, Global climate change*. World Health Organization (WHO), 2004.

[3] W. S. Broecker, "Climatic Change: Are We on the Brink of a Pronounced Global Warming?" *Science*, vol. 189, no. 4201, pp. 460–463, 1975. eprint: `http://science.sciencemag.org/content/189/4201/460.full.pdf`.

[4] A. Becquerel, "Recherches sur les effets de la radiation chimique de la lumière solaire, au moyen des courants électriques," *Comptes Rendus de L'Academie des Sciences*, vol. 9, pp. 145–149, 1839.

[5] D. M. Chapin, C. S. Fuller, and G. L. Pearson, "A New Silicon pn Junction Photocell for Converting Solar Radiation into Electrical Power," *Journal of Applied Physics*, vol. 25, no. 5, pp. 676–677, 1954.

[6] Fraunhofer-Institut, *Jahresbericht 2015/16*, Fraunhofer-Institut für solare Energiesysteme ISE, 2015/16.

[7] A. J. Nozik, G. Conibeer, and M. C. Beard, *Advanced Concepts in Photovoltaics*, ser. RSC Energy and Environment Series. The Royal Society of Chemistry, 2014, pp. 1–608.

[8] M. A. Green, K. Emery, Y. Hishikawa, W. Warta, E. D. Dunlop, D. H. Levi, and A. W. Y. Ho-Baillie, "Solar cell efficiency tables (version 49)," *Progress in Photovoltaics: Research and Applications*, vol. 25, no. 1, pp. 3–13, 2017, PIP-16-252.

[9] K. Masuko, M. Shigematsu, T. Hashiguchi, D. Fujishima, M. Kai, N. Yoshimura, T. Yamaguchi, Y. Ichihashi, T. Mishima, N. Matsubara, T. Yamanishi, T. Takahama, M. Taguchi, E. Maruyama, and S. Okamoto, "Achievement of More Than 25% Conversion Efficiency With Crystalline Silicon Heterojunction Solar Cell," *IEEE Journal of Photovoltaics*, vol. 4, no. 6, pp. 1433–1435, Nov. 2014.

[10] M. A. Green, K. Emery, Y. Hishikawa, W. Warta, and E. D. Dunlop, "Solar cell efficiency tables (version 47)," *Progress in Photovoltaics: Research and Applications*, vol. 24, no. 1, pp. 3–11, 2016, PIP-15-272.

[11] E. Franklin, K. Fong, K. McIntosh, A. Fell, A. Blakers, T. Kho, D. Walter, D. Wang, N. Zin, and M. Stocks, "Design, fabrication and characterisation of a 24.4% efficient interdigitated back contact solar cell," *Progress in Photovoltaics: Research and Applications*, vol. 24, no. 4, pp. 411–427, 2016.

[12] C. Reichel, F. Granek, M. Hermle, and S. W. Glunz, "Back-contacted back-junction n-type silicon solar cells featuring an insulating thin film for decoupling charge carrier collection and metallization geometry," *Progress in Photovoltaics: Research and Applications*, vol. 21, no. 5, pp. 1063–1076, 2013.

[13] P. Engelhart, N.-P. Harder, A. Merkle, R. Grischke, R. Meyer, and R. Brendel, "RISE: 21.5% Efficient Back Junction Silicon Solar Cell with Laser Technology as a Key Processing Tool," in *2006 IEEE 4th World Conference on Photovoltaic Energy Conference*, vol. 1, May 2006, pp. 900–904.

[14] J. Nelson, *The physics of solar cells*, English, Repr. London: Imperial College Press, 2010.

[15] M. A. Green, *Silicon solar cells: Advanced principles & practice*, English. Sydney: Univ. of New South Wales, 1995.

[16] P. Würfel and U. Würfel, *Physics of solar cells: From basic principles to advanced concepts*, English, 2., updat. and expand. Weinheim: Wiley-VCH, 2009.

[17] S. M. Sze and K. K. Ng, *Physics of semiconductor devices*, English, 3. Hoboken, NJ: Wiley-Interscience, 2007.

[18] S. M. Sze and M.-K. Lee, *Semiconductor Devices: Physics and Technology, 3rd Edition*, English, 3rd ed. John Wiley & Sons, 2012.

[19] R. Brendel, *Sunrays 1.3*, Garching Innovation GmbH, Max-Planck-Institut für Festkörperforschung, Heisenbergstrasse 1, D-70569 Stuttgart, Germany.

[20] P. P. Altermatt, "Models for numerical device simulations of crystalline silicon solar cells-a review," *Journal of Computational Electronics*, vol. 10, no. 3, pp. 314–330, 2011.

[21] D. Macdonald, F. Rougieux, A. Cuevas, B. Lim, J. Schmidt, M. D. Sabatino, and L. J. Geerligs, "Light-induced boron-oxygen defect generation in compensated p-type Czochralski silicon," *Journal of Applied Physics*, vol. 105, no. 9, pp. 093704/1–7, 2009. eprint: `http://dx.doi.org/10.1063/1.3121208`.

[22] R. Keding, P. Rothhardt, C. Roters, A. Fallisch, S. Hohage, M. Hofmann, R. Woehl, D. Borchert, and D. Biro, "Silicon Doping Performed by Different Diffusion Sources Aiming Co-Diffusion," *27th European PV Solar Energy Conference and Exhibition*, 2012.

[23] G. Micard, A. Dastgheib-Shirazi, M. Steyer, H. Wagner, P. Altermatt, and G. Hahn, "Advances in the understanding of phosphorus silicate glass (PSG) formation for accurate process simulation of phosphorus diffusion," in *27th European PV Solar Energy Conference and Exhibition*, Munich, Germany: WIP-Renewable Energies, 2012, pp. 1355–1359.

[24] R. Ghoshtagore, "Phosphorus diffusion processes in SiO2 films," *Thin Solid Films*, vol. 25, no. 2, pp. 501–513, 1975.

[25] S. Gloger, "Funktionale Schichten aus plasmaunterstützter chemischer Gasphasenabscheidung für kristalline Siliziumsolarzellen," PhD thesis, Universität Konstanz, 2015.

[26] J. Engelhardt, A. Frey, L. Mahlstaedt, S. Gloger, G. Hahn, and B. Terheiden, "Boron Emitters from Doped PECVD Layers for n-type Crystalline Silicon Solar Cells with LCO," *Energy Procedia*, vol. 55, pp. 235–240, 2014, Proceedings of the 4th International Conference on Crystalline Silicon Photovoltaics, SiliconPV 2014.

[27] J. Engelhardt, G. Hahn, and B. Terheiden, "Multifunctional ICP-PECVD Silicon Nitride Layers for High-efficiency Silicon Solar Cell Applications," *Energy Procedia*, vol. 77, pp. 786–790, 2015, Proceedings of the 5th International Conference on Crystalline Silicon Photovoltaics, SiliconPV 2015.

[28] J. Engelhardt, A. Frey, S. Gloger, G. Hahn, and B. Terheiden, "Passivating boron silicate glasses for co-diffused high-efficiency n-type silicon solar cell application," *Applied Physics Letters*, vol. 107, no. 4, p. 042 102, 2015. eprint: `http://aip.scitation.org/doi/pdf/10.1063/1.4927667`.

[29] J. Engelhardt, G. Fitzky, G. Hahn, and B. Terheiden, “Study on the Characteristics of ICP-PECVD Boron Silicate Glasses Dependent on Diborane Flux,” *ECS Journal of Solid State Science and Technology*, vol. 5, no. 10, N81–N89, 2016. eprint: `http://jss.ecsdl.org/content/5/10/N81.full.pdf+html`.

[30] C. Sah, H. Sello, and D. Tremere, “Diffusion of phosphorus in silicon oxide film,” *Journal of Physics and Chemistry of Solids*, vol. 11, pp. 288–298, 1959.

[31] S. Horiuchi and J. Yamaguchi, “Diffusion of Boron in Silicon through Oxide Layer,” *Japanese Journal of Applied Physics*, vol. 1, no. 6, p. 314, 1962.

[32] V. Y. Doo, “Silicon nitride, a new diffusion mask,” *IEEE Transactions on Electron Devices*, vol. ED-13, no. 7, pp. 561–563, Jul. 1966.

[33] A. Dastgheib-Shirazi, M. Steyer, G. Micard, H. Wagner, P. P. Altermatt, and G. Hahn, “Relationships between Diffusion Parameters and Phosphorus Precipitation during the POCl3 Diffusion Process,” *Energy Procedia*, vol. 38, pp. 254–262, 2013.

[34] N. B. Tanvir, R. Keding, P. Rothhardt, S. Meier, A. Wolf, H. Reinecke, and D. Biro, “Codiffusion Sources and Barriers for the Assembly of Back-Contact Back-Junction Solar Cells,” *IEEE Journal of Photovoltaics*, vol. 5, no. 6, pp. 1813–1820, Nov. 2015.

[35] R. Keding, “Co-Diffused Back-Contact Back-Junction Silicon Solar Cells,” PhD thesis, 2015.

[36] P. M. Fahey, P. B. Griffin, and J. D. Plummer, “Point defects and dopant diffusion in silicon,” *Rev. Mod. Phys.*, vol. 61, pp. 289–384, 2 Apr. 1989.

[37] S. W. Jones, *Diffusion in Silicon*, IC Knowledge LLC.

[38] P. Pichler, *Intrinsic Point Defects, Impurities, and Their Diffusion in Silicon*. Springer Vienna, 2004.

[39] C. S. Nichols, C. G. Van de Walle, and S. T. Pantelides, “Mechanisms of dopant impurity diffusion in silicon,” *Phys. Rev. B*, vol. 40, pp. 5484–5496, 8 Sep. 1989.

[40] R. B. Fair and J. C. C. Tsai, “A Quantitative Model for the Diffusion of Phosphorus in Silicon and the Emitter Dip Effect,” *Journal of The Electrochemical Society*, vol. 124, no. 7, pp. 1107–1118, 1977.

[41] F. N. Schwettmann and D. L. Kendall, “Carrier Profile Change for Phosphorus-Diffused Layers on Low-Temperature Heat Treatment,” *Applied Physics Letters*, vol. 19, no. 7, pp. 218–220, 1971. eprint: `http://aip.scitation.org/doi/pdf/10.1063/1.1653892`.

[42] F. Schwettmann and D. Kendall, “On the nature of the kink in the carrier profile for phosphorus-diffused layers in silicon,” *Applied Physics Letters*, vol. 21, no. 1, pp. 2–4, 1972. eprint: `http://aip.scitation.org/doi/pdf/10.1063/1.1654200`.

[43] M. Yoshida, E. Arai, H. Nakamura, and Y. Terunuma, “Excess vacancy generation mechanism at phosphorus diffusion into silicon,” *Journal of Applied Physics*, vol. 45, no. 4, pp. 1498–1506, 1974. eprint: `http://aip.scitation.org/doi/pdf/10.1063/1.1663450`.

[44] M. Yoshida, “Excess vacancy generation by E-center dissociation in the case of phosphorus diffusion in silicon,” *Journal of Applied Physics*, vol. 48, no. 6, pp. 2169–2174, 1977. eprint: `http://aip.scitation.org/doi/pdf/10.1063/1.324016`.

[45] B. Min, H. Wagner, A. Dastgheib-Shirazi, and P. P. Altermatt, “Limitation of Industrial Phosphorus-diffused Emitters by SRH Recombination,” *Energy Procedia*, vol. 55, pp. 115–120, 2014, Proceedings of the 4th International Conference on Crystalline Silicon Photovoltaics, SiliconPV 2014.

[46] S. Solmi and D. Nobili, “High concentration diffusivity and clustering of arsenic and phosphorus in silicon,” *Journal of Applied Physics*, vol. 83, no. 5, pp. 2484–2490, 1998. eprint: `http://dx.doi.org/10.1063/1.367008`.

[47] Y. Schiele, S. Fahr, S. Joos, G. Hahn, and B. Terheiden, “Study on boron emitter formation by BBr3 diffusion for n-type Si solar cell applications,” in *Proceedings of the 28th European Photovoltaic Solar Energy Conference and Exhibition (EU PVSEC 2013)*, München: WIP, 2013, pp. 1242–1247.

[48] E. Tannenbaum, “Detailed analysis of thin phosphorus-diffused layers in p-type silicon,” *Solid-State Electronics*, vol. 2, no. 2, pp. 123–132, 1961.

[49] D. Nobili, A. Armigliato, M. Finnetti, and S. Solmi, “Precipitation as the phenomenon responsible for the electrically inactive phosphorus in silicon,” *Journal of Applied Physics*, vol. 53, no. 3, pp. 1484–1491, 1982. eprint: `http://dx.doi.org/10.1063/1.330646`.

[50] A. S. Grove, *Physics and technology of semiconductor devices*, English. New York: Wiley, 1967.

[51] G. Pignatel and G. Queirolo, “Further insight on boron diffusion in silicon obtained with Auger electron spectroscopy,” *Thin Solid Films*, vol. 67, no. 2, pp. 233–238, 1980.

[52] M. A. Kessler, T. Ohrdes, B. Wolpensinger, R. Bock, and N. P. Harder, “Characterisation and implications of the boron rich layer resulting from open-tube liquid source BBr3 boron diffusion processes,” in *2009 34th IEEE Photovoltaic Specialists Conference (PVSC)*, Jun. 2009, pp. 1556–1561.

[53] X. J. Ning, “Distribution of Residual Stresses in Boron Doped p+ Silicon Films,” *Journal of The Electrochemical Society*, vol. 143, no. 10, pp. 3389–3393, 1996. eprint: `http://jes.ecsdl.org/content/143/10/3389.full.pdf+html`.

[54] M. Grundner and H. Jacob, “Investigations on hydrophilic and hydrophobic silicon (100) wafer surfaces by X-ray photoelectron and high-resolution electron energy loss-spectroscopy,” *Applied Physics A*, vol. 39, no. 2, pp. 73–82, 1986.

[55] Y. J. Chabal, G. S. Higashi, K. Raghavachari, and V. A. Burrows, “Infrared spectroscopy of Si(111) and Si(100) surfaces after HF treatment: Hydrogen termination and surface morphology,” *Journal of Vacuum Science & Technology A: Vacuum, Surfaces, and Films*, vol. 7, no. 3, pp. 2104–2109, 1989. eprint: `http://avs.scitation.org/doi/pdf/10.1116/1.575980`.

[56] M. A. Kessler, T. Ohrdes, B. Wolpensinger, and N.-P. Harder, “Charge carrier lifetime degradation in Cz silicon through the formation of a boron-rich layer during BBr3 diffusion processes,” *Semiconductor Science and Technology*, vol. 25, no. 5, p. 055 001, 2010.

[57] G. Hahn and S. Joos, “Chapter One - State-of-the-Art Industrial Crystalline Silicon Solar Cells,” in *Advances in Photovoltaics: Part 3*, ser. Semiconductors and Semimetals, G. P. Willeke and E. R. Weber, Eds., vol. 90, Elsevier, 2014, pp. 1–72.

[58] D. K. Schroder, R. N. Thomas, and J. C. Swartz, “Free Carrier Absorption in Silicon,” *IEEE Journal of Solid-State Circuits*, vol. 13, no. 1, pp. 180–187, Feb. 1978.

[59] R. A. Sinton and R. M. Swanson, “Recombination in highly injected silicon,” *IEEE Transactions on Electron Devices*, vol. 34, no. 6, pp. 1380–1389, Jun. 1987.

[60] H. G. Grimmeiss, “Deep Level Impurities in Semiconductors,” *Annual Review of Materials Science*, vol. 7, pp. 341–376, Aug. 1977.

[61] A. Cuevas, “The Recombination Parameter J0,” *Energy Procedia*, vol. 55, pp. 53–62, 2014, Proceedings of the 4th International Conference on Crystalline Silicon Photovoltaics (SiliconPV 2014).

[62] M. M. Atalla, E. Tannenbaum, and E. J. Scheibner, “Stabilization of Silicon Surfaces by Thermally Grown Oxides,” *Bell System Technical Journal*, vol. 38, no. 3, pp. 749–783, 1959.

[63] G. Dingemans and W. M. M. Kessels, “Status and prospects of Al2O3-based surface passivation schemes for silicon solar cells,” *Journal of Vacuum Science & Technology A: Vacuum, Surfaces, and Films*, vol. 30, no. 4, p. 040 802, 2012. eprint: `http://dx.doi.org/10.1116/1.4728205`.

[64] S. Gerke, H.-W. Becker, D. Rogalla, G. Hahn, R. Job, and B. Terheiden, “Investigation of hydrogen dependent long-time thermal characteristics of PECV-deposited intrinsic amorphous layers of different morphologies,” in *29th European PV Solar Energy Conference and Exhibition*, 2014, pp. 9–12.

[65] M. Hofmann, C. Schmidt, N. Kohn, J. Rentsch, S. W. Glunz, and R. Preu, “Stack system of PECVD amorphous silicon and PECVD silicon oxide for silicon solar cell rear side passivation,” *Progress in Photovoltaics: Research and Applications*, vol. 16, no. 6, pp. 509–518, 2008.

[66] A. Bentzen, A. Ulyashin, A. Suphellen, E. Sauar, D. Grambole, D. N. Wright, E. S. Marstein, B. G. Svensson, and A. Holt, “Surface passivation of silicon solar cells by amorphous silicon/silicon nitride dual layers,” in *Proceedings of the 15th International Photovoltaic Science & Engineering Conference (China Solar Energy Society, 2005)*, 2005, p. 316.

[67] M. Schaper, J. Schmidt, H. Plagwitz, and R. Brendel, “20.1%-efficient crystalline silicon solar cell with amorphous silicon rear-surface passivation,” *Progress in Photovoltaics: Research and Applications*, vol. 13, no. 5, pp. 381–386, 2005.

[68] A. G. Ulyashin, A. Bentzen, S. Diplas, A. Suphellen, A. E. Gunnaes, A. Olsen, B. G. Svensson, E. S. Marstein, A. Holt, D. Grambole, and E. Sauar, “Hydrogen Release and Defect Formation During Heat Treatments of SiNx:H/a-Si: H Double Passivation Layer on C-SI Substrate,” in *2006 IEEE 4th World Conference on Photovoltaic Energy Conference*, vol. 2, May 2006, pp. 1354–1357.

[69] M. Hofmann, S. Janz, C. Schmidt, S. Kambor, D. Suwito, N. Kohn, J. Rentsch, R. Preu, and S. W. Glunz, “Recent developments in rear-surface passivation at Fraunhofer ISE,” *Solar Energy Materials and Solar Cells*, vol. 93, no. 6-7, pp. 1074–1078, 2009, 17th International Photovoltaic Science and Engineering Conference.

[70] P. P. Altermatt, H. Plagwitz, R. Bock, J. Schmidt, R. Brendel, M. J. Kerr, A. Cuevas, *et al.*, “The surface recombination velocity at boron-doped emitters: Comparison between various passivation techniques,” in *Proceedings of the 21st European Photovoltaic Solar Energy Conference*, WIP Renewable Energies Dresden, Germany, 2006, pp. 647–650.

[71] J. I. Pankove and D. E. Carlson, “Photoluminescence of hydrogenated amorphous silicon,” *Applied Physics Letters*, vol. 31, no. 7, pp. 450–451, 1977. eprint: `http://dx.doi.org/10.1063/1.89737`.

[72] S. DeWolf and M. Kondo, “Abruptness of a-Si:H/c-Si interface revealed by carrier lifetime measurements,” *Applied Physics Letters*, vol. 90, no. 4, p. 042 111, 2007. eprint: `http://dx.doi.org/10.1063/1.2432297`.

[73] S. DeWolf, S. Olibet, and C. Ballif, “Stretched-exponential a-Si:H/c-Si interface recombination decay,” *Applied Physics Letters*, vol. 93, no. 3, p. 032 101, 2008. eprint: `http://dx.doi.org/10.1063/1.2956668`.

[74] F. Werner, B. Veith, D. Zielke, L. Kühnemund, C. Tegenkamp, M. Seibt, R. Brendel, and J. Schmidt, “Electronic and chemical properties of the c-Si/Al2O3 interface,” *Journal of Applied Physics*, vol. 109, no. 11, p. 113 701, 2011. eprint: `http://dx.doi.org/10.1063/1.3587227`.

[75] A. Richter, J. Benick, A. Kimmerle, M. Hermle, and S. W. Glunz, "Passivation of phosphorus diffused silicon surfaces with Al2O3: Influence of surface doping concentration and thermal activation treatments," *Journal of Applied Physics*, vol. 116, no. 24, p. 243 501, 2014. eprint: http://dx.doi.org/10.1063/1.4903988.

[76] B. Hoex, J. J. H. Gielis, M. C. M. van de Sanden, and W. M. M. Kessels, "On the c-Si surface passivation mechanism by the negative-charge-dielectric Al2O3," *Journal of Applied Physics*, vol. 104, no. 11, p. 113 703, 2008. eprint: http://dx.doi.org/10.1063/1.3021091.

[77] P. Saint-Cast, D. Kania, M. Hofmann, J. Benick, J. Rentsch, and R. Preu, "Very low surface recombination velocity on p-type c-Si by high-rate plasma-deposited aluminum oxide," *Applied Physics Letters*, vol. 95, no. 15, p. 151 502, 2009. eprint: http://dx.doi.org/10.1063/1.3250157.

[78] Y. Chen, Y. Yang, J. K. Marmon, X. Zhang, Z. Feng, P. J. Verlinden, and H. Shen, "Independent Al2O3/SiNx:H and SiO2/SiN x:H Passivation of p+ and n+ Silicon Surfaces for High-Performance Interdigitated Back Contact Solar Cells," *IEEE Journal of Photovoltaics*, vol. 7, no. 1, pp. 51–57, Jan. 2017.

[79] D. Schuldis, A. Richter, J. Benick, P. Saint-Cast, M. Hermle, and S. W. Glunz, "Properties of the c-Si/Al2O3 interface of ultrathin atomic layer deposited Al2O3 layers capped by SiNx for c-Si surface passivation," *Applied Physics Letters*, vol. 105, no. 23, p. 231 601, 2014. eprint: http://dx.doi.org/10.1063/1.4903483.

[80] D. Sommer, "Simulation, Entwicklung und Charakterisierung von IBC-Solarzellen mit Neuartigen Emitterschichten," PhD thesis, Universität Konstanz, 2017.

[81] E. O. Kane, "Theory of Tunneling," *Journal of Applied Physics*, vol. 32, no. 1, pp. 83–91, 1961. eprint: http://dx.doi.org/10.1063/1.1735965.

[82] L. Esaki, "Discovery of the tunnel diode," *IEEE Transactions on Electron Devices*, vol. 23, no. 7, pp. 644–647, Jul. 1976.

[83] R. A. Sinton, P. Verlinden, D. E. Kane, and R. M. Swanson., "Development Efforts in Silicon Backside-Contact Solar Cells," in *Proceedings of the 8th European Photovoltaic Solar Energy Conference*, 8. I. P. S. E. Conference, Ed., 1988, p. 1472-1476.

[84] R. A. Sinton and R. M. Swanson, "Simplified backside-contact solar cells," *IEEE Transactions on Electron Devices*, vol. 37, no. 2, pp. 348–352, Feb. 1990.

[85] M. Padilla, "Spatially Resolved Characterization and Simulation of Interdigitated Back Contact Silicon Solar Cells," PhD thesis, Albert-Ludwigs-Universität Freiburg im Breisgau, 2015.

[86] K. Mangersnes, "Back-contacted back-junction silicon solar cells," PhD thesis, Department of Physics, Faculty of Mathematics and Natural Sciences, University of Oslo, 2010.

[87] J. I. Pankove and M. L. Tarng, "Amorphous silicon as a passivant for crystalline silicon," *Applied Physics Letters*, vol. 34, no. 2, pp. 156–157, 1979. eprint: http://dx.doi.org/10.1063/1.90711.

[88] G. A. M. Hurkx, D. B. M. Klaassen, and M. P. G. Knuvers, "A new recombination model for device simulation including tunneling," *IEEE Transactions on Electron Devices*, vol. 39, no. 2, pp. 331–338, Feb. 1992.

[89] H. Hovel, "The Effect of Depletion Region Recombination Currents on the Effeciencies of Si and GaAs Solar Cells," in *Photovoltaic Specialists Conference, 10 th, Palo Alto, Calif*, 1. I. P. S. Conference, Ed., Palo Alto, 1974, pp. 34–39.

[90] A. Kaminski, J. J. Marchand, H. E. Omari, A. Laugier, Q. N. Le, and D. Sarti, "Conduction processes in silicon solar cells," in *Photovoltaic Specialists Conference, 1996., Conference Record of the Twenty Fifth IEEE*, May 1996, pp. 573–576.

[91] O. Breitenstein, "Nondestructive local analysis of current-voltage characteristics of solar cells by lock-in thermography," *Solar Energy Materials and Solar Cells*, vol. 95, no. 10, pp. 2933–2936, 2011.

[92] D. Meier, *Structure and fabrication process for an aluminum alloy junction self-aligned back contact silicon solar cell*, US Patent 5,641,362, Jun. 1997.

[93] H. Plagwitz, "Surface Passivation of Crystalline Silicon Solar Cells by Amorphous Silicon Films," PhD thesis, Gottfried Wilhelm Leibniz Universität Hannover, 2007.

[94] R. J. Schwartz and M. D. Lammert, "Silicon solar cells for high concentration applications," in *Electron Devices Meeting, 1975 International*, vol. 21, 1975, pp. 350–352.

[95] M. D. Lammert and R. J. Schwartz, "The interdigitated back contact solar cell: A silicon solar cell for use in concentrated sunlight," *IEEE Transactions on Electron Devices*, vol. 24, no. 4, pp. 337–342, Apr. 1977.

[96] T. Ohrdes, U. Römer, Y. Larionova, R. Peibst, P. P. Altermatt, and N.-P. Harder, "High fill-factors of back-junction solar cells without front surface field diffusion," in *Proc. 27th Eur. Photovoltaic Sol. Energy Conf. Exhib*, 2012, pp. 866–869.

[97] F. Granek, M. Hermle, D. M. Huljic, O. Schultz-Wittmann, and S. W. Glunz, "Enhanced lateral current transport via the front N+ diffused layer of n-type high-efficiency back-junction back-contact silicon solar cells," *Progress in Photovoltaics: Research and Applications*, vol. 17, no. 1, pp. 47–56, 2009.

[98] I. Cesar, N. Guillevin, A. R. Burgers, A. A. Mewe, M. Koppes, J. Anker, L. Geerligs, and A. W. Weeber, "Mercury: A Back Junction Back Contact Front Floating Emitter Cell with Novel Design for High Efficiency and Simplified Processing," *Energy Procedia*, vol. 55, pp. 633–642, 2014, Proceedings of the 4th International Conference on Crystalline Silicon Photovoltaics (SiliconPV 2014).

[99] S. Kluska, F. Granek, M. Rüdiger, M. Hermle, and S. Glunz, "Characterization and Modeling of Back-Contact Back-Junction Silicon Solar Cells," *24th European PV Solar Energy Conference and Exhibition*, pp. 950–954, Sep. 2009.

[100] S. Glunz, S. Rein, J. Knobloch, W. Wettling, and T. Abe, "Comparison of boron- and gallium-doped p-type Czochralski silicon for photovoltaic application," *Progress in Photovoltaics Research and Applications*, vol. 7, no. 6, pp. 463–469, 1999.

[101] J.-H. Guo, B. S. Tjahjono, and J. E. Cotter, "19.2% efficiency n-type laser-grooved silicon solar cells," in *Conference Record of the Thirty-first IEEE Photovoltaic Specialists Conference*, Jan. 2005, pp. 983–986.

[102] J. E. Cotter, J. H. Guo, P. J. Cousins, M. D. Abbott, F. W. Chen, and K. C. Fisher, "P-Type Versus n-Type Silicon Wafers: Prospects for High-Efficiency Commercial Silicon Solar Cells," *IEEE Transactions on Electron Devices*, vol. 53, no. 8, pp. 1893–1901, Aug. 2006.

[103] D. Macdonald and L. J. Geerligs, "Recombination activity of interstitial iron and other transition metal point defects in p- and n-type crystalline silicon," *Applied Physics Letters*, vol. 85, no. 18, pp. 4061–4063, 2004. eprint: `http://aip.scitation.org/doi/pdf/10.1063/1.1812833`.

[104] S. Rein and S. W. Glunz, "Electronic properties of interstitial iron and iron-boron pairs determined by means of advanced lifetime spectroscopy," *Journal of Applied Physics*, vol. 98, no. 11, p. 113 711, 2005. eprint: `http://aip.scitation.org/doi/pdf/10.1063/1.2106017`.

[105] S. Martinuzzi, O. Palais, M. Pasquinelli, and F. Ferrazza, "N-type multicrystalline silicon wafers and rear junction solar cells," *The European Physical Journal Applied Physics*, vol. 32, no. 3, pp. 187–192, 2005.

[106] R. Brendel, S. Dreissigacker, N.-P. Harder, and P. P. Altermatt, "Theory of analyzing free energy losses in solar cells," *Applied Physics Letters*, vol. 93, no. 17, p. 173 503, 2008.

[107] W. Shockley and H. J. Queisser, "Detailed Balance Limit of Efficiency of pn Junction Solar Cells," *Journal of Applied Physics*, vol. 32, no. 3, pp. 510–519, 1961.

[108] A. Richter, M. Hermle, and S. W. Glunz, "Reassessment of the Limiting Efficiency for Crystalline Silicon Solar Cells," *IEEE Journal of Photovoltaics*, vol. 3, no. 4, pp. 1184–1191, Oct. 2013.

[109] Synopsys, *Sentaurus*, Version 2008/09, Mountain View, CA, 2008.

[110] PVLighthouse, *Quokka Manual*.

[111] A. Fell, "A Free and Fast Three-Dimensional/Two-Dimensional Solar Cell Simulator Featuring Conductive Boundary and Quasi-Neutrality Approximations," *IEEE Transactions on Electron Devices*, vol. 60, no. 2, pp. 733–738, Feb. 2013.

[112] A. Fell, K. Fong, K. McIntosh, E. Franklin, and A. Blakers, "3-D simulation of interdigitated-back-contact silicon solar cells with Quokka including perimeter losses," *IEEE Journal of Photovoltaics*, vol. 4, pp. 1040–1045, 2014.

[113] A. Fell, K. R. McIntosh, M. Abbott, and D. Walter, "Quokka version 2: Selective surface doping, luminescence Modeling and data fitting," in *23rd Photovoltaic Science and Engineering Conference, Taipei*, 2013.

[114] D. A. Kleinman, "The Forward Characteristic of the Pin Diode," *Bell System Technical Journal*, vol. 35, no. 3, pp. 685–706, 1956.

[115] R. Brendel, "Modeling solar cells with the dopant-diffused layers treated as conductive boundaries," *Progress in Photovoltaics: Research and Applications*, vol. 20, no. 1, pp. 31–43, 2012.

[116] J. A. D. Alamo and R. M. Swanson, "The Physics and Modeling of Heavily Doped Emitters," I. T. on Electron Devices, Ed., 12, vol. 31, IEEE, Dec. 1984, pp. 1878–1888.

[117] S. I. Raider, R. Flitsch, and M. J. Palmer, "Oxide Growth on Etched Silicon in Air at Room Temperature," *Journal of The Electrochemical Society*, vol. 122, no. 3, pp. 413–418, 1975. eprint: `http://jes.ecsdl.org/content/122/3/413.full.pdf+html`.

[118] M. Morita, T. Ohmi, E. Hasegawa, M. Kawakami, and M. Ohwada, "Growth of native oxide on a silicon surface," *Journal of Applied Physics*, vol. 68, no. 3, pp. 1272–1281, 1990. eprint: `http://aip.scitation.org/doi/pdf/10.1063/1.347181`.

[119] W. Kern *et al.*, "Handbook of semiconductor wafer cleaning technology," *New Jersey: Noyes Publication*, pp. 111–196, 1993.

[120] *Photolithography: Theory and Application of Photoresist, Etchants and Solvents*. Nicolaus-Otto-Str. 39, D-89079 Ulm, Germany: MicroChemicals GmbH, 2012.

[121] S. Wolf and R. N. Tauber, *Silicon processing for the VLSI era. Volume 1: Process technology*, English. Sunset Beach: Lattice Press, 1986.

[122] G. Heinrich, M. Bähr, K. Stolberg, T. Wütherich, M. Leonhardt, and A. Lawerenz, "Investigation of ablation mechanisms for selective laser ablation of silicon nitride layers," *Energy Procedia*, vol. 8, pp. 592–597, 2011, Proceedings of the SiliconPV 2011 Conference (1st International Conference on Crystalline Silicon Photovoltaics).

[123] J. Engelhardt, "Schadenfreies Ablatieren von dielektrischen Schichten auf kristallinen Silizium-Scheiben," Master's thesis, Universität Konstanz, 2012.

[124] G. Heinrich, M. Bähr, K. Stolberg, T. Wütherich, M. Leonhardt, S. Friedel, A. Lawerenz, and G. Gobsch, "Influence of pulse duration and surface topography on laser ablation of silicon nitride layers on thin emitters," *Pulse*, vol. 40, p. 120, 2011.

[125] F. Haase, T. Neubert, R. Horbelt, B. Terheiden, K. Bothe, and R. Brendel, "Local aluminum-silicon contacts by layer selective laser ablation," *Solar Energy Materials and Solar Cells*, vol. 95, no. 9, pp. 2698–2700, 2011.

[126] F. Haase, E. G. Rojas, K. Bothe, and R. Brendel, "Layer selective laser ablation for local contacts to thin emitters," *Energy Procedia*, vol. 8, pp. 577–580, 2011, Proceedings of the SiliconPV 2011 Conference (1st International Conference on Crystalline Silicon Photovoltaics).

[127] S. Ring, S. Kirner, C. Schultz, P. Sonntag, B. Stannowski, L. Korte, and R. Schlatmann, "Emitter Patterning for Back-Contacted Si Heterojunction Solar Cells Using Laser Written Mask Layers for Etching and Self-Aligned Passivation (LEAP)," *IEEE Journal of Photovoltaics*, vol. 6, no. 4, pp. 894–899, Jul. 2016.

[128] J. Engelhardt, S. Ohl, G. Hahn, and B. Terheiden, "Correlation of Stress in Silicon Nitride Layers with their Complete Removal by Laser Ablation," *Energy Procedia*, vol. 38, pp. 707–712, 2013, Proceedings of the 3rd International Conference on Crystalline Silicon Photovoltaics (SiliconPV 2013).

[129] F. Smits, "Measurement of sheet resistivities with the four-point probe," *Bell System Technical Journal*, vol. 34, pp. 711–718, May 1958.

[130] R. G. Ehl and A. J. Ihde, "Faraday's electrochemical laws and the determination of equivalent weights," *Journal of Chemical Education*, vol. 31, no. 5, p. 226, 1954. eprint: http://dx.doi.org/10.1021/ed031p226.

[131] K. Gelderman, L. Lee, and S. W. Donne, "Flat-Band Potential of a Semiconductor: Using the Mott-Schottky Equation," *Journal of Chemical Education*, vol. 84, no. 4, p. 685, 2007. eprint: http://dx.doi.org/10.1021/ed084p685.

[132] *Kelvin Probe Force Microscopy (KPFM): Investigation of Local Boron Doped Emitter Regions Formed by Inkjet Boron Inks for Industrially Feasible IBC Solar Cells*, vol. 1, 2014, pp. 830–833.

[133] J. Ebser, D. Sommer, S. Fritz, Y. Schiele, G. Hahn, and B. Terheiden, "P+-doping analysis of laser fired contacts for silicon solar cells by Kelvin probe force microscopy," *Journal of Applied Physics*, vol. 119, no. 10, p. 105 707, 2016. eprint: http://dx.doi.org/10.1063/1.4943064.

[134] J. Wong, "Griddler: Intelligent computer aided design of complex solar cell metallization patterns," in *2013 IEEE 39th Photovoltaic Specialists Conference (PVSC)*, Jun. 2013, pp. 0933–0938.

[135] M. Smit, G. Acket, and C. van der Laan, "Al2O3 films for integrated optics," *Thin Solid Films*, vol. 138, no. 2, pp. 171–181, 1986.

[136] H. Leplan, J. Y. Robic, and Y. Pauleau, "Kinetics of residual stress evolution in evaporated silicon dioxide films exposed to room air," *Journal of Applied Physics*, vol. 79, no. 9, pp. 6926–6931, 1996. eprint: http://dx.doi.org/10.1063/1.361517.

[137] G. K. Reeves and H. B. Harrison, "Obtaining the specific contact resistance from transmission line model measurements," *IEEE Electron Device Letters*, vol. 3, no. 5, pp. 111–113, May 1982.

[138] G. Schubert, "Thick Film Metallisation of Crystalline Silicon Solar Cells : Mechanisms, Models and Applications," PhD thesis, Universität Konstanz, Konstanz, 2006.

[139] C. Ballif, D. M. Huljic, G. Willeke, and A. Hessler-Wyser, "Silver thick-film contacts on highly doped n-type silicon emitters: Structural and electronic properties of the interface," *Applied Physics Letters*, vol. 82, no. 12, pp. 1878–1880, 2003. eprint: `http://dx.doi.org/10.1063/1.1562338`.

[140] SintonInstruments, *WCT-120 Photoconductance Lifetime Tester User Manual*, v3.0, Boulder, CO, USA.

[141] H. Nagel, C. Berge, and A. G. Aberle, "Generalized analysis of quasi-steady-state and quasi-transient measurements of carrier lifetimes in semiconductors," *Journal of Applied Physics*, vol. 86, no. 11, pp. 6218–6221, 1999. eprint: `http://dx.doi.org/10.1063/1.371633`.

[142] R. A. Sinton, A. Cuevas, and M. Stuckings, "Quasi-steady-state photoconductance, a new method for solar cell material and device characterization," in *Conference Record of the Twenty Fifth IEEE Photovoltaic Specialists Conference*, May 1996, pp. 457–460.

[143] D. Kane and R. Swanson, "Measurement of the emitter saturation current by a contactless photoconductivity decay method," in *IEEE photovoltaic specialists conference. 18*, 1985, pp. 578–583.

[144] T. Lüder, "Passivierung von kristallinem Silizium mit Aluminiumoxid-Dünnfilmen für Solarzellenanwendungen," PhD thesis, Universität Konstanz, Konstanz, 2014.

[145] J. A. Woollam Co., Inc., *WVASE Manual*.

[146] J. A. Woollam, P. G. Snyder, and M. C. Rost, "Variable angle spectroscopic ellipsometry: A non-destructive characterization technique for ultrathin and multilayer materials," *Thin Solid Films*, vol. 166, pp. 317–323, 1988.

[147] D. E. Carlson and C. R. Wronski, "Amorphous silicon solar cell," *Applied Physics Letters*, vol. 28, no. 11, pp. 671–673, 1976. eprint: `http://dx.doi.org/10.1063/1.88617`.

List of Figures

2.1 Silicon energy band diagram . . . 4
2.2 Generation profile . . . 5
2.3 Silicon doping schematic . . . 7
2.4 Cross section schematic of a diffusion process . . . 8
2.5 Schematic of a pn-junction . . . 10
2.6 Schematic band diagram of a conventional solar cell . . . 10
2.7 Charge carrier recombination paths at a highly doped pn-junction . . . 13
2.8 Schematic cross section of a conventional solar cell . . . 15
2.9 Schematic cross section of an IBC solar cell . . . 16
2.10 Exemplary J-V curve . . . 18
2.11 Impact of the shunt resistance on the J-V curve . . . 18
2.12 Solar Spectrum . . . 20

3.1 FELA of the recombination loss and resistance loss in the bulk obtained from Quokka simulation . . . 23
3.2 Simulation result of the power conversion efficiency obtained with Quokka and Sentaurus Synopsys . . . 24
3.3 J_0 values extracted from Sentaurus Synopsis simulation in the BSF and FSF regions 25
3.4 Normalized subtraction map for η, FF, J_{sc} and V_{oc} . . . 27
3.5 FELA simulation result obtained with Quokka and Sentaurus Synopsis for the BSF contact resistance loss . . . 29
3.6 Cross section generated with Sentaurus Synopsys of the pn-junction . . . 30
3.7 Schematic cross section of the pn-junction showing the half-half structure, the zebra structure and enlargements of the hole current flow . . . 31

4.1 3D schematic of a J-V sample with illumination mask . . . 35
4.2 SEM image for comparison of laser-exposed photolithography and laser ablation used to pattern dielectric material . . . 37
4.3 Microscope image of an under-etched photoresist . . . 38
4.4 Microscope images; Variation of the laser power, the focus and the density of the ablation points for laser ablation . . . 41
4.5 SEM images of a laser treated area showing roughness in the overlap area, remaining covering layer in the center of the ablation spot and overhanging CVD residue around the ablation points . . . 42
4.6 Doping profiles revealing laser doping due to ns-laser ablation before and after a diffusion step . . . 44
4.7 Schematic cross section showing the process from a coated sample to a pn-junction after in-diffusion . . . 45
4.8 Doping profiles measured with ECV after sequential diffusion of a sample covered by a SiO_x:B/SiN_x stack and a sample covered by a SiO_x:B layer only . . . 46
4.9 Schematic cross section showing the process from a coated sample to a coating pattern, which allows the diffusion of a pn-junction with an intrinsic gap . . . 46
4.10 SEM images illustrating the challenges in making a gap region between the highly doped regions of a pn-junction with laser ablation . . . 48

4.11 Microscopy images of samples in two stages of the laser treatment applied to create a gap region between the highly doped regions on the rear side 49
4.12 Measured J-V curves at reverse bias voltage with varying shunt resistance 52
4.13 Schematic cross sections illustrating possible shunt paths 54
4.14 Optical microscope image of a pn-junction featuring contact openings and metallized surfaces 55
4.15 SEM images showing contact openings with crystal formation in the metallization area and the resulting hollows after etching the metal 55
4.16 Photoluminescence image of a float-zone sample with a p-type base and a 45 $\Omega/\square$ emitter passivated with Al_2O_3 and capped with SiN_x 58
4.17 Thermal annealing J_0 results of a n-type 45 $\Omega/\square$ emitter 60
4.18 Thermal annealing J_0 results of a p-type 140 $\Omega/\square$ emitter 61
4.19 SEM image of a smooth and a textured surface 64
4.20 Absorption coefficient of a-Si as a function of wavelength and light intensity as a function of wavelength and penetration depth in a-Si 66
4.21 Schematic cross section of an illuminated pn-junction 67
4.22 Schematic illustration of the alignment steps during the sample processing 68

List of Tables

2.1 Periodic table concerning semiconductors 6

3.1 Input parameters for the simulation of an IBC solar cell 23
3.2 J_0 input parameters for the simulation of the IBC solar cell 25
3.3 Quokka simulation minimum resolution of the characteristic quantities. 28
3.4 Maximum difference value of the loss channels obtained by FELA. 28
3.5 Simulation results achieved with Sentaurus Synopsys of one pn-junction illuminated on a width of 1000 μm with and without an intrinsic gap for the half-half structure and the zebra structure. 32

4.1 Results of the TLM measurements performed on emitter and BSF regions with varying R_{sheet}. 51
4.2 Emitter passivation quality results. 62
4.3 BSF passivation quality results. 62
4.4 a-Si passivation quality results of a laser treated BSF region. 63
4.5 Characteristic quantities of samples with pn-junctions patterned by photolithography or ps laser ablation 70
4.6 Characteristic quantities of samples with a lowly/highly passivated rear surface . 70
4.7 Comparison of J_{sc} and V_{oc} of samples with a differently passivated rear surface . 71
4.8 Comparison of J_{sc} and V_{oc} of samples with contact opening performed with photolithography and laser ablation 72